

Suspended Mirror Pendulum with Radiation Pressure Compensated Laser-Interferometric Position Readout

Dissertation
zur Erlangung des Doktorgrades
an der Fakultät für Mathematik, Informatik und Naturwissenschaften
Fachbereich Physik
der Universität Hamburg

vorgelegt von
Jan Petermann

Hamburg
2022

Gutachter/innen der Dissertation:

Prof. Dr. Roman Schnabel
Prof. Dr. Oliver Gerberding

Zusammensetzung der Prüfungskommission:

Prof. Dr. Roman Schnabel
Prof. Dr. Oliver Gerberding
Prof. Dr. Ludwig Mathey
Prof. Dr. Dieter Horns
Prof. Dr. Henning Moritz

Vorsitzende/r der Prüfungskommission:

Prof. Dr. Ludwig Mathey

Datum der Disputation:

01.09.2022

Vorsitzender Fach-Promotionsausschusses PHYSIK:

Prof. Dr. Wolfgang J. Parak

Leiter des Fachbereichs PHYSIK:

Prof. Dr. Günter H. W. Sigl

Dekan der Fakultät MIN:

Prof. Dr. Heinrich Graener

Abstract

Suspended mirror pendulums have proven to be an important building block in ground-based interferometric gravitational-wave detectors leading to the first observation of a gravitational wave in 2015 [1]. Providing a good isolation from seismic ground motion at frequencies above their resonance frequency, they allow the mirrors to act as quasi-free test masses to probe the fabric of spacetime. Suspended mirrors with macroscopic mass can also be used for experiments on gravitational interactions in the quantum regime [2, 3], which require precise readout and control of the test mass motion.

In this work, I demonstrate an optomechanical tabletop experiment with a suspended cuboid mirror test mass, serving as a common end mirror in a Michelson-Sagnac-type laser interferometer located in a high vacuum. I discuss the properties of damped harmonic oscillators as well as parametric actuation to influence the oscillator's motion and I examine laser interferometers with classical and quantum noise sources. Furthermore, I designed a Michelson-Sagnac interferometer with power- and signal-recycling capabilities and implemented a passive seismic isolation system to reduce the interferometer's seismic excitation. In addition, I planned an active seismic isolation technique to improve the setup. I demonstrate an interferometric position readout for the test mass pendulum as well as detection of the deflection angle for high pendulum amplitudes. I designed and implemented an optical setup with two distinct wavelengths to explore the possibilities for radiation pressure feedback cooling of the test mass motion. A high quality factor between 4×10^4 to 7.6×10^4 for the main pendulum mode at 1.435 Hz was achieved with the suspension system presented here. I characterized the mechanical modes of the pendulum by spectral and ringdown measurements using parametric actuation of the pendulum suspension point to excite and cool the pendulum motion. This might be applicable in gravitational-wave detectors to reduce the on-resonance thermal noise without introducing additional noise at frequencies above.

Kurzfassung

Aufgehängte Spiegelpendel haben sich als wichtiger Baustein in bodengestützten interferometrischen Gravitationswellendetektoren erwiesen, die im Jahr 2015 zur ersten Beobachtung von Gravitationswellen führten [1]. Sie bieten eine gute Isolation von seismischen Bodenbewegungen bei Frequenzen oberhalb der Resonanzfrequenzen und fungieren als quasi-freie Testmassen, um das Raum-Zeit-Gefüge zu untersuchen. Aufgehängte Spiegel mit makroskopischer Masse können auch für Experimente zu gravitativen Wechselwirkungen im Quantenregime verwendet werden [2, 3], die ein präzises Auslesen und Steuern der Bewegung der Testmasse erfordern.

In dieser Arbeit demonstriere ich ein optomechanisches Tischexperiment mit einer aufgehängten quaderförmigen Spiegelttestmasse, die als gemeinsamer Endspiegel in einem im Hochvakuum befindlichen Michelson-Sagnac Laserinterferometer dient. Ich diskutiere die Eigenschaften gedämpfter harmonischer Oszillatoren sowie parametrischer Ansteuerung zur Beeinflussung der Oszillatorbewegung und betrachte Laserinterferometer mit klassischen und Quantenrauschquellen. Darüber hinaus habe ich ein Michelson-Sagnac-Interferometer mit Leistungs- und Signalrecycling entworfen und ein passives seismisches Isolationssystem implementiert, um die seismische Erregung des Interferometers zu reduzieren. Außerdem habe ich eine aktive seismische Isolationstechnik geplant, um den Aufbau zu verbessern. Ich demonstriere eine interferometrische Positionsauslesung für das Testmassenpendel sowie eine Erfassung des Auslenkwinkels für hohe Pendelamplituden. Des weiteren habe ich einen optischen Aufbau mit zwei unterschiedlichen Wellenlängen entworfen und implementiert, um die Möglichkeiten der Strahlungsdruck-Rückkopplungskühlung der Testmassenbewegung zu untersuchen. Mit dem hier vorgestellten Aufhängungssystem wurde eine hohe Güte zwischen 4×10^4 und $7,6 \times 10^4$ für die Hauptpendelmode bei 1,435 Hz erreicht. Ich habe die mechanischen Moden des Pendels durch Spektral- und Ringdown-Messungen charakterisiert. Dabei habe ich parametrische Aktuation des Pendelaufhängungspunkts verwendet, um die Pendelbewegung anzuregen und zu kühlen. Dies könnte in Gravitationswellendetektoren anwendbar sein, um das resonante thermische Rauschen zu reduzieren, ohne zusätzliches Rauschen bei Frequenzen darüber einzukoppeln.

Contents

Contents	ix
List of Figures	xi
List of Tables	xii
List of Abbreviations	xiii
List of Symbols	xiv
1. Introduction	1
2. Damped Harmonic Oscillator	3
2.1. Equation of Motion	3
2.2. Damping Forces	4
2.2.1. Quality Factor	4
2.2.2. Viscous Damping	5
2.2.3. Structural Damping	6
2.3. Spectral Density	6
2.4. Thermal Noise	7
2.5. Non-thermal Noise	8
2.6. Gravity Pendulum	9
2.6.1. Q Factor, Dilution Factor	10
2.6.2. Residual Gas Damping	11
2.7. Parametric Damping	11
3. Laser Interferometers	13
3.1. Michelson-Sagnac Topology	13
3.1.1. Michelson Interferometer	15
3.1.2. Sagnac Interferometer	16
3.2. Interferometer Contrast	17
3.3. Fabry-Perot Resonator	18
3.4. Quantum Noise of Position Measurements	21
3.4.1. Photon Shot Noise	22
3.4.2. Backaction Noise	22
3.4.3. Standard Quantum Limit	23

3.5.	Classical Laser Noise	24
3.5.1.	Amplitude Noise	24
3.5.2.	Phase Noise	24
3.6.	Recycling Techniques	25
3.6.1.	Power Recycling	26
3.6.2.	Signal Recycling	26
4.	Experimental Setup	28
4.1.	Vacuum System	28
4.2.	Seismic Isolation	29
4.2.1.	Optical Table	30
4.2.2.	Seismic Isolation Stage	30
4.3.	Pendulum	35
4.3.1.	Suspension	35
4.3.2.	Test Mass	36
4.3.3.	Pendulum Eigenfrequencies	39
4.3.4.	Pendulum Installation Procedure	43
4.4.	Interferometer	45
4.4.1.	Interferometer Design	45
4.4.2.	Optics	46
4.4.3.	Mirror Positioners	50
4.5.	Optical Setup	51
4.5.1.	1550 nm Setup	51
4.5.2.	1064 nm Setup	53
4.6.	Laser	54
4.6.1.	1550 nm	54
4.6.2.	1064 nm	55
4.7.	Detection	56
4.7.1.	Interferometric Detection	56
4.7.2.	Deflection Angle	56
4.7.3.	Data Acquisition Card	57
4.7.4.	Lock-In amplifier	58
5.	Experimental Results	59
5.1.	Test Mass Internal Cavity	59
5.2.	Pendulum Modes	60
5.2.1.	Main Pendulum Mode	63
5.2.2.	Yaw and Pitch Mode	65
5.2.3.	Violin Modes	69
5.2.4.	Additional Modes	70
5.3.	Pendulum Ringdown	71
5.4.	Amplitude Estimation	74
5.5.	Pendulum in Quadrature Phase Space	76

6. Summary and Outlook	78
Bibliography	80
Appendix A. Legend	87
Appendix B. Pendulum Fits	88
Appendix C. Ringdown Fits	91
Appendix D. Mirror Positioner Configuration and GUI	92
Eidesstattliche Versicherung / Declaration on oath	93
Acknowledgments	94

List of Figures

2.1.	Damped oscillator ringdown	5
2.2.	Thermal noise PSD	8
2.3.	PSD transfer function $ H ^2$	9
2.4.	Gravity pendulum	10
2.5.	Parametrically driven pendulum	12
3.1.	Michelson-Sagnac interferometer	14
3.2.	Fabry-Perot resonator	18
3.3.	Cavity resonances	20
3.4.	Curved mirror resonator	21
3.5.	Recycled Michelson-Sagnac interferometer	25
4.1.	Vacuum assembly	29
4.2.	Concrete block displacement spectrum	31
4.3.	FEM simulation of seismic isolation stage	32
4.4.	Seismic isolation stage	35
4.5.	Suspension system	36
4.6.	<i>MassQ</i> pendulum	37
4.7.	Test mass holder	39
4.8.	Pendulum modes	40
4.9.	Interferometer spacer	46
4.10.	Test mass beam radius	47
4.11.	Mirror positioner	50
4.12.	Optical setup	52
4.13.	1550nm piezo calibration	55
4.14.	1550nm temperature calibration	56
4.15.	Quadrant photodiode	57
4.16.	Lock-in amplifier	58
5.1.	Test mass scanning 1064 nm	60
5.2.	Test mass cavity beam profile	61
5.3.	Test mass scanning 1550 nm	61
5.4.	Broadband mode spectrum	62
5.5.	Main mode spectrum	64
5.6.	Yaw mode spectrum	66
5.7.	Pitch mode spectrum	68

5.8. Violin modes spectrum	70
5.9. Additional pendulum modes	72
5.10. Ringdown measurement	73
5.11. Pendulum amplitude estimation	75
5.12. Pendulum phase space	77
A.1. Legend	87
B.1. Main mode fits	88
B.2. Yaw mode fits	89
B.3. Pitch mode fits	90
C.1. Ringdown fits	91
D.1. Mirror positioner GUI	92

List of Tables

4.1.	Material parameters for isolation stage	33
4.2.	FPM dampers and masse of loads	34
4.3.	<i>MassQ</i> test mass parameters	38
4.4.	Calculated pendulum eigenfrequencies	44
4.5.	Interferometer optics with curvature	48
4.6.	Interferometer cavity parameters	48
5.1.	Fit results main mode	67
5.2.	Fit results yaw mode	68
5.3.	Fit results pitch mode	69
5.4.	Pendulum mode frequencies	71
5.5.	Fit results ringdown	74

List of Abbreviations

Notation	Description
AOI	angle of incidence 49
API	application programming interface 51
AR	anti-reflection 49
ASD	amplitude spectral density 7, 24
CAD	computer-aided design 29, 39, 45
CLI	command-line interface 50, 51
CM	center of mass 10, 37, 38
EOM	equation of motion 3, 10, 41, 42
FDT	fluctuation–dissipation theorem 7
FEM	finite element method 30
FFT	fast Fourier transform 58, 63
FPM	fluoroelastomer 30
FSR	free spectral range 19, 25, 54, 55
FT	Fourier transform 3, 4, 6
FWHM	full width at half maximum 4, 9, 19
GUI	graphical user interface 51
LO	local oscillator 58, 76
PBS	polarizing beamsplitter 51, 53
PRM	power-recycling mirror 26
PSD	power spectral density 3, 6–8, 22–25, 30, 58
PTFE	polytetrafluoroethylene 39
QPD	quadrant photodiode 53, 56, 57, 60, 63, 65, 67, 69, 70, 72, 74, 76
RBW	resolution bandwidth 58, 67
RIN	relative intensity noise 24
RoC	radius of curvature 36, 47, 60, 61
SLS	standard linear solid 34, 35
SQL	standard quantum limit 21, 23, 49
SRM	signal-recycling mirror 26, 27
TEM	transverse electromagnetic mode 19
WSS	wide-sense stationarity 6, 7

List of Symbols

Notation	Description
m	mass
T	temperature
k_{B}	Boltzmann constant
\hbar	reduced Planck's constant
g	acceleration due to gravity
L	pendulum length
t	time
F	force
ϕ	loss factor
Q	Q factor
x	displacement
S_{xx}	displacement spectral density
f	frequency
f_0	eigenfrequency
ω	angular frequency
E	Young's modulus, energy
k	spring constant
A	area
P	power, pressure
r	amplitude reflectivity, radius
R	power reflectivity
I	moment of inertia
τ	torque, exponential decay time
w	beam radius

1. Introduction

Interferometers are a sensitive tool for precise length-change measurements and have been used for over a century now. Starting from Michelson in 1881 with his famous experiment [4] that he improved later together with Morley [5], interferometers have been used in various topologies such as the Sagnac [6] or the Mach-Zehnder interferometer [7, 8]. In the last decade, sophisticated versions of a Michelson interferometer led to the direct detection of gravitational waves and paved the way for gravitational-wave astronomy [1]. For these laser interferometer detectors, mirrors suspended as pendulums with high Q factors are an important building block as they provide isolation from seismic excitation and serve as "free falling" test masses above their resonance frequency to probe the effects of gravitational waves on the fabric of spacetime.

In this work, I studied a single pendulum suspended test mass used as the common end mirror in a Michelson-Sagnac type interferometer as part of the *MassQ* experiment. This topology has been studied before theoretically in [9, 10, 11] and experimentally in [12, 13, 14] with a SiN-Membrane oscillator as common mirror with resonance frequencies in the 100 kHz range and effective masses below 100 ng. One advantage of this topology with a balanced interferometer is that laser amplitude noise does not excite the oscillator's motion via radiation pressure, since the radiation pressure force is equal and opposite on both mirror sides. Using mirrors with macroscopic mass and lower eigenfrequency, this topology could be utilized in pendulum-based interferometric seismometers as in [15] for better sensitivity. Such a system with two massive oscillators might also be used to detect Newtonian noise coupling via the gravitational force between the oscillators. Newtonian noise from seismic fields is expected to limit future ground based gravitational-wave observatories at frequencies below 10 Hz [16]. Since Newtonian noise cannot be shielded with seismic isolation, sophisticated systems to estimate the Newtonian noise from the measured seismic disturbances will be needed to cancel it [17]. Cryogenic cooling of the pendulum and thus decreasing the thermal noise can make it possible for the pendulum motion to be limited by quantum noise fluctuations from back-action and shot noise. This can be used to realize Einstein-Podolsky-Rosen-entangled motion of two massive objects as discussed in [18, 2].

In this thesis, I present the design of a power- and signal-recycled Michelson-Sagnac interferometer with a suspended 50 g cuboid mirror serving as the common end mir-

ror. The test mass was designed to serve as an optical cavity. The cavity axis could then be used as a reference for the alignment of the two interferometer arms. On anti-resonance, the cavity would suppress the optical power inside to reduce heating due to absorption. Since the test mass surface was not manufactured precise enough for the planned design, this alignment scheme could not be tested during this work. However, we successfully set up the suspended mirror pendulum with a Q factor of the main pendulum mode at 1.435 Hz between 4×10^4 to 7.6×10^4 serving as the common end mirror for a Michelson interferometer. With the interferometric measurement and the detection of the deflection angle, a measurement of the pendulum motion for amplitudes over multiple orders of magnitude is established. An optical setup with two distinct laser wavelengths allows for radiation pressure feedback cooling of the pendulum motion inside the interferometer. Additionally, the pendulum motion can be influenced by parametric actuation of the suspension point, which might be applicable in gravitational-wave detectors to reduce the on-resonance thermal noise without introducing additional noise at frequencies above [19]. I designed and implemented a passive seismic isolation system for the interferometer. I observed multiple different mechanical modes of the pendulum and measured the eigenfrequency as well as the Q factor by means of spectral analysis and ringdown measurements. Furthermore, I observed the main pendulum mode in quadrature phase space in the rotation frame of a local oscillator by demodulation of the measurement signal with a lock-in amplifier.

2. Damped Harmonic Oscillator

In this chapter the transfer function for a damped harmonic oscillator is derived based on [12, 20] and the Q factor for viscous and structural damping is introduced. The concept of a power spectral density (PSD) is explained and the thermal and non-thermal noise PSD for the oscillator is discussed. The gravity pendulum and corresponding damping mechanisms are analyzed and the concept of parametrically driven oscillators is shown.

The following uses Newton's notation (dot notation) for the derivative with respect to time $\dot{x}(t) = \frac{dx(t)}{dt}$.

2.1. Equation of Motion

The equation of motion (EOM) for a damped harmonic oscillator with a general damping force F_{damp} driven by an external force F_{ext} is given by

$$m\ddot{x}(t) + F_{\text{damp}}(x(t), \dot{x}(t)) + kx(t) = F_{\text{ext}}(t), \quad (2.1)$$

where m denotes the oscillator's mass and k the spring constant of the harmonic potential. This equation can be transformed into frequency space using the Fourier transform (FT)

$$(\mathcal{F}x)(\omega) = \hat{x}(\omega) = \int_{-\infty}^{\infty} x(t)e^{-i\omega t} dt. \quad (2.2)$$

Applying Leibniz integral rule to the time derivative of the inverse FT

$$\frac{d^n}{dt^n}x(t) = \frac{d^n}{dt^n} \left(\frac{1}{2\pi} \int_{-\infty}^{\infty} \hat{x}(\omega)e^{i\omega t} d\omega \right) \quad (2.3)$$

$$= \frac{1}{2\pi} \int_{-\infty}^{\infty} \hat{x}(\omega) \frac{d^n}{dt^n} e^{i\omega t} d\omega \quad (2.4)$$

$$= \frac{1}{2\pi} \int_{-\infty}^{\infty} (i\omega)^n \hat{x}(\omega) e^{i\omega t} d\omega \quad (2.5)$$

leads to the FT of derivatives

$$\mathcal{F} \frac{d^n}{dt^n} x(t) = (i\omega)^n \hat{x}(\omega). \quad (2.6)$$

Assuming the damping force is linear, one can now rewrite eq. (2.1) in the frequency domain using eq. (2.6)

$$[-m\omega^2 + i\phi(\omega)k + k] \hat{x}(\omega) = \hat{F}_{\text{ext}}(\omega) \quad (2.7)$$

with a loss angle $\phi(\omega)$ that depends on the particular damping force. Thus, linear damping can be described by a complex spring constant $\tilde{k}(\omega) = k(1 + i\phi(\omega))$. In terms of the oscillator's natural frequency $\omega_0 = \sqrt{k/m}$ eq. (2.7) reads

$$[-m\omega^2 + m\omega_0^2(1 + i\phi(\omega))] \hat{x}(\omega) = \hat{F}_{\text{ext}}(\omega). \quad (2.8)$$

Hence, the transfer function H from external force to oscillator displacement is

$$H(\omega) = \frac{\hat{x}(\omega)}{\hat{F}_{\text{ext}}(\omega)} = \frac{1}{-m\omega^2 + m\omega_0^2(1 + i\phi(\omega))}. \quad (2.9)$$

2.2. Damping Forces

There are multiple models that can describe the damping forces in a physical system which originate from different processes, for example linear and nonlinear thermo-elastic, viscous and structural damping [20]. For linear damping forces the corresponding loss angles add up to a total loss angle

$$\phi_{\text{total}} = \sum_i \phi_i. \quad (2.10)$$

2.2.1. Quality Factor

The quality factor or Q factor characterizes the dissipation of a system that is driven at its eigenfrequency f_0 [21, ch. 7.5]. It can be defined by the ratio of the total energy stored in the system and the energy that is dissipated per radian [22, p. 42]

$$Q = 2\pi \frac{\text{total energy}}{\text{energy dissipated per cycle}}. \quad (2.11)$$

Thus a large Q means less dissipation. Another common definition uses the resonance frequency f_r and the full width at half maximum (FWHM) Δf of the power spectrum [21, ch. 7.5]

$$Q = \frac{f_r}{\Delta f} = \frac{\omega_r}{\Delta \omega}. \quad (2.12)$$

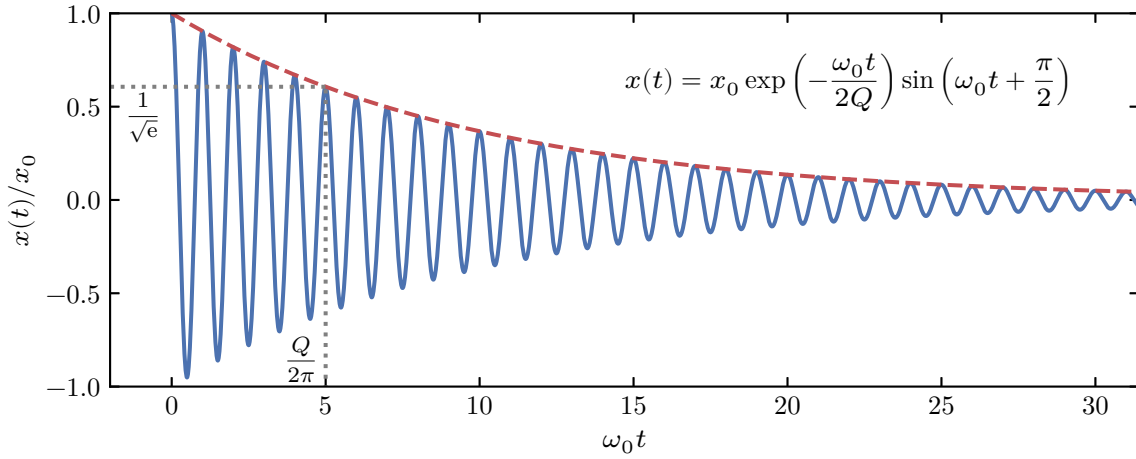


Figure 2.1.: Ringdown of a damped harmonic oscillator with $Q = 5 \cdot 2\pi$. It takes 5 oscillations for the amplitude to drop down to a fraction of $\frac{1}{\sqrt{e}} \approx 0.6$. The envelope is an exponential decay.

For large Q , these two definitions become approximately identical. It can be expressed as the inverse of the loss angle at the eigenfrequency

$$Q = \frac{1}{\phi(\omega_0)}. \quad (2.13)$$

Hence, as can be seen from eq. (2.10), Q factors add up inversely

$$\frac{1}{Q_{\text{total}}} = \sum_i \frac{1}{Q_i}. \quad (2.14)$$

The amplitude $x(t)$ of an excited damped harmonic oscillator decays exponentially with a time constant that is related to the Q factor

$$x(t) = x_0 \exp\left(-\frac{\omega_0 t}{2Q}\right) \sin(\omega_0 t + \phi). \quad (2.15)$$

$\frac{Q}{2\pi}$ is the number of oscillations it takes for the amplitude to drop down to a fraction of $\frac{1}{\sqrt{e}} \approx 0.6$. An example of such a ring-down is shown in fig. 2.1 for a Q factor $Q = 5 \cdot 2\pi$.

2.2.2. Viscous Damping

The viscous damping force

$$F_{\text{damp,vis}} = m\Gamma \dot{x}(t) \quad (2.16)$$

is proportional to the oscillators velocity $\dot{x}(t)$ with the damping coefficient Γ . This leads to a loss angle

$$\phi_{\text{vis}}(\omega) = \frac{\omega\Gamma}{\omega_0^2} \quad (2.17)$$

that is frequency dependent. The Q factor is

$$Q_{\text{vis}} = \frac{\omega_0}{\Gamma}. \quad (2.18)$$

Viscous damping is often used to model motion through a fluid.

2.2.3. Structural Damping

Structural or hysteresis damping can be described by a frequency independent loss angle

$$\phi(\omega) = \phi_{\text{struc}}. \quad (2.19)$$

In this case, the damping force is simply proportional to the oscillator's displacement, but lags behind with a phase of 90° . Structural damping is used to model internal losses in the oscillator's material. The Q factor is simply

$$Q_{\text{struc}} = \frac{1}{\phi_{\text{struc}}}. \quad (2.20)$$

2.3. Spectral Density

The PSD S_{xx} for a wide-sense stationarity (WSS) process $x(t)$ is given by the FT of its auto-correlation function

$$R_{xx}(\tau) = \int_{-\infty}^{\infty} x(t+\tau)x^*(t) dt, \quad (2.21)$$

with x^* being the complex conjugate, yielding [23]

$$S_{xx}(\omega) = \int_{-\infty}^{\infty} R_{xx}(\tau)e^{-i\omega\tau} d\tau. \quad (2.22)$$

It describes the power distribution of the signal in frequency domain. The average power in a frequency band $[\omega_1, \omega_2]$ can be calculated by integrating the PSD

$$\bar{P}_{[\omega_1, \omega_2]} = \frac{1}{2\pi} \int_{\omega_1}^{\omega_2} S_{xx}(\omega) d\omega. \quad (2.23)$$

The mean square value of the signal is given by integrating over all frequencies

$$\langle x^2 \rangle = \bar{P}_{[-\infty, \infty]} = \frac{1}{2\pi} \int_{-\infty}^{\infty} S_{xx}(\omega) d\omega. \quad (2.24)$$

If two WSS processes x and y are related via a transfer function $H(\omega) = \frac{\hat{x}(\omega)}{\hat{y}(\omega)}$, one can calculate the PSD S_{xx} from S_{yy} via

$$S_{xx}(\omega) = |H(\omega)|^2 \cdot S_{yy}(\omega). \quad (2.25)$$

The unit of the PSD is given in squared units of the signal x : $[S_{xx}] = \frac{[x]^2}{s^{-1}}$. Sometimes it is more convenient to display linear units of the signal, hence one defines the amplitude spectral density (ASD) as $\text{ASD} = \sqrt{\text{PSD}}$ with unit $[\text{ASD}] = \frac{[x]}{\sqrt{s^{-1}}}$. However, for calculation the PSD should be used.

Since the PSD is symmetric $S_{xx}(-\omega) = S_{xx}(\omega)$, one can define the single-sided PSD $S_{xx}^{\text{ss}}(\omega) = 2S_{xx}$ that is valid for frequencies $\omega > 0$. It is useful e.g. for spectrum analyzers that do not distinguish positive and negative frequencies.

2.4. Thermal Noise

In 1928, J. B. Johnson discovered the temperature dependent voltage noise in a resistor without supplied current [24] that was explained by H. Nyquist with the fluctuation–dissipation theorem (FDT) [25]. It was formally proven in 1951 by Callen and Welton [26] and later expanded by Kubo [27]. The FDT states that a process in thermal equilibrium which dissipates energy to a thermal bath experiences fluctuations driven by this bath. It associates the thermal noise PSD to the imaginary part of the transfer function H from a random thermal force F_{th} to the observable x . For frequencies ω , with $\hbar\omega \ll k_{\text{B}}T$, the equipartition theorem holds, where F_{th} has a white noise spectrum, and the FDT is given by [26]

$$S_{xx}(\omega) = -\frac{2k_{\text{B}}T}{\omega} \text{Im}(H(\omega)) \quad (2.26)$$

with temperature T and Boltzmann constant k_{B} .

For the harmonic oscillator transfer function (eq. (2.9)) the single-sided thermal noise spectrum reads

$$S_{xx}^{\text{ss}}(\omega) = \frac{4k_{\text{B}}T\phi\omega_0^2}{m\omega [(\omega^2 - \omega_0^2)^2 + \phi^2\omega_0^4]}. \quad (2.27)$$

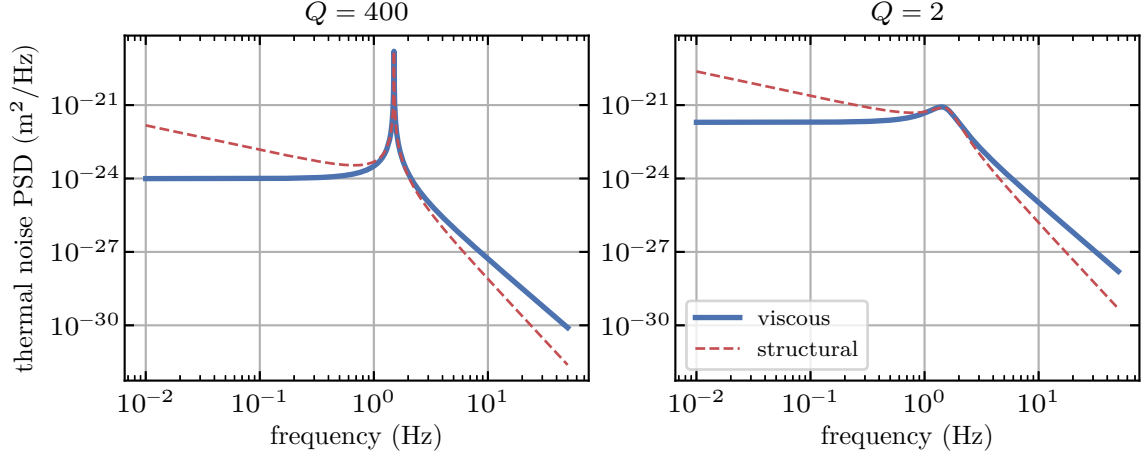


Figure 2.2.: Thermal noise PSD for an oscillator with $m = 50$ g at room temperature $T = 300$ K and an eigenfrequency $f_0 = 1.5$ Hz for two different Q factors. The resonance peak broadens for a smaller Q factor and the maximum height decreases but the integral under the curves stays the same since the temperature is proportional to it.

Using eqs. (2.18) and (2.20) one can write eq. (2.27) for viscous and structural damping in terms of the Q factor as

$$S_{xx,\text{vis}}^{\text{ss}}(\omega) = \frac{4Q_{\text{vis}}k_B T \omega_0}{m \left(Q_{\text{vis}}^2 (\omega^2 - \omega_0^2)^2 + \omega^2 \omega_0^2 \right)} \quad (2.28)$$

and

$$S_{xx,\text{struc}}^{\text{ss}}(\omega) = \frac{4Q_{\text{struc}}k_B T \omega_0^2}{m\omega \left(Q_{\text{struc}}^2 (\omega^2 - \omega_0^2)^2 + \omega_0^4 \right)}. \quad (2.29)$$

These two are identical at the eigenfrequency ω_0 but the latter has a $1/\omega$ slope instead of a constant for lower frequencies and drops down faster with a slope of $1/\omega^5$ compared $1/\omega^4$ in the viscous case [21, p. 120]. This is illustrated in fig. 2.2 for an oscillator with $m = 50$ g at room temperature $T = 300$ K and an eigenfrequency $f_0 = 1.5$ Hz with two different Q factors. The resonance peak broadens for a smaller Q factor and the maximum height decreases but the integral under the curves stays the same since the temperature is proportional to it.

2.5. Non-thermal Noise

When the oscillator is not in thermal equilibrium but is driven by a force with much larger PSD than the thermal force, the fluctuations due to the thermal bath can be neglected. The bath only contributes via the dissipation and the fluctuations solely result due to the driving force. Hence, the PSD of the oscillators motion is

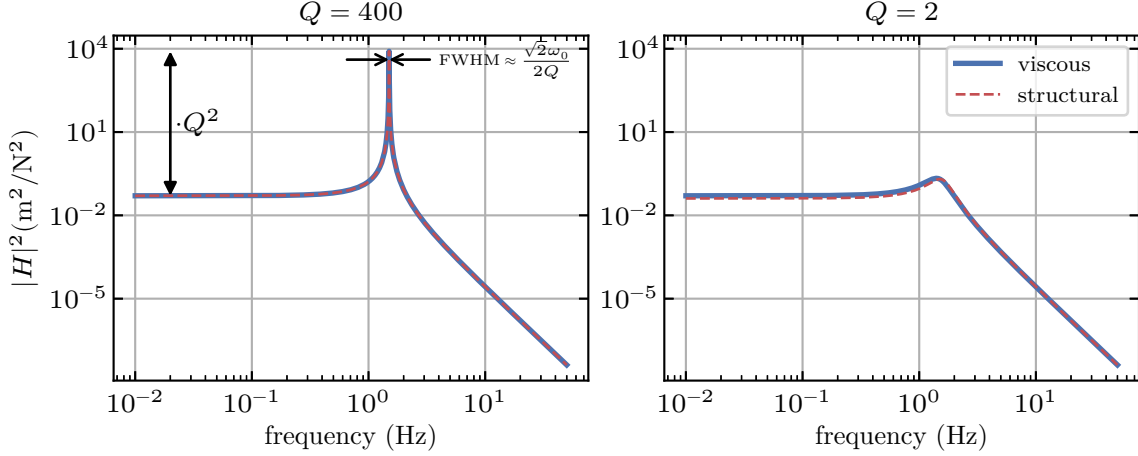


Figure 2.3.: PSD transfer function $|H|^2$ for an oscillator with $m = 50$ g at room temperature $T = 300$ K and an eigenfrequency $f_0 = 1.5$ Hz for two different Q factors. For large Q factors there is no difference between viscous and structural damping.

not governed by the imaginary part of the transfer function anymore but by the absolute value squared via eq. (2.25). For viscous and structural damping these read

$$|H_{\text{vis}}|^2 = \frac{Q_{\text{vis}}^2}{m^2 (Q_{\text{vis}}^2 (\omega^2 - \omega_0^2)^2 + \omega^2 \omega_0^2)} \quad (2.30)$$

and

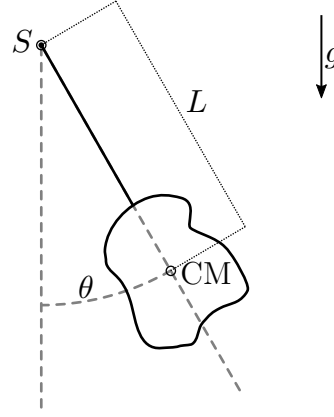
$$|H_{\text{struc}}|^2 = \frac{Q_{\text{struc}}^2}{m^2 (Q_{\text{struc}}^2 (\omega^2 - \omega_0^2)^2 + \omega_0^4)}, \quad (2.31)$$

respectively. The only difference between these two is the second term in the denominator which is neglectable for higher Q factors. This is shown in fig. 2.3 for the same parameters as in the thermal case above. For $Q = 400$ there is basically no difference between viscous and structural damping. For $Q = 2$ the maximum is shifted very slightly but the overall frequency dependence for both damping types is the same contrary to the thermal case. For large Q factors, the maximum value is scaled by a factor of Q^2 compared to the value at $\omega = 0$. The FWHM of the curve is given by $\frac{\sqrt{2}\omega_0}{2Q}$.

2.6. Gravity Pendulum

An oscillator where the restoring force is due to gravity is called a gravity pendulum. In its most simple form, one can describe such a pendulum by a point mass that is suspended by a massless wire and moves in a plane. Although this is oftentimes a good approximation, it can lead to deviations for systems with extended masses.

Figure 2.4: Gravity pendulum with an extended mass suspended by a massless wire from the suspension point S with deflection angle θ and pendulum length L . The acceleration due to gravity is g .



Such a system is shown in fig. 2.4. The distance from the suspension point S to the center of mass (CM) is denoted by L and the deflection angle of the CM from the resting position is given by θ .

In order to describe such a system with an EOM, it is beneficial to look at the torques that are involved. Equating the torque due to the moment of inertia I and the restoring torque due to gravity leads to the EOM for a pendulum without damping

$$I\ddot{\theta}(t) = -mgL \sin \theta(t), \quad (2.32)$$

where g is the standard acceleration due to gravity. Using the small angle approximation $\sin \theta \approx \theta$ leads to

$$I\ddot{\theta}(t) = -mgL\theta(t). \quad (2.33)$$

Adding a linear damping torque τ_{damp} and an external torque τ_{ext} we get

$$I\ddot{\theta}(t) + \tau_{\text{damp}}(\theta(t), \dot{\theta}(t)) + I\omega_0^2\theta(t) = \tau_{\text{ext}}(t) \quad (2.34)$$

with the eigenfrequency

$$\omega_0 = \sqrt{\frac{mgL}{I}}. \quad (2.35)$$

It is similar to eq. (2.1) and can be equivalently solved. In the simple case of a point mass, the moment of inertia is given by $I = mL^2$ yielding

$$\omega_0 = \sqrt{\frac{g}{L}} \quad (2.36)$$

which is independent of the suspended mass. [28, ch. 2.1.1.5]

2.6.1. Q Factor, Dilution Factor

A gravity pendulum stores energy in the gravitational field which is lossless. This would result in an infinite Q factor. However, in physical pendulums there is always

loss present. The suspension wire for example has to bend slightly to allow the mass to swing. This loss can be modeled as structural loss in the wire material. The energy E_{bend} that is stored in this bending is typically small compared to the energy E_g that is stored in the gravitational field. The loss for the gravity pendulum according to eqs. (2.11) and (2.13) is thus given by

$$\phi_{\text{pen}} = \frac{E_{\text{loss}}}{2\pi(E_g + E_{\text{bend}})} \approx \frac{E_{\text{loss}}}{2\pi E_g}. \quad (2.37)$$

The lost energy can be expressed via the loss factor of the wire as $E_{\text{loss}} = 2\pi E_{\text{bend}} \phi_{\text{bend}}$ resulting in

$$\phi_{\text{pen}} = \phi_{\text{bend}} \frac{E_{\text{bend}}}{E_g} = D \phi_{\text{bend}}. \quad (2.38)$$

The factor $D = \frac{E_{\text{bend}}}{E_g}$ is called the dilution factor of the pendulum. For small angles this can be expressed as

$$D = \frac{N\sqrt{TEI_{\text{wire}}}}{2mgL} \quad (2.39)$$

where N is the number of suspension wires, T the tension fo the wires, E the Young's modulus of the wire material and I_{wire} the moment of inertia of the wire. For wires with circular cross section of radius r this is given by $I_{\text{wire}} = \frac{\pi}{2}r^4$. [29]

2.6.2. Residual Gas Damping

The limiting factor for the Q factor of a pendulum in atmospheric pressure is the viscous damping of the surrounding gas. In order to reduce this loss mechanism, one can install the pendulum inside of a vacuum chamber and reduce the residual gas pressure. The Q factor of the gas damped pendulum is given by [30]

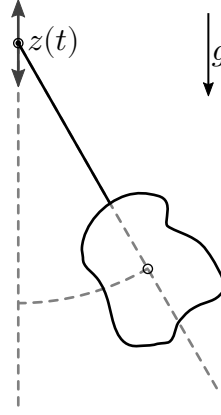
$$Q_{\text{gas}} = 4 \frac{m}{A} \frac{\omega_0}{P} \sqrt{\frac{\pi k_B T}{8\mu}} \quad (2.40)$$

where A is the surface area of the pendulum in the direction of motion, P is the residual gas pressure and μ the molecular mass of the gas molecule (often H_2 or N_2).

2.7. Parametric Damping

Periodically changing a parameter of an oscillator can extract energy from or transfer energy into the system. A familiar example for this is a person on a swing periodically stretching and tightening the legs, which effectively changes the moment of

Figure 2.5: Parametrically driven pendulum. The suspension point is moved periodically up and down with the modulation $z(t)$.



inertia and thus the eigenfrequency. This leads to an energy gain without an external force acting on the system. Such systems are called *parametrically driven oscillators*. Depending on the phase of the parameter change relative to the oscillator's motion, it can also reduce the energy. This is called parametric damping.

Another way to introduce a parametric drive for a suspended pendulum is moving the suspension point periodically up and down with an acceleration

$$\ddot{z}(t) = z_0 \Omega^2 \sin(\Omega t + \phi) \quad (2.41)$$

as shown in fig. 2.5. This effectively changes the gravitational acceleration ($g \rightarrow g + \ddot{z}(t)$) in eq. (2.35) and thus gives a time dependent eigenfrequency

$$\omega_0(t) = \sqrt{\frac{m(g + \ddot{z}(t))L}{I}}. \quad (2.42)$$

The optimal parametric gain is achieved for $\Omega = 2\omega_0$, but it also works at the eigenfrequency of the oscillator $\Omega = \omega_0$. Over time, the oscillator adjusts its relative phase $\Delta\phi$ such, that $\Delta\phi = 0$, which corresponds to the case of maximum energy transfer to the oscillator (parametric heating). In order to remove energy consistently from the oscillator, the relative phase has to be actively stabilized to $\Delta\phi = \pi$. The corresponding parametric Q factor is [31, p. 27]

$$Q_{\text{parametric}} = -\frac{1}{2 \cos(\Delta\phi)} \frac{L}{z_0}, \quad (2.43)$$

where a negative Q factor resembles parametric heating. Note that it is proportional to the fraction of the parametric modulation amplitude z_0 to the length of the pendulum L .

A detailed overview of the theory for parametrically driven oscillators can be found in the master's thesis of Daniel Hartwig [31] that I supervised during the course of this work. The integration of parametric damping into the *MassQ* experiment will be described in detail in his upcoming PhD thesis. A possible application of parametric damping in gravitational-wave detectors can be found in [19].

3. Laser Interferometers

Laser interferometers in multiple variations are a well established tool for precision experiment. In 1887, Michelson and Morley carried out the well known experiment on the luminiferous ether with the later called Michelson interferometer [5], which ultimately paved the way for Einstein's theory of relativity [32]. In 1925, Michelson and Gale used another interferometer topology, the Sagnac-Interferometer, to measure the rotation of the earth. Today, Michelson interferometers are used as precision instruments in gravitational-wave observatories [1, 34] to detect the stretching of spacetime due to gravitational waves. A Michelson interferometer can also be used to measure the refractive index of optical materials [35]. Sagnac interferometers in form of fiber-optic gyroscopes are used for precision navigation [36]. In this chapter, I describe the theory of a combined Michelson-Sagnac interferometer topology and discuss the special cases of a pure Michelson or Sagnac interferometer, respectively. Furthermore, I give an overview of Fabry-Perot resonators and optical cavities as well as noise sources of a Michelson-Sagnac interferometer for both quantum and classical noise. At last, I introduce power- and signal-recycling techniques, which can enhance the interferometer sensitivity.

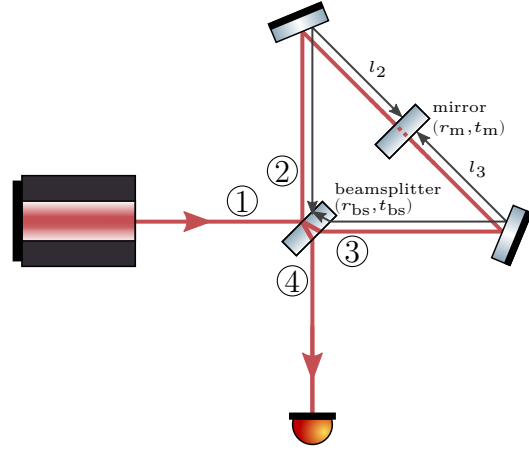
3.1. Michelson-Sagnac Topology

A Sagnac interferometer is created by splitting a laser beam with a beamsplitter and using steering mirrors to reflect the beams such that they are counter propagating in a loop and finally recombined on the beamsplitter. Placing a partly reflective mirror with amplitude reflection and transmission coefficients r_m and t_m inside the loop creates an additional Michelson mode from the two reflected parts of the beam forming a Michelson-Sagnac interferometer. A schematic view of this configuration is shown in fig. 3.1.

This interferometer topology has been studied in [9, 10, 11] and used in experiments such as [37, 12, 14]. The following derivation of the input-output relations is based on [12, 37].

I assume a single input field a_{in} that is incident on port 1 of the beamsplitter with

Figure 3.1: Michelson-Sagnac interferometer topology. Light from the input port 1 is split on a beamsplitter with amplitude reflectivity r_{bs} into two arms exiting port 2 and 3. Two steering mirrors form a loop for the counter propagating beams. A partly reflective common mirror with reflectivity r_m reflects part of the beams which then form the Michelson mode. The beams are overlapped again on the beamsplitter and are measured with a detector in the output port 4. The arm lengths l_2 and l_3 are given by the optical path length from the beamsplitter to the reflective surface of the common end mirror.



ports 1 to 4 as indicated in fig. 3.1. The amplitude reflection and transmission coefficients at the beamsplitter r_{ij} and t_{ij} , respectively, are complex numbers and can be written in polar form as

$$r_{ij} = r_{bs} e^{i\theta_{ij}} \quad (3.1)$$

$$t_{ij} = t_{bs} e^{i\theta_{ij}}. \quad (3.2)$$

Here, i denotes the input port and j the output port with $i, j \in \{1, 2, 3, 4\}$. In order to fulfill energy conservation for a lossless beamsplitter,

$$r_{bs}^2 + t_{bs}^2 = 1 \quad (3.3)$$

must hold and an overall phase of π has to be accumulated with

$$(\theta_{12} + \theta_{34}) - (\theta_{13} + \theta_{24}) = \pm\pi. \quad (3.4)$$

For simplicity, the phase flip can be set to a single reflection with $\theta_{12} = \pi$ and $\theta_{34} = \theta_{13} = \theta_{24} = 0$.

The transmitted field amplitude a_{trans} in port 4 is the sum of two Sagnac and two Michelson fields with different phases and is given by

$$a_{trans} = a_{in} \left[\underbrace{t_m r_{bs}^2 e^{i\theta_{S1}^t} + t_m t_{bs}^2 e^{i\theta_{S2}^t}}_{\text{Sagnac}} + \underbrace{r_m r_{bs} t_{bs} e^{i\theta_{M1}^t} + r_m r_{bs} t_{bs} e^{i\theta_{M2}^t}}_{\text{Michelson}} \right] \quad (3.5)$$

with the acquired phases

$$\theta_{S1}^t = \theta_{12} + \theta_{34} + \theta_m^t + k(l_2 + l_3) \quad (3.6)$$

$$\theta_{S2}^t = \theta_{13} + \theta_{24} + \theta_m^t + k(l_2 + l_3) \quad (3.7)$$

$$\theta_{M1}^t = \theta_{12} + \theta_{24} + \theta_m^r + 2kl_2 \quad (3.8)$$

$$\theta_{M2}^t = \theta_{13} + \theta_{34} + \theta_m^r + 2kl_3, \quad (3.9)$$

where $k = \frac{2\pi}{\lambda}$ is the wave number with the laser wavelength λ and θ_m^t and θ_m^r are phases that are acquired on transmission or reflection on the mirror, respectively. The length of the interferometer arms, that is the distance from the beamsplitter to the mirror, are l_2 and l_3 for the two beamsplitter ports 2 and 3, respectively. For the transmitted field, the two Sagnac fields experience two transmissions through or reflections off the beamsplitter while the Michelson fields each get a single transmission and reflection. Using the phase relation eq. (3.4) and the identity

$$e^{ix} + e^{iy} = e^{i\frac{x+y}{2}} \cdot 2 \cos\left(\frac{x-y}{2}\right), \quad (3.10)$$

we can simplify the transmission coefficient for the interferometer to

$$t_{\text{ifo}} = \frac{a_{\text{trans}}}{a_{\text{in}}} = \underbrace{t_m e^{i\theta_{S1}^t} (r_{\text{bs}}^2 - t_{\text{bs}}^2)}_{\text{Sagnac}} + \underbrace{2r_m r_{\text{bs}} t_{\text{bs}} e^{i\frac{\theta_{M1}^t + \theta_{M2}^t}{2}} \cos\left(\frac{\theta_{M1}^t - \theta_{M2}^t}{2}\right)}_{\text{Michelson}}. \quad (3.11)$$

The Michelson mode is sensitive to the arm length difference $\Delta l = l_2 - l_3$.

Similarly, the reflected field amplitude is again the sum of 4 fields yielding

$$a_{\text{ref}} = a_{\text{in}} \left[\underbrace{t_m r_{\text{bs}} t_{\text{bs}} e^{i\theta_{S1}^r} + t_m r_{\text{bs}} t_{\text{bs}} e^{i\theta_{S2}^r}}_{\text{Sagnac}} + \underbrace{r_m r_{\text{bs}}^2 e^{i\theta_{M1}^r} + r_m t_{\text{bs}}^2 e^{i\theta_{M2}^r}}_{\text{Michelson}} \right], \quad (3.12)$$

but this time the two Michelson fields experience two transmissions or reflections. The acquired phases are

$$\theta_{S1}^r = \theta_{12} + \theta_{13} + \theta_m^t + k(l_2 + l_3) \quad (3.13)$$

$$\theta_{S2}^r = \theta_{13} + \theta_{12} + \theta_m^t + k(l_2 + l_3) \quad (3.14)$$

$$\theta_{M1}^r = \theta_{12} + \theta_{12} + \theta_m^r + 2kl_2 \quad (3.15)$$

$$\theta_{M2}^r = \theta_{13} + \theta_{13} + \theta_m^r + 2kl_3. \quad (3.16)$$

Using the fact that $\theta_{S1}^r = \theta_{S2}^r$, the reflection coefficient for the interferometer can be simplified to

$$r_{\text{ifo}} = \frac{a_{\text{ref}}}{a_{\text{in}}} = \underbrace{2t_m r_{\text{bs}} t_{\text{bs}} e^{i\theta_{S1}^r}}_{\text{Sagnac}} + \underbrace{r_m r_{\text{bs}}^2 e^{i\theta_{M1}^r} + r_m t_{\text{bs}}^2 e^{i\theta_{M2}^r}}_{\text{Michelson}}. \quad (3.17)$$

In the following, the two edge cases of a pure Michelson or Sagnac interferometer are discussed further, since these cases are relevant for the *MassQ* experiment.

3.1.1. Michelson Interferometer

Using a perfectly reflecting mirror with $t_m = 0$, the Sagnac mode vanishes and the interferometer is reduced to a pure Michelson interferometer with a common end

mirror for both arms. The same is true for a balanced beamsplitter with $\Delta_{\text{bs}} = r_{\text{bs}}^2 - t_{\text{bs}}^2 = 0$, since in this case the two Sagnac fields interfere destructively. The behavior is that of a Michelson interferometer where the input field is just scaled by the mirror reflectivity r_{m} . The normalized transmitted power is then given by

$$\begin{aligned} T_{\text{ifo}} &= \frac{P_{\text{trans}}}{P_{\text{in}}} = \left| \frac{a_{\text{trans}}}{a_{\text{in}}} \right|^2 \\ &= 4r_{\text{m}}^2 r_{\text{bs}}^2 t_{\text{bs}}^2 \cos^2 \left(\underbrace{\frac{2\pi}{\lambda} \Delta l + \theta^{\text{t}}}_{\delta} \right) \\ &= 2r_{\text{m}}^2 r_{\text{bs}}^2 t_{\text{bs}}^2 (1 + \cos(2\delta)) \end{aligned} \quad (3.18)$$

with the input power $P_{\text{in}} = |a_{\text{in}}|^2$ and total phase $\theta^{\text{t}} = \frac{(\theta_{12} + \theta_{24}) - (\theta_{13} + \theta_{34})}{2}$. The normalized reflected power is then

$$R_{\text{ifo}} = 1 - T_{\text{ifo}} \quad (3.19)$$

which reflects the energy conservation. A detuning $\delta = n\pi$ with $n \in \mathbb{Z}$ maximizes T_{ifo} while $\delta = n\pi + \frac{\pi}{2}$ leads to a dark output. These conditions are called *bright fringe* and *dark fringe*, respectively. $\delta = (2n - 1)\frac{\pi}{4}$ is the point with the maximal sensitivity to an arm length change which is called *mid fringe*.

Equation (3.18) can be rewritten in terms of oscillator displacement x from an equilibrium position Δl_0 . The arm length difference changes with twice the oscillator displacement ($\Delta l = \Delta l_0 + 2x$) and thus

$$T_{\text{ifo}}(x) = 4r_{\text{m}}^2 r_{\text{bs}}^2 t_{\text{bs}}^2 \cos^2 \left(\frac{4\pi}{\lambda} x + \Phi_0 \right) \quad (3.20)$$

with a detuning $\Phi_0 = \frac{\pi}{\lambda} \Delta l_0 + \theta^{\text{t}}$ that can be tuned by changing the equilibrium position Δl_0 . For small displacements, eq. (3.20) can be approximated with a Taylor expansion

$$T_{\text{ifo}}(x) = 4r_{\text{m}}^2 r_{\text{bs}}^2 t_{\text{bs}}^2 \cos^2 \Phi_0 - \frac{32\pi r_{\text{m}}^2 r_{\text{bs}}^2 t_{\text{bs}}^2 \sin \Phi_0 \cos \Phi_0}{\lambda} x. \quad (3.21)$$

3.1.2. Sagnac Interferometer

Removing the mirror, thus setting $t_{\text{m}} = 1$, leads to a pure Sagnac interferometer which is not sensitive to differential arm length changes but only to rotations of the interferometer. For a non-rotating interferometer, the normalized output power only depends on the beamsplitter imbalance and reads

$$\frac{P_{\text{trans}}}{P_{\text{in}}} = T_{\text{ifo}} = \Delta_{\text{bs}}^2. \quad (3.22)$$

For a balanced beamsplitter and perfect beam overlap, the output port is completely dark. For a real Sagnac interferometer there is always minimal misalignment present. This would increase the output power from which an upper bound for the beamsplitter imbalance can be estimated from the best possible alignment as $\Delta_{\text{bs}} \leq \sqrt{T_{\text{ifo}}}$

Influence of Rotations

In a rotating Sagnac interferometer, the two counter propagating beams experience a relative phase shift

$$\Delta\delta = \frac{4}{\lambda c} \vec{\omega} \vec{A} \quad (3.23)$$

that depends on the area of the Sagnac loop \vec{A} and the angular velocity of the rotation $\vec{\omega}$. Michelson and Gale used this in 1925 to measure the rotation of the earth [38, 33] with an interferometer area of around 0.2 km^2 .

In order to estimate this effect for the *MassQ* experiment, we can calculate the phase shift for Hamburg

$$\Delta\delta_{\text{MassQ}} = \frac{4}{\lambda c} \omega A \cos(90^\circ - \text{LAT}) \approx 10^{-7} \text{ rad} \quad (3.24)$$

with a latitude $\text{LAT} = 53^\circ 33'$ for an area $A = 0.25 \text{ m}^2$, $\lambda = 1550 \text{ nm}$ and angular velocity $\omega = 2\pi \text{ rad d}^{-1}$. This would be equivalent to a beam splitter imbalance $\Delta_{\text{bs}} \approx 10^{-7}$, which is neglectable to the realistically expected imbalance of around 10^{-3} .

3.2. Interferometer Contrast

The calculations above use a plane wave approximation for the laser. However, in reality a laser is described by a Gaussian beam. If the two modes of the beams at the output do not overlap perfectly, they cannot interfere complete destructively resulting in nonzero output power even for tuning to the dark fringe. We can define the interferometer contrast [12, p. 39]

$$C = \frac{P_{\text{max}} - P_{\text{min}}}{P_{\text{max}} + P_{\text{min}}} \quad (3.25)$$

where P_{max} and P_{min} are the maximally and minimally achievable output powers, respectively, and rewrite eq. (3.18) to

$$T_{\text{ifo}} = 2r_{\text{m}}^2 r_{\text{bs}}^2 t_{\text{bs}}^2 (1 + C \cdot \cos(2\delta)) \quad (3.26)$$

such that the contrast is included.

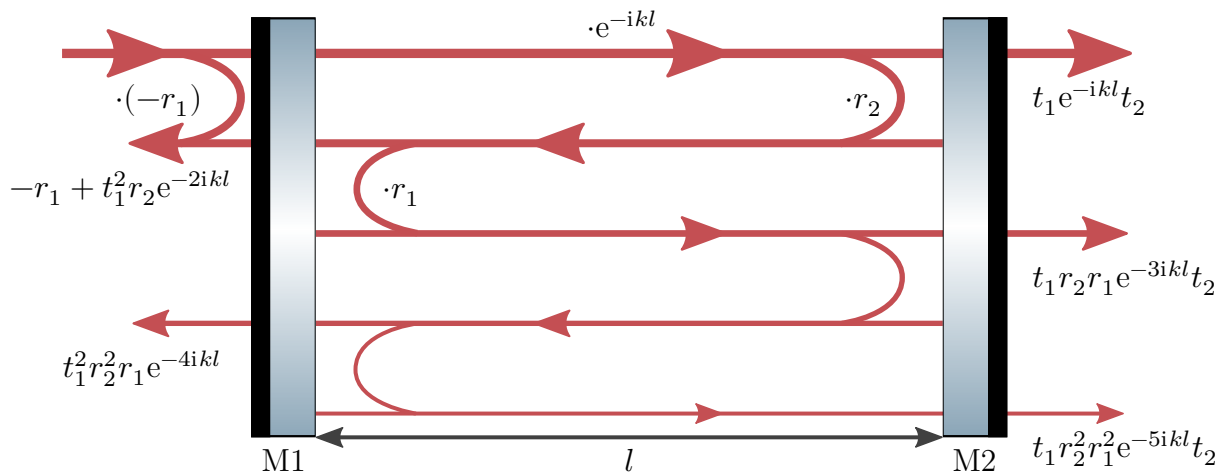


Figure 3.2.: Fabry-Perot resonator with mirrors M1 and M2 with a cavity length l . The first terms of the infinite sum for the amplitude transmissivity and reflectivity are shown. The factor e^{-ikl} is the phase accumulated by a single trip through the cavity. On the first reflection of M1 an additional phase of π is acquired, hence the minus sign.

3.3. Fabry-Perot Resonator

Another type of interferometer are optical resonators or cavities such as the Fabry-Perot resonator, which consists of two plane parallel mirrors M1 and M2 spaced a distance l apart. An incident light field gets partly transmitted and reflected on the first mirror M1. The transmitted field then travels through the resonator and gets again transmitted and reflected on mirror M2. The reflected part now travels back through the cavity and repeats the process infinitely. The resulting reflected and transmitted fields from the resonator are the infinite sum of all the fields traveling in the same direction.

In order to understand the basic operating principle, we treat this as a one-dimensional problem with plane waves as in [21, ch. 6.3] and assign a field reflectivity $r_{1,2}$ and transmissivity $t_{1,2}$ to mirrors M1 and M2, respectively. This is shown in fig. 3.2 with the first terms of the infinite series indicated. Assuming no loss with $r_{1,2}^2 + t_{1,2}^2 = 1$, the series is a geometric sum which can be expressed in a simple algebraic form, which yield the field transmissivity of the cavity

$$t_c = t_1 t_2 e^{-ikl} \sum_{n=0}^{\infty} (r_1 r_2 e^{-2ikl})^n = \frac{t_1 t_2 e^{-ikl}}{1 - r_1 r_2 e^{-2ikl}} \quad (3.27)$$

and analogously the cavity field reflectivity

$$r_c = -r_1 + t_1^2 r_2 e^{-2ikl} \sum_{n=0}^{\infty} (r_1 r_2 e^{-2ikl})^n = -r_1 + \frac{t_1^2 r_2 e^{-2ikl}}{1 - r_1 r_2 e^{-2ikl}}. \quad (3.28)$$

The first reflected field of M1 acquires an additional phase of π since the reflection occurs on an interface with switched refractive indices compared to all the other reflections, hence the $-r_1$ in the sum. The factor e^{-ikl} is the phase accumulated by a single trip through the cavity length l with the wave number k as defined above. In the case $kl = n\pi$, the circulating fields interfere constructively and the cavity is on resonance. In the case of an impedance matched cavity with $r_1 = r_2$ the transmission losses are exactly compensated by the transmission of the incoming field and all optical power is transmitted through the cavity. The power transmissivity $T_c = |t_c|^2$ and the phase of the transmitted light $\arg(t_c)$ for such an impedance matched cavity is shown in fig. 3.3 for different mirror reflectivities. The phase change around the resonance gets steeper for higher reflectivity and the width of the resonances becomes smaller. In frequency space, the distance between two resonances is called the free spectral range

$$\text{FSR} = \frac{c}{2l} \quad (3.29)$$

where c is the speed of light. The free spectral range (FSR) is related to the FWHM of the resonances or cavity linewidth

$$\Delta\nu = \frac{c}{\pi l} \arcsin \left[\frac{1 - r_1 r_2}{2\sqrt{r_1 r_2}} \right] \quad (3.30)$$

by the cavity finesse [39, p. 210]

$$\mathcal{F} = \frac{\text{FSR}}{\Delta\nu} \approx \frac{\pi\sqrt{r_1 r_2}}{1 - r_1 r_2}. \quad (3.31)$$

where the last approximation is valid for high finesse values with $\arcsin(x) \approx x$ for small x .

Around resonance, a cavity can be approximated as a one-pole low-pass filter with a corner frequency [39]

$$f_c = \frac{\Delta\nu}{2} \quad (3.32)$$

which attenuates signals outside the cavity bandwidth.

Mode Matching

The above discussion assumed plane waves and neglects the spatial beam profile. The incoming beam can be expressed in the basis of transverse electromagnetic modes (TEMs). These modes are described by a complex beam parameter q that is related to the beam curvature R and beam radius w as [40]

$$\frac{1}{q} = \frac{1}{R} - i \frac{\lambda}{\pi w^2}, \quad (3.33)$$

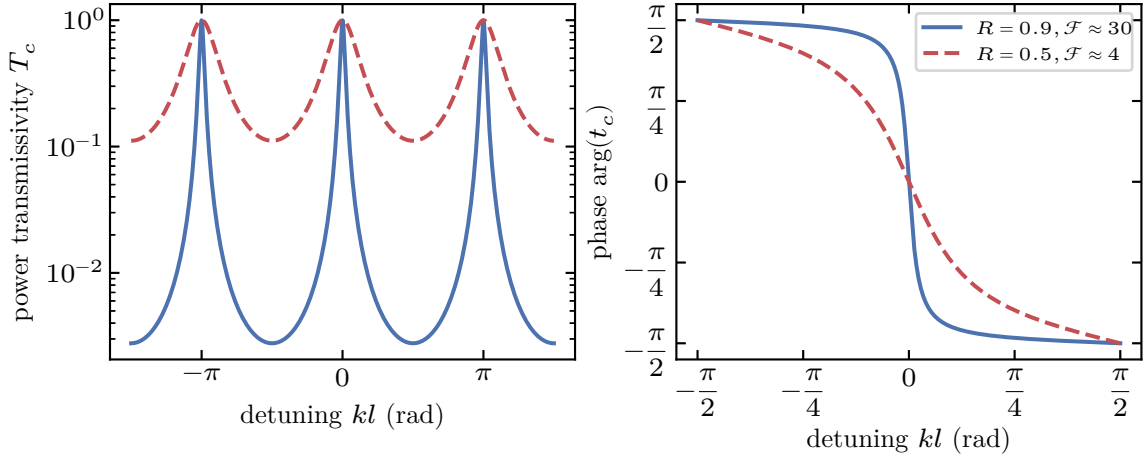


Figure 3.3.: Resonances of an impedance matched cavity for different mirror reflectivities R and thus different finesse values. Changing the cavity detuning kl either by cavity length or laser frequency leads to resonances for integer multiples of π .

Left: Logarithmic power transmissivity. On resonance, the transmissivity is 1. For higher finesse, the transmissivity on anti-resonance gets smaller.

Right: On resonance, the slope of the phase is maximal and gets steeper for higher finesse.

which is only determined by the resonator geometry. Compared to plane waves, these modes acquire an additional Gouy phase [40] which leads to different resonance lengths for the cavity modes. This allows the cavity to act as a spatial filter for the beam by tuning the resonance condition such that only the desired Gaussian mode is resonant. The incoming beam has to be matched to the desired mode by aligning the position and angle of the incoming beam to allow for maximum transmission. The unmatched part is reflected off the cavity.

Beam Size

The beam size of the cavity modes depends on the resonator geometry parameters as the mirror curvatures R_1 and R_2 and the resonator length l shown in fig. 3.4 as well as the wavelength λ and the refractive index n of the material between the mirrors. For an optical cavity to form, the wavefront curvature of the mode at the mirror needs to be equal to the curvature of the mirror surface. Following [40], the beam radii at the mirrors 1 and 2 are then given by

$$w_1 = \sqrt[4]{\left(\frac{\lambda R_1}{n\pi}\right)^2 \cdot \frac{R_2 - l}{R_1 - l} \cdot \frac{l}{R_1 + R_2 - l}} \quad (3.34)$$

$$w_2 = \sqrt[4]{\left(\frac{\lambda R_2}{n\pi}\right)^2 \cdot \frac{R_1 - l}{R_2 - l} \cdot \frac{l}{R_1 + R_2 - l}} \quad (3.35)$$

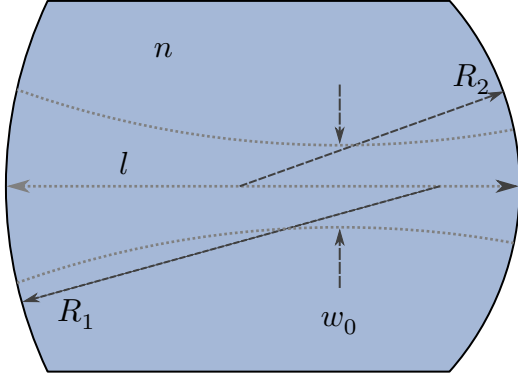


Figure 3.4: Resonator with surface curvatures R_1 and R_2 and cavity length l . The refractive index of the material in between the mirror surfaces is n . The gray dotted lines indicate the optical axis and the longitudinal mode shape with the beam waist w_0 .

and the waist size is

$$w_0 = \sqrt[4]{\left(\frac{\lambda}{n\pi}\right)^2 \frac{l(R_1 - l)(R_2 - l)(R_1 + R_2 - l)}{(R_1 + R_2 - 2l)^2}}. \quad (3.36)$$

The sign for the curvature is positive for convex surfaces with respect to the inside of the cavity as in fig. 3.4.

3.4. Quantum Noise of Position Measurements

Due to the quantum nature of light, a measurement of optical power is inherently a photon counting process. For a coherent field this is a Poisson process where the individual photons are uncorrelated [41]. This results in a single sided white noise spectral density for the photon flux n

$$S_{nn}^{\text{shot}} = 2\bar{n} \quad (3.37)$$

with the average flux $\bar{n} = \frac{P}{\hbar\omega}$, which is the optical power P divided by the photon energy $\hbar\omega = \hbar\frac{2\pi c}{\lambda}$. Using eq. (2.25), we can calculate the shot noise spectral density for the optical power [12, p. 9]

$$S_{PP}^{\text{shot}} = 2\hbar\frac{2\pi c}{\lambda}P = \frac{4\hbar\pi c}{\lambda}P. \quad (3.38)$$

The quantum noise in the interferometer manifests in two different ways, namely the detection shot noise and the back-action noise [42]. Since they scale opposite with light power, they cannot be reduced at the same time by changing the incoming laser power. This leads to the standard quantum limit (SQL) of interferometry which poses a limit on the sensitivity of a position measurement which can only be surpassed using non-classical states of light such as squeezed light [43].

3.4.1. Photon Shot Noise

For a laser interferometer, the detection shot noise can not be distinguished from power fluctuations due to a signal inside the interferometer which is why it is useful to express the shot noise PSD in terms of length units m^2/Hz by normalizing it to the change in output power due to a signal x . For the balanced interferometer from eq. (3.18) this yields

$$S_{xx}^{\text{shot}}(\delta) = \frac{S_{\text{PP}}^{\text{shot}}}{\left(\frac{dP_{\text{trans}}}{dx}\right)^2} = \frac{\hbar c \lambda}{16\pi r_m^2 P_{\text{in}}} \frac{1}{\sin^2(\Phi_0)}. \quad (3.39)$$

This function approaches a minimum value [9]

$$S_{xx}^{\text{shot}} = \frac{\hbar c \lambda}{16\pi r_m^2 P_{\text{in}}} \quad (3.40)$$

for $\Phi_0 \rightarrow n\frac{\pi}{2}$, which is the dark-fringe condition. However, at this point there is no signal at the output port, and thus the interferometer has to be operated slightly detuned from dark port when the signal is measured with a single photodiode.

3.4.2. Backaction Noise

Another manifestation of the Poissonian photon statistics inside the interferometer is the quantum radiation pressure noise or back-action noise [42]. The radiation pressure force exerted on a mirror by a laser with optical power P on reflection is

$$F_{\text{RP}} = \frac{2P}{c}, \quad (3.41)$$

where c is the speed of light. The noise spectral density for the optical power is again given by eq. (3.38). Using eq. (2.25) with the transfer function eq. (3.41), we can calculate the force noise spectral density from that:

$$S_{FF}^{\text{RPN}} = \left(\frac{2}{c}\right)^2 \frac{4\hbar\pi c}{\lambda} P = \frac{16\hbar\pi P}{c\lambda}. \quad (3.42)$$

In a balanced Michelson-Sagnac interferometer, the reflected optical power on one side of the mirror is $P = \frac{r_m^2 P_{\text{in}}}{2}$, yielding

$$S_{FF}^{\text{RPN}} = \frac{8\hbar\pi r_m^2 P_{\text{in}}}{c\lambda} \quad (3.43)$$

for the force noise on one mirror side. Due to energy conservation on the beamsplitter, these forces are anti-correlated [9] and the spectral densities add up, resulting in

$$S_{FF}^{\text{RPN}} = \frac{16\hbar\pi r_m^2 P_{\text{in}}}{c\lambda} \quad (3.44)$$

for the total radiation pressure force noise on the mirror. Again using eq. (2.25) with the harmonic oscillator displacement transfer function, we can express the radiation pressure noise in terms of oscillator displacement

$$S_{xx}^{\text{RPN}}(\omega) = |H(\omega)|^2 \cdot S_{FF}^{\text{RPN}} = |H(\omega)|^2 \cdot \frac{16\pi\hbar r_m^2 P_{\text{in}}}{c\lambda}. \quad (3.45)$$

3.4.3. Standard Quantum Limit

The shot noise in the position measurement and the back-action noise scale opposite with the incoming laser power P_{in} . While the shot noise decreases with higher power, the back-action noise on the oscillator is increased. The total quantum noise of the position measurement

$$S_{xx}^{\text{q}} = \frac{\hbar c\lambda}{16\pi r_m^2 P_{\text{in}}} + |H(\omega)|^2 \cdot \frac{16\pi\hbar r_m^2 P_{\text{in}}}{c\lambda} \quad (3.46)$$

is given by the sum of the individual PSDs since the noise is not correlated. We can now determine the minimum with respect to P_{in} with

$$\frac{dS_{xx}^{\text{q}}}{dP_{\text{in}}} = -\frac{\hbar c\lambda}{16\pi r_m^2 P_{\text{in}}^2} + |H(\omega)|^2 \cdot \frac{16\pi\hbar r_m^2}{c\lambda} = 0 \quad (3.47)$$

yielding the frequency dependent input power

$$P_{\text{SQL}}(\omega) = \frac{c\lambda}{16\pi r_m^2 |H(\omega)|} \quad (3.48)$$

required to reach the SQL for the Michelson-Sagnac interferometer [12, p. 36]

$$S_{xx}^{\text{SQL}}(\omega) = 2\hbar |H(\omega)|. \quad (3.49)$$

Well above the resonance frequency of a pendulum, the SQL approaches that of a free mass with transfer function

$$|H(\omega)| = \frac{1}{m\omega^2} \quad (3.50)$$

yielding the free mass SQL[2]

$$S_{xx}^{\text{fmSQL}}(\omega) = \frac{2\hbar}{m\omega^2}. \quad (3.51)$$

3.5. Classical Laser Noise

Additionally to quantum noise, the interferometer sensitivity can also be limited by classical laser noise in amplitude and frequency. This technical laser noise can have multiple origins such as a length change of the resonator or a fluctuating pump power [12, p. 41]. This section briefly describes the influence of these classical noise sources on the displacement measurement with the interferometer. A more detailed analysis can be found in [12, 44].

3.5.1. Amplitude Noise

Technical fluctuations of the laser power are characterized by the relative intensity noise (RIN)

$$\text{RIN}(\omega) = \frac{\sqrt{S_{\text{PP}}^{\text{laser}}(\omega)}}{\bar{P}} \quad (3.52)$$

which relates the ASD of the power fluctuations to the average laser power \bar{P} and is typically frequency dependent. The fluctuating power leads to a varying radiation pressure force in the mirror causing a corresponding displacement PSD [12, p. 43]

$$S_{xx}^{\text{RIN}}(\omega) = |H(\omega)|^2 \left(\frac{2r_{\text{m}}^2 \Delta_{\text{bs}}}{c} \right)^2 S_{\text{PP}}^{\text{laser}}(\omega) \quad (3.53)$$

which is dependent on the beamsplitter imbalance. For a perfectly balanced beamsplitter, the radiation pressure force from both sides of the mirror would cancel out and the mirror would not be influenced by the classical laser noise at all. Even for a non-balanced beamsplitter the radiation pressure effect is reduced with the Michelson-Sagnac topology compared to the classical Michelson design where the laser noise would always effect both end mirrors individually.

3.5.2. Phase Noise

Incoming laser phase noise results in a phase difference of the two interferometer arms

$$\Delta\theta(t) = \theta(t) - \theta(t + \Delta t) \quad (3.54)$$

depending on the time delay $\Delta t = \frac{\Delta l}{c}$ until the beams are recombined on the beamsplitter [45]. The time delay is determined by the path length difference Δl and the speed of light c . Using the linearity and time shifting properties of the

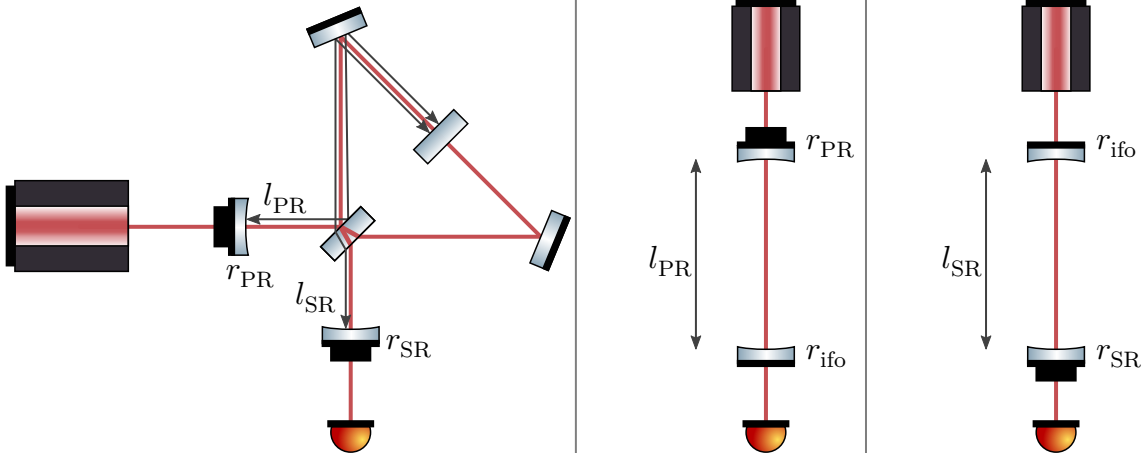


Figure 3.5.: Legend for the optics in fig. A.1.

Left: Recycled Michelson-Sagnac interferometer with recycling mirrors in the input and output port. The amplitude reflectivities are r_{PR} and r_{SR} for the PRM and for the SRM, respectively. The cavity length is the optical path length from the recycling mirror to the reflective surface of the common end mirror. **Middle:** Simplified model for the power-recycling cavity with length l_{PR} with the PRM as input mirror and the interferometer as effective output mirror with amplitude reflectivity r_{ifo} . **Right:** Simplified model for the signal-recycling cavity with length l_{SR} with the interferometer as effective input mirror and the SRM as output mirror.

Fourier transform, one can calculate the relation between the PSD of the phase difference to the PSD of the laser phase fluctuations [46]

$$S_{\Delta\theta\Delta\theta}(\omega) = 4 \sin^2 \left(\frac{\omega \Delta l}{2c} \right) S_{\theta\theta}(\omega). \quad (3.55)$$

Thus, laser phase fluctuation couple maximally for frequencies $\frac{\omega}{2\pi} = \frac{c}{2\Delta l}$, that is half of the interferometer's FSR. For a path length difference $\Delta l = 1$ cm, the maximum is at around 15 GHz. Thus, for frequencies up to 1 kHz, phase noise coupling should not be problematic. However, when signal recycling is used, this path length difference will be increased by the cavity round trips and phase noise coupling might demand for a laser phase noise stabilization [12].

3.6. Recycling Techniques

Only considering the input and output fields of an interferometer, we can view it as a simple mirror with variable amplitude transmissivity and reflectivity given by eqs. (3.11) and (3.17), respectively, that depend on the interferometer tuning. Using another mirror, one can now form a cavity. This mirror can either be placed in the

input or output port of the interferometer allowing for so called power- or signal-recycling, respectively, which can increase the interferometer sensitivity for certain frequencies. A schematic view of this setup is shown in fig. 3.5. The left side shows the power- and signal recycling mirror inside the interferometric setup while the right side shows the simplified view with the interferometer as a single mirror with amplitude reflectivity r_{ifo} . The cavity lengths for the power- and signal-recycling cavity are given by the optical path length from the recycling mirror to the reflective surface of the common end mirror as indicated in fig. 3.5. For the path inside the beamsplitter, one has to take into account the refractive index of the material n_{BS} .

3.6.1. Power Recycling

When the interferometer is tuned to dark fringe, it acts like a mirror with a power reflectivity $R_{\text{ifo}} = |r_{\text{ifo}}|^2 = 1$. The back-reflected light can now be sent back coherently into the interferometer by tuning the position of the power-recycling mirror (PRM) such that the resulting cavity is on resonance. This effectively increases the input power for the interferometer by the power buildup factor of the cavity. This is the power-recycling gain [9]

$$G_{\text{PR}} = \frac{1 + r_{\text{PR}}}{1 - r_{\text{PR}}} \quad (3.56)$$

where r_{PR} is the amplitude reflectivity of the PRM. In the formulas for the quantum noise eqs. (3.40) and (3.45) one has to replace the input power $P_{\text{in}} \rightarrow G_{\text{PR}} P_{\text{in}}$. Taking into account losses inside the interferometer, the reachable gain is bounded by the power losses A_{ifo} inside the interferometer as [47]

$$G_{\text{PR}} \approx \frac{1}{A_{\text{ifo}}} \quad (3.57)$$

where we assume that most of the loss occurs in the interferometer and not at the PRM.

3.6.2. Signal Recycling

Placing a signal-recycling mirror (SRM) in the output port and tuning the resulting cavity to resonance with the carrier light creates a signal recycling cavity. As shown in fig. 3.5 on the right, the interferometer is again modeled as a single mirror. This cavity acts as an optical low-pass filter for a signal generated inside the cavity (interferometer signals) and resonantly enhances signal sidebands that lie inside the

cavity bandwidth [12, 39]. We can define a frequency dependent signal-recycling gain

$$G_{\text{SR}}(f) = \frac{G_{\text{SR}}}{1 + \left(\frac{f}{f_c}\right)^2} \quad (3.58)$$

with the corner-frequency $f_c = \frac{\omega_c}{2\pi}$ (see eq. (3.32)) and the DC gain

$$G_{\text{SR}} = \frac{1 + r_{\text{SR}}}{1 - r_{\text{SR}}} \quad (3.59)$$

where r_{SR} is the amplitude reflectivity of the SRM.

We can substitute $P_{\text{in}} \rightarrow G_{\text{SR}}(f)G_{\text{PR}}P_{\text{in}}$ in the expression for the quantum noise from eqs. (3.40) and (3.45) to get the combined effect for power- and signal-recycling for the shot noise [9]

$$S_{xx}^{\text{shot}}(\omega) = \frac{\hbar c \lambda}{16\pi r_m^2 G_{\text{SR}} G_{\text{PR}} P_{\text{in}}} \left[1 + \left(\frac{\omega}{\omega_c}\right)^2 \right] \quad (3.60)$$

and the back-action noise

$$S_{xx}^{\text{RPN}}(\omega) = |H(\omega)|^2 \cdot \frac{16\pi \hbar r_m^2 G_{\text{SR}} G_{\text{PR}} P_{\text{in}}}{c \lambda} \frac{1}{1 + \left(\frac{\omega}{\omega_c}\right)^2}. \quad (3.61)$$

4. Experimental Setup

In this chapter, I describe the experimental setup that I have designed and built during this work. Central point is the suspended mirror pendulum serving as the common end mirror in an interferometer with Michelson-Sagnac topology. The interferometer is located in a high vacuum to avoid residual gas damping. In order to reduce seismic excitation, we use a passive isolation system for the optical table and a second passive isolation stage for the interferometer itself. For frequencies around the pendulum mode, we designed an active seismic isolation that is going to be implemented. For the pendulum, we use a cuboid test mass suspended by two wire loops. Here, I calculate the moment of inertia for this shape and estimate the eigenfrequencies for different pendulum modes. I further explain the design considerations for the interferometer which are based on [2]. We use an optical setup with the two laser wavelengths of 1550 nm and 1064 nm for interferometric position readout and detection of the deflection angle as well as for applying a radiation pressure force to the test mass.

4.1. Vacuum System

The vacuum system consists of a cylindrical steel chamber with an inner diameter of 35 cm and a height of 32 cm with two optical window flanges attached on opposite sides. The optical axis through the center of the windows is located 17.8 cm above the table surface. Additionally one high voltage BNC feedthrough for the parametric actuation piezo and a 25-port D-Sub feedthrough for the cryo-compatible mirror positioners are connected. The vacuum side electrical connections are made with Kapton[®] coated wires. A wide range gauge (Edwards WRG-S-DN40CF) that is able to measure the pressure inside the chamber from atmospheric pressure down to 10^{-9} mbar is attached.

A turbopump (Edwards nEXT400D 160W, CF160) connected via a gate valve provides a high vacuum on the order of 10^{-8} mbar that is backed up by a scroll pump providing the necessary pre-vacuum of 10^{-1} mbar. The scroll pump is located in a separate room and shared via a tube system to multiple laboratories to remove disturbances from the experiments. The turbopump is connected to this system

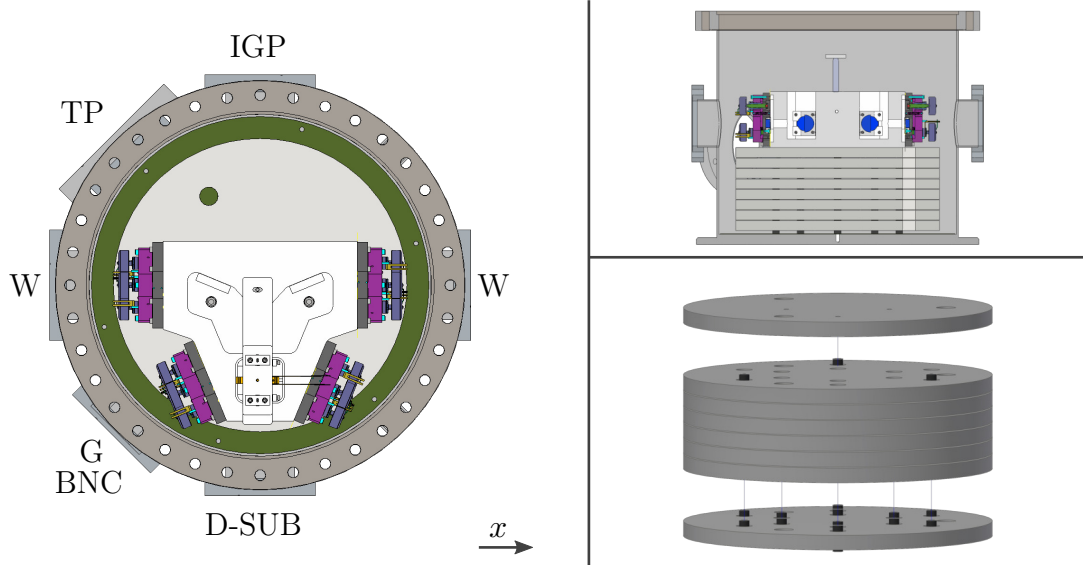


Figure 4.1.: CAD views of the vacuum assembly. **Left:** Top view with the interferometer on top of the seismic isolation stage. The connections to the flanges are indicated: Window (W), Turbopump (TP), ion getter pump (IGP), 25-port D-Sub connector (D-SUB), wide range gauge (G) and the high voltage BNC feedthrough (BNC). **Right top:** Half-cut through the assembly up to the optical axis. The two flanges on the sides are the window flanges. **Right bottom:** Exploded view of the seismic isolation stage with the top plate lifted up and the bottom plate extended down. One can see the 12 FPM dampers for the bottom plate and the three below the top plate due to less weight above.

with a ball valve which is bypassed with a needle valve to prevent a high gas flow during the initial pump down to the pre-vacuum. An additional ion getter pump is connected to the chamber to be able to perform the experiment without a running turbopump. It has not been used so far since no disturbances due to the turbopump have been observed yet. A computer-aided design (CAD) drawing of the vacuum tank with the connection to the flanges is shown in fig. 4.1 on the left. On the right top one can see a half cut through the assembly up to the optical axis.

4.2. Seismic Isolation

Since the experiment works with low mechanical frequencies around 1 Hz, it can be disturbed by seismic excitations. Especially in urban environments where the experiment is located, seismic noise above 1 Hz is present [48]. In this section, I discuss multiple passive seismic isolation systems for different frequency ranges. Since the passive methods do not provide sufficient isolation, I introduce a planned active seismic isolation scheme.

4.2.1. Optical Table

The optical table is located on top of a concrete block with a mass of ≈ 31 t supported by four spring dampers. This provides a passive seismic isolation, since the table is not directly connected to the ground. Additionally, the table has a build-in pneumatic vibration isolation, which is not used at the moment, since it has a resonance in the frequency range of the pendulum. Figure 4.2 shows a measurement of the displacement spectrum with a seismometer (Trillium 120Q/QA from Nanometrics) on top of the concrete block in the three Cartesian coordinate axes as defined in fig. 4.6. The seismometer measures the velocity from which I estimated the PSD using Welch's method [50] as implemented in SciPy [51, 52]. The velocity spectrum is converted into a displacement spectrum by dividing by the square of the angular frequency. One can see a resonance peak around 2 Hz for the x- and y-direction and at around 3 Hz for the z-direction. Since this lies in the frequency range of the pendulum, it is still seismically excited. In order to reduce the seismic excitation further, we are going to implement an active isolation scheme on the concrete block with voice coil actuators that provide a feedback force onto the concrete block. Since voice coil actuators do not have a mechanical connection to the ground, no additional seismic coupling without the active feedback is introduced.

4.2.2. Seismic Isolation Stage

In order to decouple the interferometer from seismic disturbances, it is located on top of a seismic isolation stage inside the vacuum tank that is the only mechanical connection to the outside except from the electrical wiring. The damping stage consists of 8 steel plates that are connected via fluoroelastomer (FPM) dampers that act as springs between the plates. The plates have a diameter of 300 mm and a height of 14.375 mm each. The dampers are cylindrical and have a diameter as well as a compressed height of 10 mm. They are inset into the plates both on top and on the bottom to provide a gap between the plates of 1 mm. Since the total height of the stage is restricted by the optical axis, this allows higher plates and thus more mass which provide a better isolation. The total height of isolation stage is 127.5 mm.

The seismic isolation stage was mainly designed to provide a good isolation in a frequency range around 300 Hz, since the experiment is designed to be quantum noise limited around this frequency range. A finite element method (FEM) simulation in COMSOL Multiphysics® of the transfer function from ground displacement to displacement of the upper plates is shown in fig. 4.3. For the simulation, a frequency dependent loss factor for FPM is used as measured in [53]. For more details on how this is implemented consider [54]. Table 4.1 contains an overview of the used

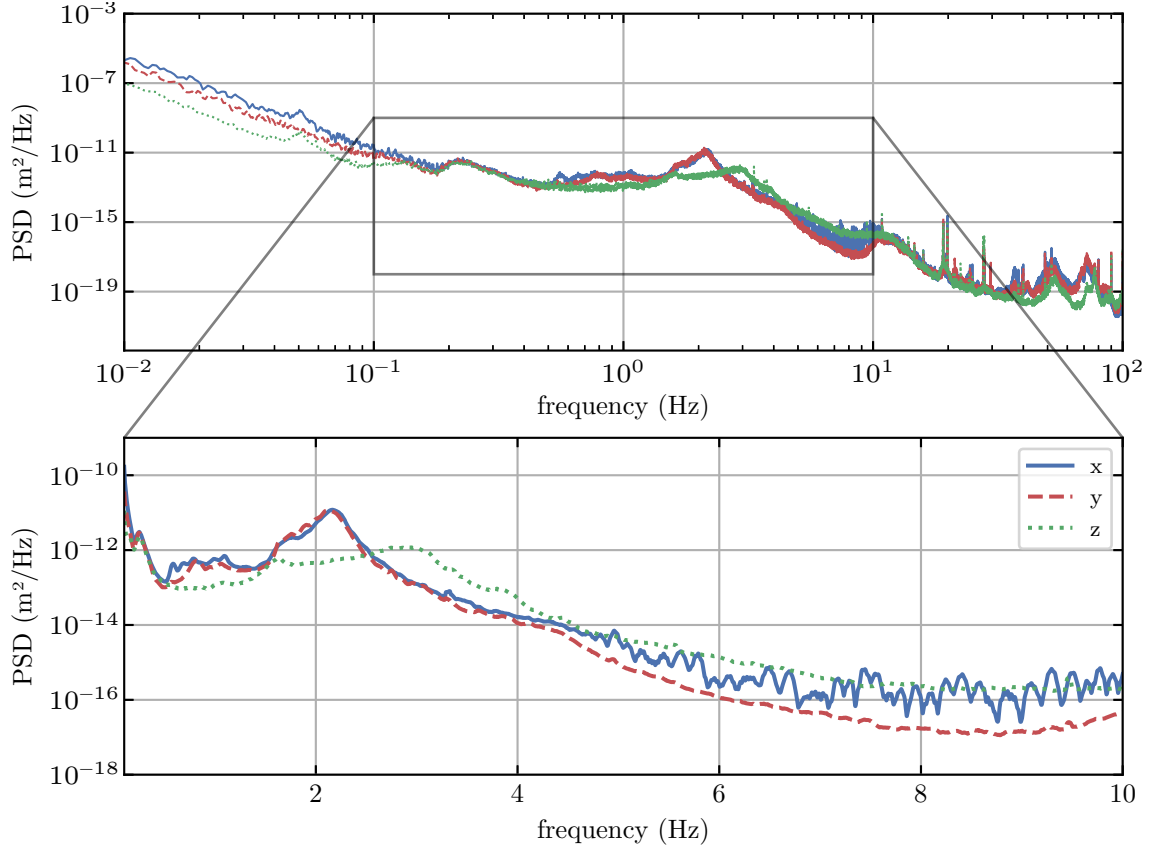


Figure 4.2.: Seismic noise for three directions measured on top of the concrete block of the passive optical table isolation. The measurement axes coincide with the coordinate system defined in fig. 4.6.

Top: Displacement PSD against logarithmic frequency. The spectrum decreases until it reaches a plateau around 1 Hz of $\approx 1 \times 10^{-12} \text{ m}^2 \text{ Hz}^{-1}$ and leads to a resonance peak at around 2 Hz after which it further decreases. The self noise of the seismometer increases above 10 Hz [49], which might be the cause for the additional peak at higher frequencies.

Bottom: Zoom around the resonance peak with linear frequency axis to the region where the seismometer has a flat response.

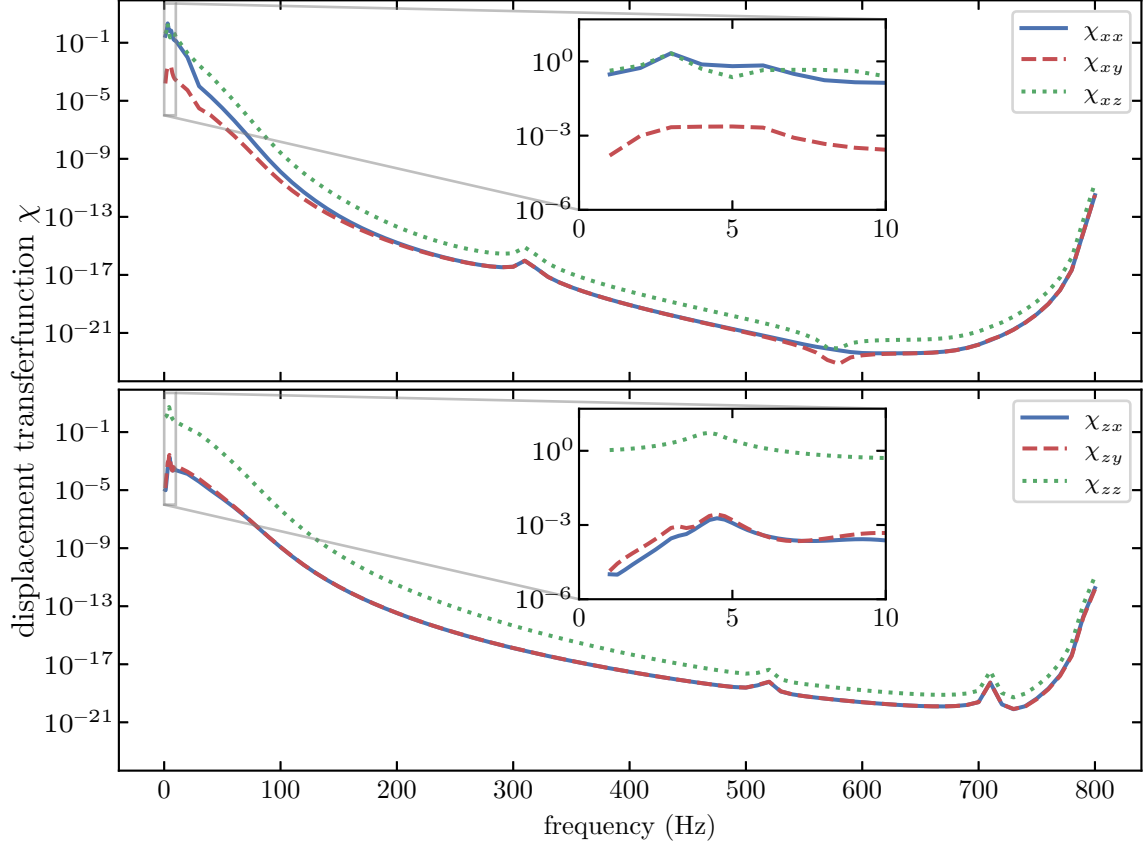


Figure 4.3.: FEM simulation of the displacement transfer functions χ for the seismic isolation stage in COMSOL Multiphysics[®]. In the simulation, a displacement to the ground of $1\mu\text{m}$ is applied and the resulting displacement is averaged over the top plate. The transfer function χ_{ij} denotes a ground displacement Δi causing a top displacement Δj for $i, j \in \{x, y, z\}$. The coordinate system is the same as given in fig. 4.6. A frequency dependent loss factor for FPM is assumed as measured in [53]. The simulation was performed by Alexander Franke.

Top: Transfer function from displacement in x -direction to all three directions x, y, z .

Bottom: Transfer function from displacement in z -direction (up-down) to all three directions x, y, z .

Table 4.1.: Material parameters used in the FEM simulation for the isolation stage.

Material parameter	Symbol	Steel	FPM
Young's modulus	E	200 GPa	6.6 MPa
Density	ρ	$7.9 \times 10^3 \text{ kg m}^{-3}$	$2 \times 10^3 \text{ kg m}^{-3}$
Poisson's ratio	ν	0.29	0.48

material parameters in the simulation. The top of fig. 4.3 shows the simulated transfer function for displacement in x -direction to all three spatial directions. The coordinate system is the same as defined in fig. 4.6, where the x -axis is along the movement of the main pendulum mode. The inset shows a zoom onto the lower frequency part. One can see a small resonance at around 3 Hz for χ_{xx} and χ_{xz} of the otherwise relatively constant transfer function. For higher frequencies, it decreases significantly to around 1×10^{-16} around 300 Hz. Above 700 Hz it rises again due to resonances of the steel plates. The general trend is the same for initial displacement in z -direction, which is shown below. Thus, this passive isolation should provide a good reduction of seismic excitation at higher frequencies. However, around the center frequency of the main pendulum mode at 1.5 Hz, no significant isolation is provided. For that reason, we will implement the active isolation discussed above. A more detailed overview of the design consideration for the isolation stage can be found in the master's thesis of Alexander Franke [54] that I supervised during the course of this work.

Damper Compression

Since the dampers are compressed under a weight load, the uncompressed height h for the different plates has to be determined in order to get the compressed height $h_0 = 10 \text{ mm}$. The strain $\frac{h-h_0}{h}$ is connected via the Young's modulus E to the stress $\sigma = E \frac{h-h_0}{h}$ [55, p. 372] from which the uncompressed height can be calculated

$$h = \frac{h_0}{1 - \frac{\sigma}{E}}. \quad (4.1)$$

The stress per damper is

$$\sigma = \frac{mg}{N\pi r^2} \quad (4.2)$$

where N is the number of dampers, $r = 5 \text{ mm}$ the radius of the damper and m is the mass of the weight load above. The uncompressed heights with three dampers per plate for the lower plates were much larger than the diameter resulting in a thin long cylinder. This made the isolation stage very unstable and a new approach

Table 4.2.: Number of FPM dampers for the seismic isolation stage. The plates are numbered from top to bottom. The Young's modulus of FPM is $E_{\text{FPM}} = 6.6 \text{ MPa}$. The second table shows the masses of the different loads.

plate	# of dampers	mass (kg)	$\frac{\text{stress}}{\text{damper}}$ (MPa)	height (mm)
1	3	14.92	0.62	11.0
2	3	22.79	0.95	11.7
3	6	30.67	0.64	11.1
4	6	38.55	0.80	11.4
5	6	46.42	0.97	11.7
6	12	54.30	0.56	10.9
7	12	62.17	0.65	11.1
8	12	70.05	0.73	11.2

mass (kg)	
description	
top plate	8.00
normal plate	7.88
interferometer spacer	4.07
mirror positioner	0.71

with more dampers such that the stress per damper stays roughly the same is used. Table 4.2 shows the resulting heights for each plate, where the plates are counted top to bottom. The Young's modulus of the FPM was measured by Henry Frädrieh for his master's thesis as $E_{\text{FPM}} = 6.6 \text{ MPa}$.

An exploded CAD view of the final isolation stage is shown in fig. 4.1 on the bottom right. One can see the different number of dampers for the top and bottom plate. The three bigger holes go through each plate and are used for alignment and for measurements of the total height. A column of these holes is visible in the half cut through the vacuum assembly in fig. 4.1 in the top right.

The above calculations used a stationary model where the strain results instantaneously from the applied stress. However, real physical system often experience creep and the stationary state is only reached asymptotically. Such behavior can be modeled with the standard linear solid (SLS) in Kelvin-Voigt form where a single spring is put in series with a so called Maxwell element, a spring parallel to a viscous dashpot that introduces an exponential time dependence [56, 57]. Figure 4.4 shows this model (right) and the measured height of the isolation over time after the interferometer was put on top (left). The height decreased instantaneously and

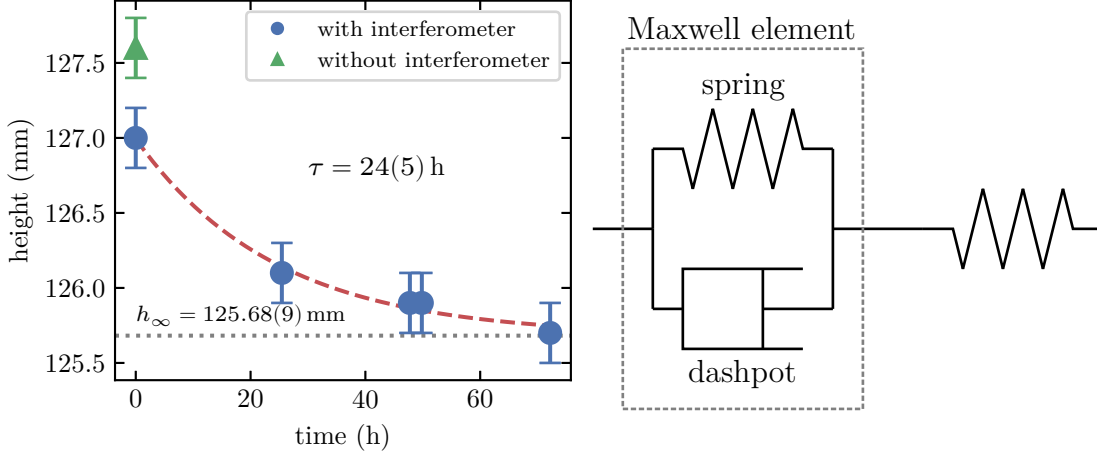


Figure 4.4.: Left: Measured height of the seismic isolation stage before and after the interferometer was put on top. The time dependent creep was fitted using eq. (4.3). **Right:** Schematic drawing of the Kelvin-Voigt SLS with a single spring in series with a Maxwell element that consists of a spring in parallel with a viscous dashpot.

then experienced a time dependent creep that was fit using the function

$$h(t) = h_{\infty} + (h_0 - h_{\infty}) \exp\left(-\frac{t}{\tau}\right) \quad (4.3)$$

with the stationary value $h_{\infty} = 125.68(9)$ mm and the relaxation time $\tau = 24(5)$ h. It takes multiple days for the isolation stage to settle to the final position which is 2 mm lower than the designed value of 127.5 mm, which can be compensated by the alignment of the incoming beam.

4.3. Pendulum

The following section explains the ideas and concepts to set up a high Q pendulum with a novel cuboid test mass design and a suspension system that allows for a parametric drive of the pendulum. The moments of inertia for the test mass and the expected eigenfrequencies for multiple modes of the system are calculated and the installation process of the pendulum is described.

4.3.1. Suspension

The pendulum is suspended by two loops of tungsten wire with radius $r_{\text{wire}} = 20 \mu\text{m}$ and density $\rho_{\text{wire}} = 19.3 \text{ g cm}^{-3}$ [58]. The wires are clamped between two metal rods

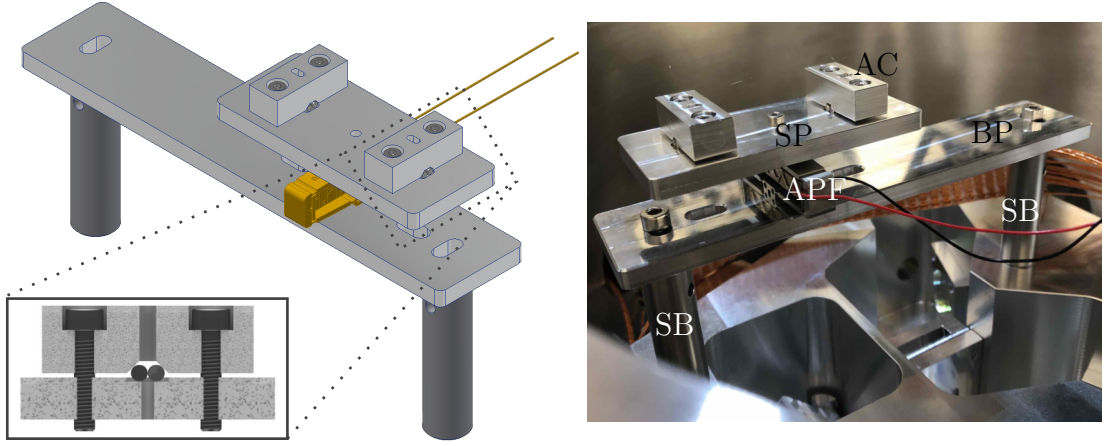


Figure 4.5.: Suspension system. **Left:** CAD drawing with a cut through the suspension clamping. The suspension wire is clamped between the two metal rods in the center. **Right:** Photo of the installed suspension system on top of the interferometer spacer with the two support beams (SB). The amplified piezo actuator (APF) is attached to the base plate (BP) at the bottom and to the suspension plate (SB) at the top. The two angled clamps (AC) are screwed to the suspension plate pressing the metal rods against the suspension wire.

that are pushed together with an angled clamp that is screwed to the suspension plate. This creates ideally a single point of contact and thus reduces losses due to friction in the suspension system. A schematic view and a photo of the suspension can be seen in fig. 4.5. The suspension plate is screwed to an amplified piezoelectric actuator (Thorlabs APF503) that shrinks in height under positive voltage (up to 150 V) with a displacement range of 310 μm . The piezo actuator is attached to a base plate at the bottom that connects to the two support beams.

4.3.2. Test Mass

The test mass for the pendulum is a cuboid made from Suprasil[®]3001 (Heraeus) with width $b = 25 \text{ mm}$ and a square surface with side length $a = 29 \text{ mm}$. The square is rotated by 45° when suspended such that the tips are facing sideways. This creates a sharp corner as a bending point for the suspension wire which is thought to reduce friction losses due to the wire sliding on the test mass. A schematic overview of the suspended test mass from multiple directions is shown in fig. 4.6. The sensing laser is traveling in x-direction and is reflected off this square surface which is coated with a highly reflective dielectric coating with a power transmissivity $T = 150 \text{ ppm}$ for the main laser wavelength $\lambda = 1550 \text{ nm}$. For the secondary laser wavelength $\lambda = 1064 \text{ nm}$ the transmissivity is $T = 1 \%$. The two square surfaces have a radius of curvature (RoC) of 690 m to form a stable resonator cavity with length $L_{\text{cav}} = b$.

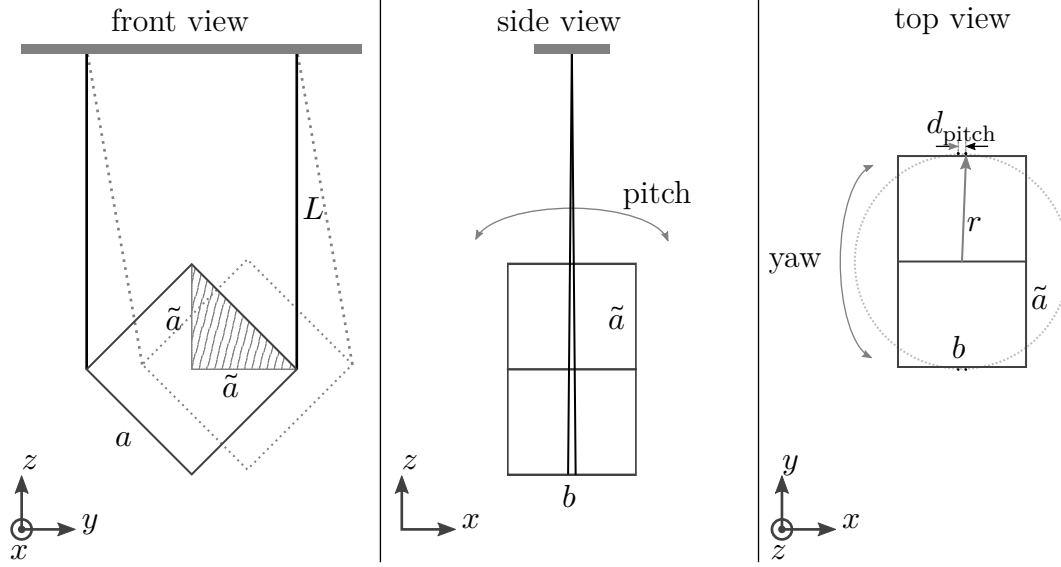


Figure 4.6.: Schematic view of the *MassQ* pendulum from three directions. The test mass is suspended by two wire loops converging to a single point (see **side view**). The movement for the pitch and yaw modes are indicated in the side and top view, respectively. The sensing laser is traveling in x -direction and is reflected of the surface in the **front view**. The striped area indicates a quarter of the volume that is used for the integration to calculate the moments of inertia. The dotted lines indicate the movement of the perpendicular mode.

The resulting cavity waist radius is $w_0 = 1.002 \text{ mm}$ which leads to a low diverging beam inside the interferometer. An overview of the test mass parameters is given in table 4.3. The actual mass of the test mass was weighed with a precision scale to $m = 47.657 \text{ g}$.

The two suspension wire loops are spaced a small distance apart on the bottom of the test mass and converge to a single clamping point as can be seen in fig. 4.6 in the side view.

Moments of Inertia

In order to calculate the pendulum's moments of inertia I_S relative to axes through the suspension point, it is sufficient to compute the moments of inertia I_{CM} relative to axes through the CM and use Steiner's parallel axis theorem to shift the axes by the pendulum length L yielding $I_S = I_{\text{CM}} + mL^2$. The moment of inertia is generally given by integrating over all mass elements dm [55, pp. 300-301]

$$I = \int_V r_{\perp}^2 dm = \int_V r_{\perp}^2 \rho(\vec{r}) dV \quad (4.4)$$

Table 4.3.: *MassQ* test mass parameters.

m	47.657 g
a	29 mm
b	25 mm
RoC	690 m
w_0	1.002 mm
T(1550 nm)	150 ppm
T(1064 nm)	1 %
material	Suprasil [®] 3001

where r_\perp is the perpendicular distance to the axis of rotation and $\rho(\vec{r})$ the density inside the volume V .

For a body with constant density, this can be written as

$$I = \rho \int_V r_\perp^2 dV = \frac{m}{V} \int_V r_\perp^2 dV. \quad (4.5)$$

In the case of the *MassQ* pendulum in fig. 4.6, the moments of inertia for the three main axes through the CM are given by

$$I_i = 4 \frac{m}{a^2 b} \int_0^b dx \int_0^{\tilde{a}} dy \int_0^{\tilde{a}-y} r_{\perp,i}^2 dz, \quad i \in \{x, y, z\} \quad (4.6)$$

where $r_{\perp,x}^2 = y^2 + z^2$ and correspondingly for y and z . The integration is executed over a quarter of the volume due to symmetry (striped area in fig. 4.6) and compensated by the factor 4. The integration bounds for the striped region are given by $\tilde{a} = \frac{a}{\sqrt{2}}$ and the volume of the test mass is $V = a^2 b$. Evaluating these integrals (using *SymPy* [59]) yields

$$I_x = \frac{ma^2}{6} \quad (4.7)$$

$$I_y = I_z = \frac{m(a^2 + 4b^2)}{12}. \quad (4.8)$$

Test Mass Holder

In order to make characterization measurements on the test mass and to help with the installation of the pendulum into the interferometer, a holder for the mass was

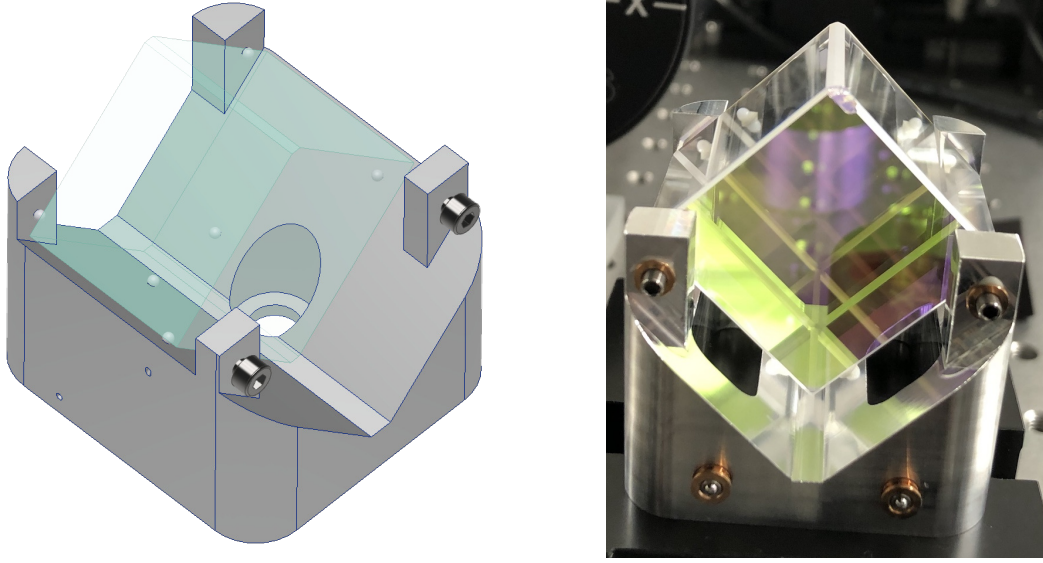


Figure 4.7.: Test mass holder. **Left:** CAD drawing of the holder with the test mass sitting on top of the PTFE spheres that are inset into the holder. **Right:** Photo of the coated test mass inside the holder viewed in the direction of the laser.

designed. The test mass rests on the two lower angled side faces on four polytetrafluoroethylene (PTFE)(also known as *Teflon*[®]) spheres and is restricted in motion in the x -direction by two fixed PTFE spheres and two adjustable screws with PTFE tips. This allows adjustment of the movement range for the pendulum. A CAD drawing of the holder as well as a photo of the resting test mass in the holder is shown in fig. 4.7.

4.3.3. Pendulum Eigenfrequencies

In this section I present the eigenfrequencies for multiple mechanical modes of the pendulum. Each mode is modeled independently as a single degree of freedom harmonic oscillator. An overview of the different modes is given in fig. 4.8.

Main Mode

With eqs. (2.35) and (4.8) one can calculate the eigenfrequency for the main pendulum mode rotating around the y -axis (test mass movement in x -direction)

$$\omega_{0,\text{main}} = \omega_{0,y} = \sqrt{\frac{12Lg}{12L^2 + a^2 + 4b^2}}. \quad (4.9)$$

It depends on the moment of inertia of the suspended mass.

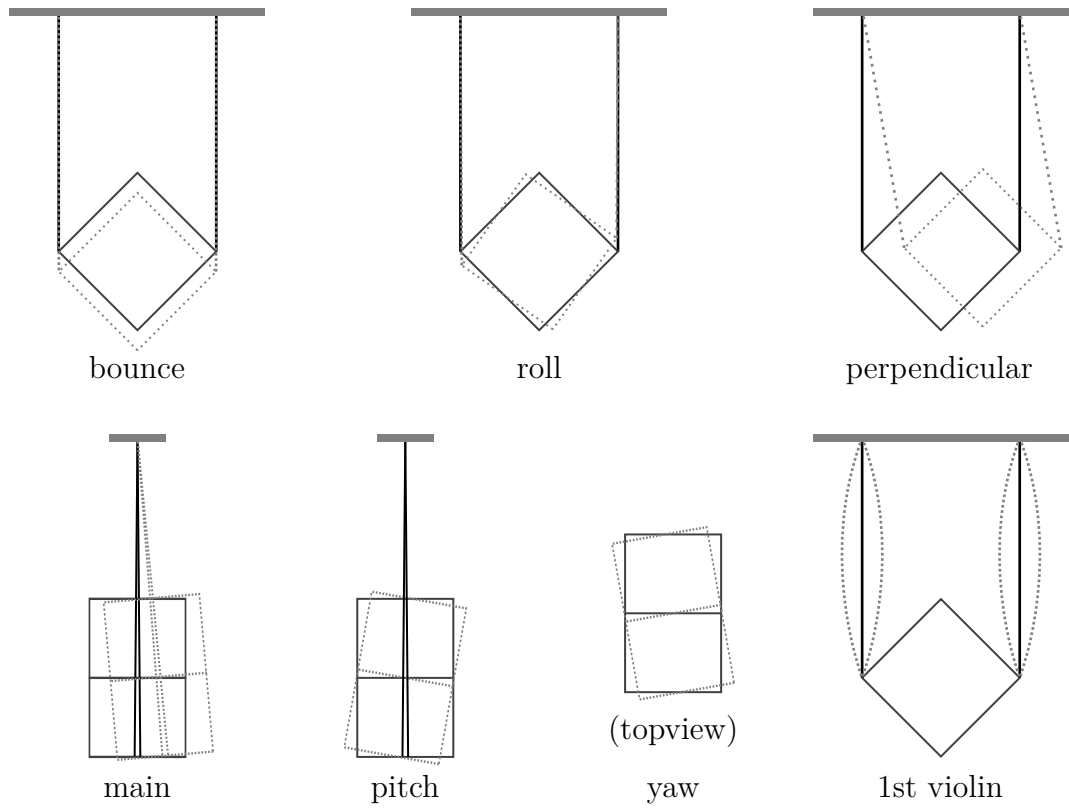


Figure 4.8.: Mechanical modes of the suspended pendulum. The dashed lines indicate the movement of the test mass and the suspension wires.

Perpendicular Mode

The perpendicular pendulum mode arises due to the two separated suspension attachment points along the y -direction. This keeps every point of the suspended mass moving on an arc with radius L as shown with the dotted lines in fig. 4.6. Thus the frequency for this mode is independent of the moment of inertia and is the same as for the mathematical pendulum eq. (2.36).

Pitch and Roll Mode

The pitch and roll mode store energy in the elasticity of the suspension wires. These exert a restoring torque on the suspended mass due to the off-center attachment points. The following derivation of the eigenfrequency is based on work by my colleague Daniel Hartwig.

The spring constant k_{wire} is determined by the Young's modulus of the wire material E and the area of the wire's cross section A by Hooke's law [55]

$$k_{\text{wire}} = \frac{\Delta F}{\Delta L} = \frac{EA}{L} \frac{\Delta L}{L} = \frac{EA}{L} \quad (4.10)$$

where ΔF is the force and ΔL the distance the wire is displaced from the equilibrium length L . The torque from N wires that are placed a distance $\frac{d}{2}$ from the center of mass is then

$$\tau = N \frac{d}{2} \Delta F = N \frac{d}{2} k \Delta L = \frac{N}{4} k d^2 \varphi. \quad (4.11)$$

Here I used the small angle approximation to express the length change in terms of the rotation angle φ as $\Delta L = \frac{d}{2} \varphi$.

From the EOM

$$I \ddot{\varphi} + \frac{N}{4} k d^2 \varphi = 0 \quad (4.12)$$

we can extract the eigenfrequency for the elastic pendulum modes as

$$\omega_{0,\text{elastic}} = \sqrt{\frac{N k d^2}{4 I}} = d \sqrt{\frac{N E A}{4 I L}}. \quad (4.13)$$

Yaw Mode

As an approximation for the yaw mode frequency, we assume rigid suspension wires that remain at a constant length L . When the test mass rotates around the z -axis

by an angle ϕ , the suspension attachment points move on a circle with radius r as indicated by the dotted line in the top view of fig. 4.6. In our case, that is

$$r = \sqrt{\tilde{a}^2 + \left(\frac{d_{\text{pitch}}}{2}\right)^2}. \quad (4.14)$$

The pendulum mass is lifted and energy is stored in the gravitational field. Using small angle approximations, we can estimate the resulting mode frequency. Then the suspension point is displaced from its equilibrium position by $\Delta x \approx r\phi$. This is essentially a gravity pendulum as in fig. 2.4. The wire compensates the radial component of the gravitational force, giving a restoring force

$$F_\tau \approx \frac{m}{N}g\theta \approx \frac{m}{N}g\frac{\Delta x}{L} \quad (4.15)$$

along Δx . This force acts as a torque τ to the yaw rotation from each of the N suspension wires

$$\tau = N\frac{mgr^2}{NL}\phi = \frac{mgr^2}{L}\phi. \quad (4.16)$$

Using this torque in the EOM

$$I_z\ddot{\phi} + \frac{mgr^2}{L}\phi = 0, \quad (4.17)$$

one can determine the eigenfrequency

$$\omega_{0,\text{yaw}} = \sqrt{\frac{mgr^2}{I_z L}}. \quad (4.18)$$

Similar approximations have been employed for a two wire suspension in [60]. However, since this assumes rigid suspension wires, the real mode frequency is expected to be higher due to an additional force from the elasticity of the wire.

Bounce Mode

The bounce mode frequency is that of an elastic pendulum where each suspension wire takes a load of $\frac{m}{N}$. Using the spring constant from eq. (4.10), the eigenfrequency for the bounce mode is then

$$\omega_{0,\text{bounce}} = \sqrt{\frac{EAN}{mL}}. \quad (4.19)$$

Violin Modes

The violin modes of the suspension wire can be approximated by the natural frequencies of an ideal string and are given by [61]

$$\omega_n = \frac{n\pi}{L} \sqrt{\frac{mg}{N\mu}} \quad (4.20)$$

where $\mu = \pi r_{\text{wire}}^2 \rho_{\text{wire}}$ is the wire's linear mass density. Higher order violin frequencies are integer multiples of the fundamental mode frequency.

An overview of the different pendulum eigenfrequencies is shown in table 4.4. The designed pendulum length was $L = 12.01$ cm, however, this is most probably not the real pendulum length since it is not possible to determine the length precisely when suspending the pendulum in the experiment. Another length for the calculation was chosen such that the main pendulum mode resembles the measured eigenfrequency better for comparison. The Young's modulus for these calculations was fitted such that the frequencies for the roll and bounce mode were close to observed frequencies in the experiment (compare section 5.2). This resulted in $E_{\text{tungsten}} = 355$ GPa which is in good agreement with values in the literature [62, 58]. Since the wire distance for the pitch mode d_{pitch} is not exactly known, I fitted a value to the observed frequency of the pitch mode. This resulted in $d_{\text{pitch}} = 7.5$ mm, which is a reasonable value for the installed pendulum. For the wire's density, the value $19.3 \times 10^3 \text{ kg m}^{-3}$ provided by the manufacturer was used [58].

4.3.4. Pendulum Installation Procedure

The installation process of the pendulum into the interferometer is a challenging task due to the small wire diameter and the tendency of the wires to curl. At the beginning, only the two support beams should be installed on the interferometer spacer. The installation procedure is as follows:

1. First, the holder for the test mass is placed inside the cutout in the interferometer spacer and secured in the correct position by screwing the attached screws against the spacer wall.
2. The next step is to place the two wire loops into the cutout. For this, the tungsten wire should be cut to a length of approximately 0.5 m and hung down from one end between two fingers to check for entanglement and remove any curls.
3. Place both wires such that they run in parallel straight over the cutout.

Table 4.4.: Calculated eigenfrequencies for the different pendulum modes. $L = 12.010$ cm is the designed pendulum length and $L = 11.824$ cm was fitted such that the main pendulum mode (pendulum y) corresponds to the measured value. I assumed a Young's modulus for tungsten of $E_{\text{tungsten}} = 355$ GPa.

mode	ω_0	$f_0(L = 12.010 \text{ cm})(\text{Hz})$	$f_0(L = 11.824 \text{ cm})(\text{Hz})$
math./perpendicular	$\sqrt{\frac{g}{L}}$	1.4382	1.4494
pendulum y / main	$2\sqrt{3}\sqrt{\frac{Lg}{12L^2+a^2+4b^2}}$	1.4245	1.4352
roll	$\frac{\sqrt{3}a\sqrt{\frac{AEN}{La^2m}}}{2}$	38.4800	38.7815
pitch ($d = 7.5$ mm)	$\sqrt{3}d\sqrt{\frac{AEN}{Lm(a^2+4b^2)}}$	9.9859	10.0642
yaw ($d = 7.5$ mm)	$\sqrt{3}\sqrt{\frac{g(2a^2+d^2)}{L(a^2+4b^2)}}$	1.7967	1.8108
bounce	$\sqrt{\frac{AEN}{Lm}}$	44.4329	44.7810
1st violin	$\pi\sqrt{\frac{gm}{L^2N\mu_{\text{wire}}}}$	578.6692	587.7721

4. Place the test mass centrally onto the wires and lower it down onto the holder pulling the wires down into the cutout. This holds the wires under tension and prevents curling.
5. Screw the first plate to the support beams and attach the piezo actuator and the suspension plate.
6. Fiddle the two wires through the holes in the two plates and through the angled clamp.
7. Place the metal rods from both sides against the wire into the grove and screw down the clamp but do not fasten the screws yet. The wire is hold in place by the weight of the clamp.
8. Repeat the steps for the other ends of the wire loops.
9. Apply 150 V to the piezo actuator to lower the suspension.
10. Pull on the wires to tension them slightly without lifting the test mass and tighten the clamp screws carefully.
11. Reduce the piezo voltage to 75 V to pull out the pendulum to the final resting position.

An improvement that would help drastically with step 6 is to add small slits to the holes in the plates. With that one can place the wires into the holes from the side.

4.4. Interferometer

In this section, I describe the design considerations for the interferometer. A central monolithic interferometer spacer serves as attachment point for the optics and the test mass suspension. I calculate the curvature for the test mass as well as the recycling mirrors and simulate the cavity parameters for three different test mass materials. I further describe the control of the cryo-compatible electric mirror positioners used for the steering mirrors and the recycling mirrors.

4.4.1. Interferometer Design

The interferometer design uses a Michelson-Sagnac topology with a beamsplitter and two steering mirrors that fold the interferometer arms by 45° into a loop where the two counter-propagating beams take the same optical path. Placing a highly reflective mirror into the path creates a Michelson interferometer where the mirror is the common end mirror for both arms. This reduces the displacement noise of the mirror due to laser intensity noise depending in the splitting ratio of the beamsplitter. For our interferometer, the input and output paths are also deflected each by 45° from two fixed mirrors such that they lie on the same optical axis as the opposing input and output windows of the vacuum tank. Power- and signal-recycling are possible using an additional steerable mirror in the input and output of the interferometer, respectively. These four mirrors are controlled electronically. One idea to help with the alignment to the test mass was to design it itself as a cavity. With this, the cavity axis can be used as a reference to match both interferometer arms to. This makes sure that the opposing laser beams hit the test mass on the same axis, reducing an additional torque to the pendulum from off-center radiation pressure forces. Furthermore, when the laser frequency is tuned off-resonant to the test mass cavity, the optical power inside is suppressed below the transmissivity of the mirror around the anti-resonance which reduces the absorption and thus heating.

Monolithic Spacer

With later cryogenic use in mind, a central monolithic interferometer spacer serves as the attachment point for all optics, to provide mechanical stability and good heat transport. The spacer was milled from a single block of aluminum. A CAD drawing of the spacer with the spatial path lengths is shown in fig. 4.9. It provides cutouts for free movement of the electric mirror positioners that are screwed on. The fixed mirrors are pressed directly onto the spacer for a good thermal contact. The position

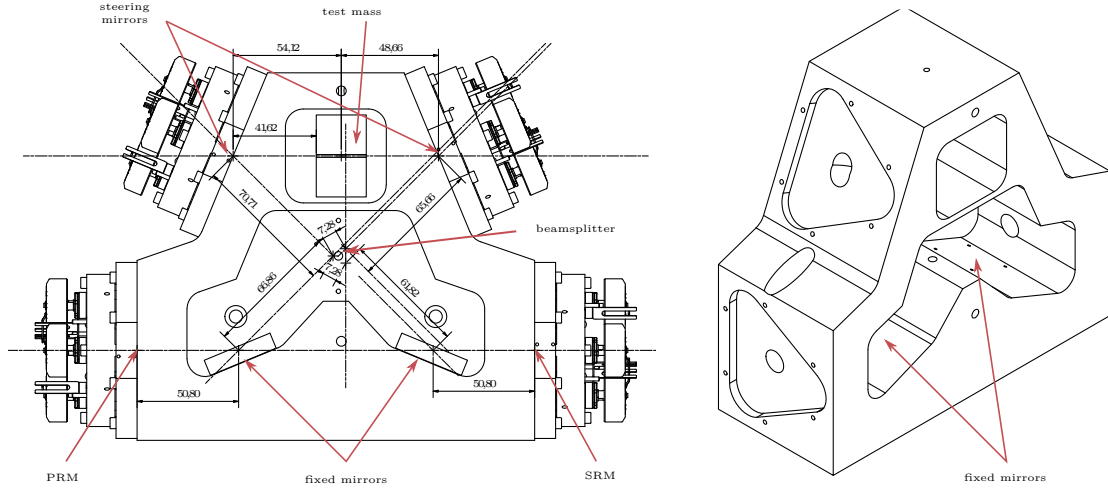


Figure 4.9.: CAD drawing of the interferometer spacer with attached mirror positioners and test mass placed inside the cutout. The spatial path lengths for the laser beams in the interferometer are indicated.

Right: Spacer without attachments. Here one can see the cutouts for the electric mirror positioners as well as the flat wall to place the fixed mirrors against.

of the pendulum is placed slightly off center to compensate the optical path length difference by transmission through the beamsplitter. Holes for the laser beams are drilled into the spacer. It has a total mass of around 4 kg.

4.4.2. Optics

I designed the interferometer optics for a nearly collimated beam with low divergence inside the interferometer with a large beam radius of 1 mm on the test mass surface to reduce coating thermal noise. We considered three materials for the test mass cavity, Suprasil[®]3001, silicon and sapphire, requiring various curvatures for the optics due to different indices of refraction. Silicon and sapphire are expected to have a lower thermal noise contribution at cryogenic temperatures [63]. However, for the room temperature experiment, we use Suprasil[®]3001 for the test mass material since it has better optical properties at room temperature compared to silicon and sapphire.

Mirror Curvature

First, I determined the surface curvature for the test mass cavity for the main laser wavelength of 1550 nm. The cavity length was set to 25 mm by the thickness of

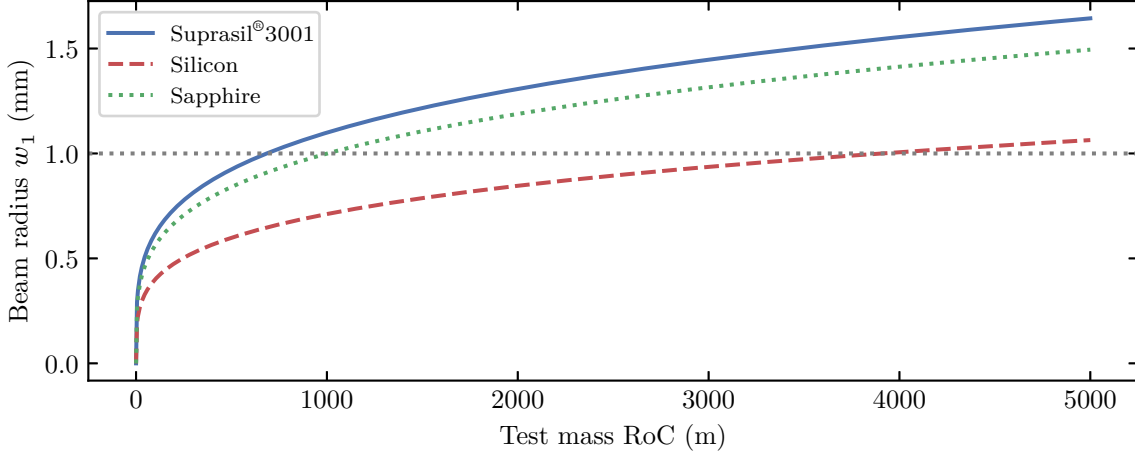


Figure 4.10.: Beam radius w_1 on the test mass surface depending on the RoC for different materials and a wavelength of 1550 nm. The gray dotted line indicates the target size of 1 mm.

an available piece of sapphire. For a symmetric test mass, one can calculate the beam radius on the surface w_{TM} using eq. (3.34) with $R_1 = R_2 = \text{RoC}_{\text{TM}}$. This is shown in fig. 4.10 for the three considered materials. The gray dashed line indicates the desired beam radius of 1 mm. The refractive index n as well as the calculated RoC_{TM} for the materials are summarized in table 4.5. For silicon, the refractive index at 100 K is used while for Suprasil®3001 and sapphire, the refractive index at room temperature is considered. Since the test mass is also one mirror for the recycling cavities, for good mode matching the beam size on this mirror has to be the same

$$w_1(R_1 = -\text{RoC}_{\text{TM}}, R_2 = \text{RoC}_{\text{PRM}}, l = l_{\text{PR}}) = w_1(R_1 = \text{RoC}_{\text{TM}}, R_2 = \text{RoC}_{\text{TM}}, l = l_{\text{TM}}). \quad (4.21)$$

Solving for RoC_{PRM} yields the appropriate curvature for the recycling mirror. The power recycling cavity length is fixed due to space constraints of the mirror positioner and the vacuum tank and was set to $l_{\text{PR}} = 23$ cm. The resulting curvature for the recycling mirrors is also shown in table 4.5 together with the beam radius w_{PRM} on the mirror. Since the signal recycling cavity length is with $l_{\text{SR}} = 23.5$ cm slightly longer, the corresponding radii of curvature RoC_{SRM} are decreased slightly. However, this difference lies within the manufacturing error and should not be problematic due to the small beam divergence. Thus, we ordered mirrors with a $\text{RoC} = 17.75$ m to be used for power and signal recycling.

Cavity Parameters

I simulated the interferometer cavities with the software *Finesse 2* [67] and extracted the cavity parameters for the two laser wavelengths. Table 4.6 shows the

Table 4.5.: RoC and beam radius w for the curved surfaces of the test mass and recycling mirrors. Three materials with different refractive indices n are considered. For Suprasil[®]3001, the index for 1550 nm is calculated using the Sellmeier parameters provided by the manufacturer [64].

Parameter	Suprasil [®] 3001	Silicon	Sapphire
$n(\lambda = 1550 \text{ nm})$	1.44342 [64]	3.4467 @ 100 K [65, 66]	1.7462 [63, 66]
RoC_{TM}	690 m	3400 m	1000 m
w_{TM}	1 mm	1 mm	1 mm
RoC_{PRM}	17.78 m	17.99 m	17.75 m
RoC_{SRM}	17.43 m	17.63 m	17.40 m
$w_{\text{PRM}} \approx w_{\text{SRM}}$	1.008 mm	1.006 mm	1.006 mm

Table 4.6.: Parameters for the three interferometer cavities for both laser wavelengths. Since the recycling mirrors are almost transparent for 1064 nm, here only the test mass cavity parameters are shown.

Cavity	Parameter	1550 nm	1064 nm
	R_{TM}	$> 99.985 \%$	99 %
	R_{RM}	$< 99.7 \%$	$< 0.3 \%$
	n_{TM}	1.444	1.450
Power recycling	Finesse	1992	-
	FSR (MHz)	652	-
	Linewidth (kHz)	327	-
	Optical Roundtrip Length (cm)	46	-
Test mass	Finesse	20942	313
	FSR (MHz)	4152	4136
	Linewidth (kHz)	198	13232
	Optical Roundtrip Length (cm)	7	7
Signal recycling	Finesse	1992	-
	FSR (MHz)	638	-
	Linewidth (kHz)	320	-
	Optical Roundtrip Length (cm)	47	-

power reflectivities R_{TM} and R_{RM} for the test mass and the recycling mirrors, respectively, for both wavelengths. The refractive index for the Suprasil[®]3001 test mass is calculated using the Sellmeier equation [68] with the parameters provided by the manufacturer [64].

For 1550 nm, the test mass has a high reflectivity $R_{\text{TM}} = 99.985\%$ and thus a finesse of $\approx 2.1 \times 10^4$, providing a good intracavity power suppression for off-resonant light. The reflectivity for the recycling mirror $R_{\text{RM}} = 99.7\%$ yields a recycling gain of ≈ 1330 (eq. (3.56)). For an input laser power of ≈ 2 W, this yields a power above 1 kW on each test mass surface. The planned measurement range of up to 800 Hz lies well within the signal recycling cavity linewidth of 320 kHz. With this configuration the free-mass SQL (eq. (3.51)) for a mass $m = 100$ g would be reached at around 300 Hz. For $m = 50$ g, the frequency increases to around 440 Hz.

The recycling mirrors are nearly transparent for the 1064 nm light, which enables radiation pressure interactions with the test mass without the need for a cavity resonance.

Beamsplitter

The beamsplitter inside the interferometer is optimized for 1550 nm light in s-polarization with an angle of incidence (AOI) of 45° . The backside is coated with a high performance anti-reflection (AR) coating with a power reflection < 25 ppm (coating 17021R-19045R). The coating was measured by Pascal Geweke as part of his master's thesis [69].

The beamsplitter is mostly transparent for s-polarized 1064 nm light with a power transmission around 93 %. Thus, most of this light hits the test mass on one side. This asymmetry is needed to apply an effective force due to radiation pressure. Also most of the light is reflected back into the interferometer input port, where it can be used for the detection of the deflection angle (see section 4.7.2).

Since light is transmitted through the beamsplitter substrate, a good thermal contact to the spacer is needed to reduce heating from absorption, especially when using power recycling. For this, the beamsplitter's backside is pressed with leaf springs against a holder, that provides a hole for the transmitted beam to pass through. The holder is then screwed to the spacer. For a better thermal contact, one can use additional gold foil at the contact areas.

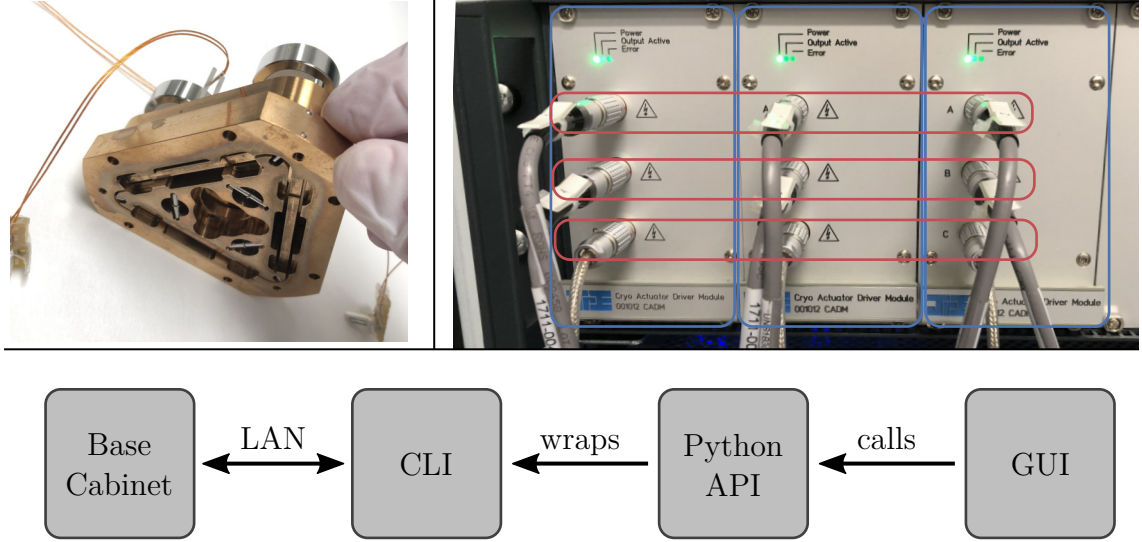


Figure 4.11.: Mirror positioner and control.

Left: Photo of the cryo compatible mirror positioner showing the monolithic spring structure. On the backside, one can see parts of two of the three piezoknobs.

Right: Base cabinet for the mirror positioners. The blue boxes indicate the three control units, of which each one can drive a single piezoknob at a time. This is why the piezoknobs for each positioner are split across the control units as indicated by the red boxes, to be able to drive all three knobs at the same time.

Bottom: Control diagram for the piezoknobs. The self written Python API is a wrapper for the manufacturer provided command-line interface (CLI) that send commands to the base cabinet via LAN.

4.4.3. Mirror Positioners

In order to be able to align the two steering mirrors as well as signal and power recycling mirrors inside the vacuum, we use electric mirror positioners with three degrees of freedom, which are attached to the monolithic interferometer spacer. These positioners were custom made by JPE [70] and are vacuum and cryo compatible. They consist of a triangular monolithic center piece, which is machined such that it acts as a spring. At the corners, three so called piezoknobs push against the monolithic spring to adjust the mirror angle in three directions. By moving the piezoknobs equally, it is possible to move the mirror linearly along the central axis. A photo of these positioners is shown in fig. 4.11. The piezoknobs use a spindle and nut inertia drive, which enables a step motion on nanometer scale which is driven by an AC voltage [71]. The AC amplitude and frequency determine the step size and frequency with a maximum of $150 V_{pp}$ and 600 Hz [72].

Positioner Control

The piezoknobs are controlled via a base cabinet which can hold up to three individual control units. Each of those units can connect to three piezoknobs. Since a control unit can only drive one piezoknob at a time, we connect the three knobs for single mirror positioner to three individual control units. This enables us to move a single mirror with three knobs at the same time. A photo of the base cabinet is shown in fig. 4.11 on the right side. The cable connections for a single mirror positioner are marked. Below, the control scheme is shown. The base cabinet is connected via LAN to the local laboratory network. A manufacturer provided CLI enables the control of individual piezoknobs. For consistent control and to be able to control a whole positioner, I programmed a Python [73] based object-oriented application programming interface (API) that wraps around the CLI. An additional graphical user interface (GUI) based on a Jupyter Notebook [74] enables the use of a persistent configuration with named positioners for easier and more consistent control. More details can be found in appendix D.

4.5. Optical Setup

In the optical setup, we use two wavelengths that are overlapped in front of the vacuum tank to co-propagate inside the interferometer. A simplified schematic view of the optical table is shown in fig. 4.12. Since the windows of the vacuum tank are higher than the beam height on the table, an additional breadboard with a height of 18.9 cm is used to raise part of the table. This makes it possible to place alignment optics with a beam height of 7.5 cm on the input side of the interferometer. We use s-polarized light to enter the vacuum tank since the optics inside the interferometer are optimized for this polarization. By using a flip mirror directly in front of the input view port, the test mass can be characterized outside of the vacuum tank with both wavelengths at the correct waist position. The two laser wavelengths are overlapped directly in front of the vacuum tank only followed by a pair of alignment mirrors, that are highly reflective for both wavelengths.

4.5.1. 1550 nm Setup

The 1550 nm light is shown in red color in fig. 4.12. In order to prevent back reflection into the laser, a Faraday isolator is used behind the fiber laser's collimator after which a polarizing beamsplitter (PBS) with a half-waveplate in front is used to adjust the optical power. Since the spatial mode from the fiber collimator is distorted, it is send through with a mode-cleaner ring cavity. In order to keep the cavity on resonance,

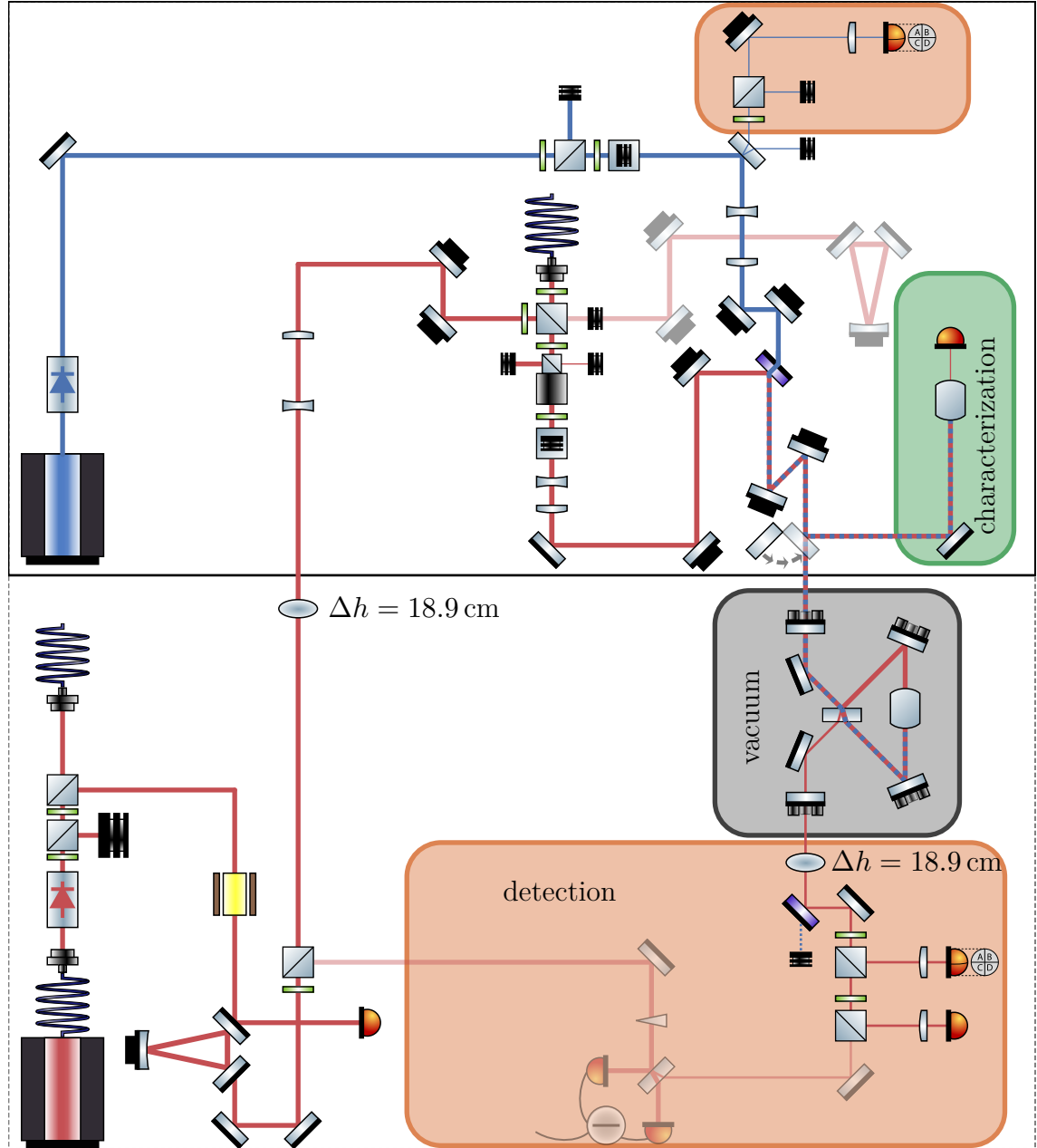


Figure 4.12.: Schematic overview of the optical setup. The two wavelengths of 1550 nm and 1064 nm are displayed with red and blue color, respectively. The gray dashed line indicates the optical table and the solid black line shows the area, where the surface is raised with an additional breadboard to adjust the beam height to the window height of the vacuum chamber. The green box highlights the characterization setup for the test mass cavity for which the light can be picked up with a flip mirror in front of the vacuum chamber, which is indicated with the gray box. The detection setup in the interferometer output port as well as for the deflection angle of the 1064 nm light are highlighted by the orange boxes. The grayed out parts are not setup on the table at the moment. A detailed explanation of the optical setup is given in the text. The legend for the optics can be found in fig. A.1

we use the Pound–Drever–Hall technique [75]. An electro-optic modulator in front of the cavity imprints sidebands on the light. A photodiode placed in reflection of the ring cavity demodulates the measured signal at the sideband frequency to create the Pound–Drever–Hall error signal.

Part of the transmitted light through the mode cleaner can then be used as the local oscillator field for the optical homodyne detection which is currently not implemented (grayed out in fig. 4.12). The other part is transferred to the upper breadboard with a periscope. Since the piezo that changes the mode cleaner cavity length is not able to follow when the laser frequency is scanned over a large range, we also use an optical fiber to clean the mode and transfer it to the upper table. The beam paths from the fiber and the transmitted light are combined with a PBS on the upper breadboard. They both can be matched to a reference cavity, which is not set up at the moment (grayed out in fig. 4.12). This setup allows to scan the laser frequency for mode matching to the test mass while also matching the transmitted light from the mode cleaner.

Behind the PBS, a Faraday rotator is used to separate the back reflected light coming from the interferometer. In order to clean the polarization, a second PBS is used that is turned such that it reflects the light upwards into a beam dump. This way, the transmitted light has a clean s-polarization. After that, two lenses match the beam to the test mass cavity mode. After overlapping with the 1064 nm on the dichroic mirror, the beams are sent into the interferometer in the vacuum tank. For 1550 nm and s-polarization, the dichroic mirror has a power reflectivity of 99.4%. Behind the output port, a second periscope is used to shift the beam back down to the original beam height. A second dichroic mirror then filters out residual 1064 nm light that makes it through to the interferometer output. The 1550 nm beam is then split up for the quadrant photodiode (QPD) to measure the deflection and a single photodiode for the interferometric measurement signal.

4.5.2. 1064 nm Setup

The 1064 nm light is shown in blue color in fig. 4.12. Behind the laser head, again a Faraday isolator is used to prevent back reflection into the laser. The spatial mode of this laser is fine and no additional mode cleaner is needed. A PBS in combination with a half-waveplate is used to adjust the optical power to the interferometer. Behind that, the polarization is again cleaned to get s-polarized light. A mirror with low transmission is then used to pick up part of the back reflected light coming from the interferometer for the detection of the deflection angle. With another PBS, the optical power for the QPD can be adjusted. The reflected light of the pick-up mirror is mode matched to the test mass cavity with two lenses. A pair of mirrors afterwards is used to overlap the two wavelengths on the dichroic mirror.

For 1064 nm and s-polarization, the dichroic mirror has a power transmission of 99.2 %. Inside the interferometer, most of the 1064 nm light is transmitted through the beamsplitter, gets reflected from one side of the test mass and is mostly reflected back into the input port of the interferometer, where it is used for the detection of the deflection angle.

4.6. Laser

In order to provide the two wavelengths of 1550 nm and 1064 nm, we use two commercially available laser systems that will be discussed in this section.

4.6.1. 1550 nm

The 1550 nm laser is a fiber based seed and amplifier combination (Koheras BOOSTIK HP from NKT Photonics) providing a maximum CW output light power of 5 W. The laser frequency can be changed by applying an external voltage to a build in piezo that changes the fiber laser cavity length. The allowed voltage range is 0 V to 200 V. A self-build high voltage amplifier with a gain of 100 limits the output voltage to not exceed the maximum of 200 V to prevent damage to the laser. A second method for shifting the laser frequency is via the temperature which can be changed by hand in steps of 10 mK on the laser controller.

The following describes the calibration for the frequency scanning of the 1550 nm laser. With this calibration factor, the frequency shift can be calculated from the applied voltage, either to the laser piezo or temperature actuator. As a frequency reference, I used the triangular mode cleaner cavity with a FSR of 705 MHz with a build in piezo to scan the cavity length.

Piezo Scanning

To calibrate the piezo scanning, I applied a voltage ramp to the laser piezo through a high voltage amplifier with a gain of 100 and recorded the mode spectrum over one ramp slope as shown in fig. 4.13 on the left side. I extracted the positions of the peak values in the spectrum that are repeating after one FSR and the corresponding ramp voltage. The piezo calibration factor is then the slope of a linear fit through these three points as shown on the right of fig. 4.13 resulting in a frequency shift of 12.30(1) MHz V⁻¹.

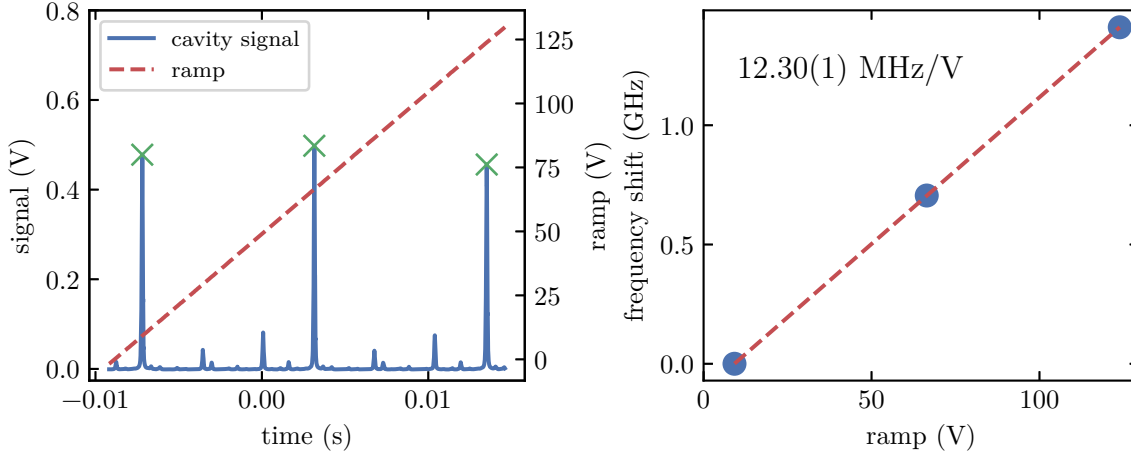


Figure 4.13.: Piezo frequency scanning calibration for the 1550 nm laser.

Left: Cavity transmission signal and voltage ramp to the piezo over time for one ramp slope. The ramp voltage is scaled by a factor 100 to show the actual voltage at the piezo through a high voltage amplifier. The crosses indicate the positions of one full cavity FSR.

Right: Frequency shift relative to the left most cavity mode calibrated via the known cavity FSR of 705 MHz against ramp voltage. The slope of the linear fit (dashed line) is the calibration factor for the piezo scanning of $12.30(1) \text{ MHz V}^{-1}$.

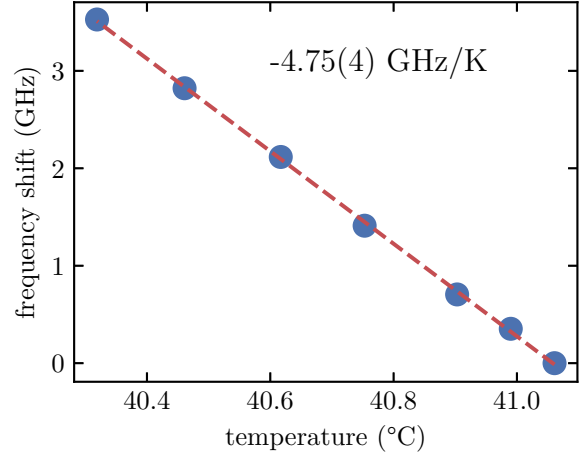
Temperature Scanning

For calibration of the frequency shifting via temperature, I scanned the length of the reference cavity with the piezo that is attached to the cavities back mirror with a fast ramp to get a mode spectrum on the oscilloscope. I marked the position of the first main peak and shifted the laser frequency by adjusting the laser temperature by hand until the peak one FSR further reached the mark. From these points and the corresponding temperature, the calibration factor is the slope of a linear fit, resulting in a frequency shift of -4.75 GHz K^{-1} .

4.6.2. 1064 nm

The 1064 nm laser is a solid-state Nd:YAG CW laser (Mephisto from Coherent) with a maximum output light power of 2 W. The output power can be modified with an external voltage in the range from -10 V to 10 V providing a modulation range of around 0 W to 2 W for the output power. The laser frequency can be changed with a bandwidth of around 1 Hz by temperature. This can be modified by an external voltage in the range -10 V to 10 V with a calibration factor of -3 GHz V^{-1} [76]. It also provides a fast scanning method with a piezo with an input voltage range of 0 V to 65 V with calibration factor of 1 MHz V^{-1} [76]. For this, we use a self-built high voltage amplifier that provides only up to the maximum allowed voltage.

Figure 4.14: Temperature frequency scanning calibration for the 1550 nm laser. The frequency shift was determined by scanning the cavity length with a piezo periodically to observe a mode spectrum. A marker on the oscilloscope was placed at the position of the highest visible mode and the laser frequency then changed slowly by temperature. After one cavity FSR of 705 MHz, the same mode was shifted onto the marker. The slope of the dashed line is the temperature calibration factor of -4.75 GHz K^{-1} .



4.7. Detection

We use two methods to detect the pendulum motion: Interferometric detection and detection of the deflection angle. The signals from the detector can either be recorded directly with a fast data acquisition card or with a digital lock-in amplifier providing the possibility to demodulate the signal with a local oscillator frequency and detect the quadrature components.

4.7.1. Interferometric Detection

For the interferometric detection, we currently use a single photodiode in the output port of the interferometer for the 1550 nm light. Since at the moment, the pendulum amplitude is still too high for a linear readout on a single fringe, this detection scheme is only used to estimate the pendulum amplitude for now (see section 5.4). At a later stage, we plan to use an optical homodyne detection scheme to operate at the dark port of the interferometer.

4.7.2. Deflection Angle

In order to be able to measure the pendulum motion at amplitudes exceeding a single interferometer fringe, we detect the deflection angle with a sensor that can measure the beam position. In the first stage of the experiment, we used a QPD (*OSI Optoelectronics FCI-InGaAs-Q3000*) in combination with a lens in the interferometer output port with the 1550 nm light. A QPD is a four segmented photodiode that is split horizontally and vertically as shown in fig. 4.15. Using the difference in

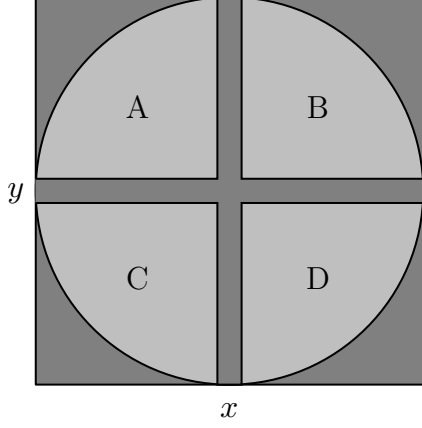


Figure 4.15: Schematic view of a QPD. The photodiode is split horizontally and vertically into 4 segments. Through the difference in photo current of the respective segments, one can determine the beam position in x - and y direction (see eq. (4.22)) linearly in a certain range. Once the beam fully crosses a split, the respective position signal becomes constant.

photo current I of the 4 segments, one can measure the vertical y and horizontal x position of a beam with a larger size compared to the width of the split as

$$x = \frac{(I_A + I_C) - (I_B + I_D)}{I_A + I_C + I_B + I_D} \quad (4.22)$$

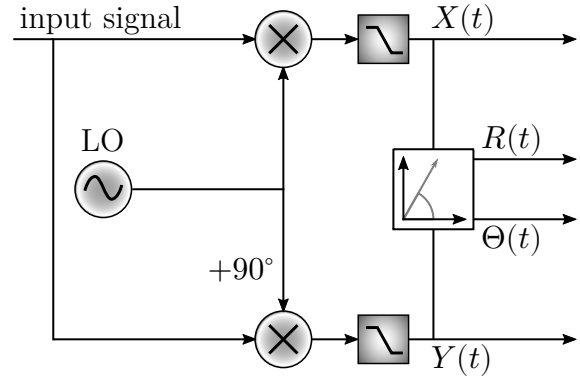
$$y = \frac{(I_A + I_B) - (I_C + I_D)}{I_A + I_C + I_B + I_D} \quad (4.23)$$

This position measurement is only linear in a certain range. For large amplitudes, when the beam only hits one side of the split, the signal becomes constant. The range can be adjusted by changing the QPD distance to the focus of the lens. However, this also changes the spot size and can lead to problems when the beam gets too small. Since the two reflected beams from the test mass move with a phase of 180 deg in opposite directions, the QPD would show no signal, when the interferometer is aligned. Thus, we purposely misalign the steering mirror in one interferometer arm to block the light on that side. In order to overcome these limitations, we are planning to use a 2D lateral effect position sensor (*Thorlabs PDP90A*) in the near future, which is only sensitive to the beam center position. Since it is not sensitive to 1550 nm, we changed the optical setup to allow for a small pick-off of the back reflected 1064 nm light in the input port. With this change, it is also possible to measure the deflection angle when the interferometer is aligned, since the beamsplitter is mostly translucent for 1064 nm light and the main part of the reflected light comes from a single pendulum side.

4.7.3. Data Acquisition Card

For direct sampling of the measurement signal, we use a data acquisition card (*National Instruments PCIE-6374*) with 16 bit resolution and a maximum sampling rate of 3.571 MS/s. For spectral analysis, we use Welch's method [50] on the time traces

Figure 4.16: Working principle of a lock-in amplifier. The input signal is split and mixed with a local oscillator (LO) signal and a LO-signal with a 90° phase shift, resulting in sum and difference frequencies. Subsequent low pass filtering removes the sum frequency and only keeps the slowly varying in-phase component $X(t)$ and quadrature component $Y(t)$ of the complex signal $Z(t) = X(t) + iY(t)$, which can also be displayed in polar coordinates with amplitude $R(t)$ and phase $\Theta(t)$ in the complex plane. The figure is based on [79].



to estimate the PSD. In order to fulfill the Nyquist–Shannon sampling theorem [77, 78], the sampling rate has to be at least twice as high as the frequency of interest. Especially for measurements of larger frequencies with high resolution, this can lead to big datasets, since the resolution bandwidth (RBW) depends on the measurement time.

4.7.4. Lock-In amplifier

We use a digital lock-in amplifier (*Zurich Instruments HF2*) to measure in-phase and quadrature component from demodulation with a local oscillator. The working principle of a lock-in amplifier is shown in fig. 4.16. The input signal is multiplied with the local oscillator (LO) and a 90° phase shifted version of the LO resulting in a complex signal Z with components at the sum and difference frequency. Subsequent low pass filtering removes the sum frequency component, leaving only a slowly varying signal $Z(t) = X(t) + iY(t) = R(t)e^{i\Theta}$ with amplitude $R(t)$ and phase $\Theta(t)$ or in-phase component $X(t)$ and quadrature component $Y(t)$. The lock-in amplifier can also use a fast Fourier transform (FFT) on the demodulated signal to convert to the frequency domain.

A so-called zoom FFT allows for long measurements with a high resolution around a specific frequency, without the need to have a high sampling rate, since the effective sampling rate only needs to be able to detect frequencies inside the low pass filter bandwidth around the LO. [79]

5. Experimental Results

In the following chapter, I present my experimental results. I start with the characterization of the test mass cavity by scanning the laser frequency. Using the QPD detection scheme, I analyze the pendulum spectrum and determine the oscillator parameters for multiple pendulum modes by fitting the resonance spectra. Additionally, I show ringdown measurements where the main pendulum mode was excited parametrically before observing the decaying power of the pendulum motion. Furthermore, I estimate the seismically excited amplitude of the pendulum movement with the interferometric detection scheme and show the pendulum motion in the phase space of quadrature components.

5.1. Test Mass Internal Cavity

In order to characterize the test mass internal cavity, I used a test setup outside of the vacuum chamber where the test mass is placed at the same optical path length as inside the interferometer to maintain the mode matching to the beam (green box in fig. 4.12). I overlapped the 1064 nm and 1550 nm beams over a long distance to align both beams simultaneously to the test mass. I measured the transmitted 1064 nm light with a photodiode while scanning the laser frequency via the crystal temperature. I could observe a frequency dependence of the transmission as shown in fig. 5.1. The two dashed vertical lines indicate one $\text{FSR} = 4.2 \text{ GHz}$ of the test mass. However, this transmission was insensitive to misalignment in position and angle. The width of the transmission peaks is much broader than expected from the theoretical cavity parameters in table 4.6.

Figure 5.2 shows the spatial profile of the transmitted light on a beam profiler. It is distorted and does not show a clean spatial mode. It also moves when moving the incoming beam. Moving the incoming beam also has no effect on the distortion of the transmitted beam shape. This lets suspect that there is no well defined optical cavity axis present inside the test mass and only partial interference occurs due to the reflection on the slightly curved surfaces. The optical axis of a two mirror cavity is the line intersecting the two centers of curvature [80]. Since the radii of curvature are large compared to the dimensions of the test mass, a slight misalignment of the

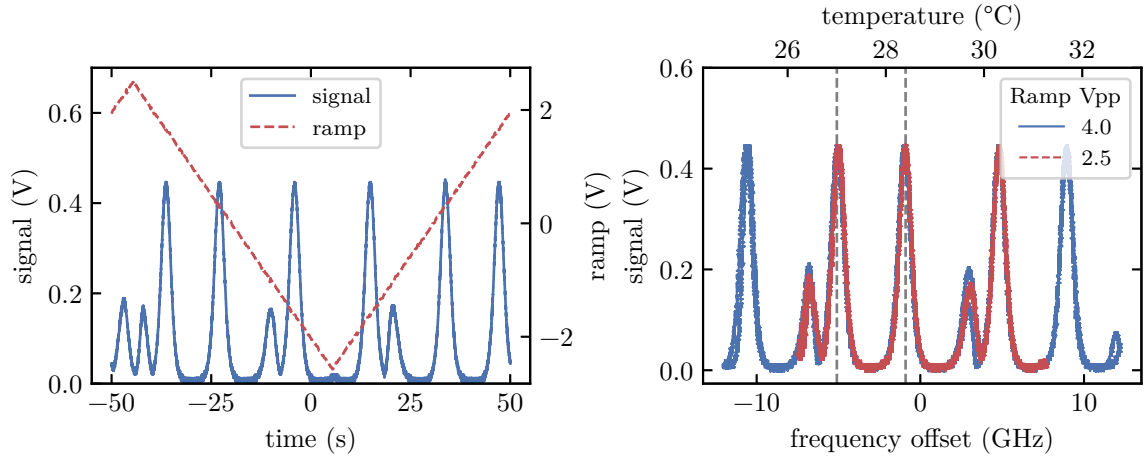


Figure 5.1.: Transmission signal of the test mass cavity while scanning the frequency of the 1064 nm laser by changing the crystal temperature.

Left: Transmission signal and voltage ramp that controls the laser frequency vs. time.

Right: Transmission signal vs. laser frequency offset (laser crystal temperature). The frequency offset is calculated from the ramp voltage via the conversion factor -3 GHz V^{-1} that is given by the manufacturer. The two dashed lines indicate a distance of one FSR = 4.2 GHz that is calculated from the cavity length via eq. (3.29). There are two transmission peaks that have the same frequency distance. The smaller peaks are most likely mode jumps of the laser.

center points would result in an optical axis that lies outside of the test mass. This is illustrated on the right side in fig. 5.2. Here, the angle of the curved surfaces is drastically exaggerated for visibility. Also the RoC is shown much smaller compared to the expected cavity length l_{cav} .

Figure 5.3 shows a frequency scan with the 1550 nm laser where the test mass coatings have a higher reflectivity. I scanned the frequency via the internal laser piezo by applying a ramped voltage to a high voltage amplifier. During the fast piezo scan, I adjusted the laser temperature by hand, until a signal in the transmitted light could be observed. The right side in fig. 5.3 shows the signal against the frequency offset, which is calculated with the calibration factor 12.3 MHz V^{-1} from fig. 4.13. Only a small peak is visible, which is barely higher than the noise floor. The width of the peak is approximately 1 GHz.

5.2. Pendulum Modes

In order to get an overview of the pendulum modes, I took a zoom FFT (see section 4.7.4) measurement of the vertical and horizontal channel on the QPD with a measurement time of 5.2 h which corresponds to RBW of $54 \mu\text{Hz}$. Figure 5.4 shows

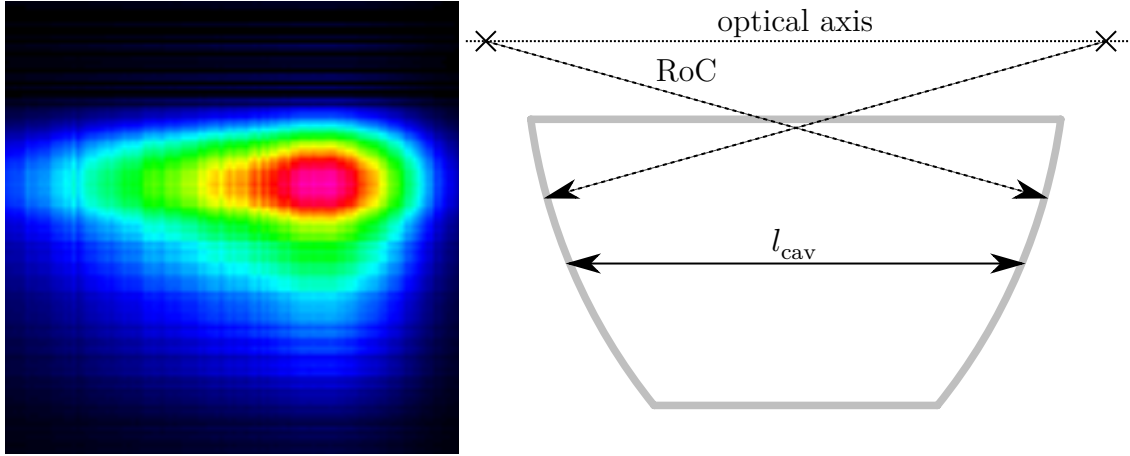


Figure 5.2.:

Left: Transverse spatial profile of the transmitted light from the test mass. It shows a distortion with two "tails" coming from the central Gaussian shaped part.

Right: Illustration of the suspected problem with the test mass cavity. The optical axis that connects the two centers of curvature lies outside of the monolithic test mass. The angle of the curved surfaces is drastically exaggerated for visibility. Also the RoC is shown much smaller compared to the expected cavity length l_{cav} .

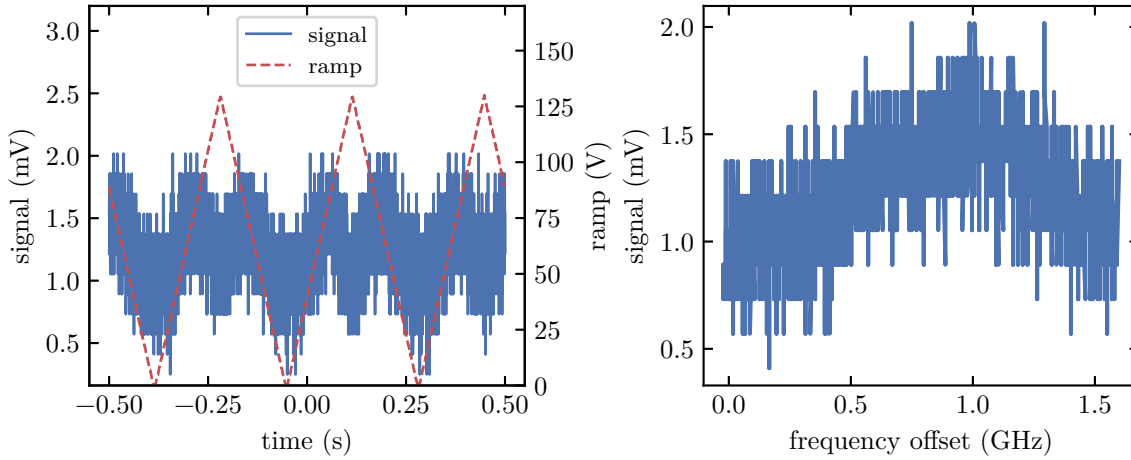


Figure 5.3.: Transmission signal of the test mass cavity while scanning the frequency of the 1550 nm via the piezo actuator. During this procedure, the laser temperature was changed until some signal was visible that is shown here.

Left: Transmission signal and voltage ramp that controls the laser frequency vs. time.

Right: Transmission signal vs. laser frequency offset. The frequency offset is calculated from the ramp voltage via the calibration factor 12.3 MHz V^{-1} from fig. 4.13.

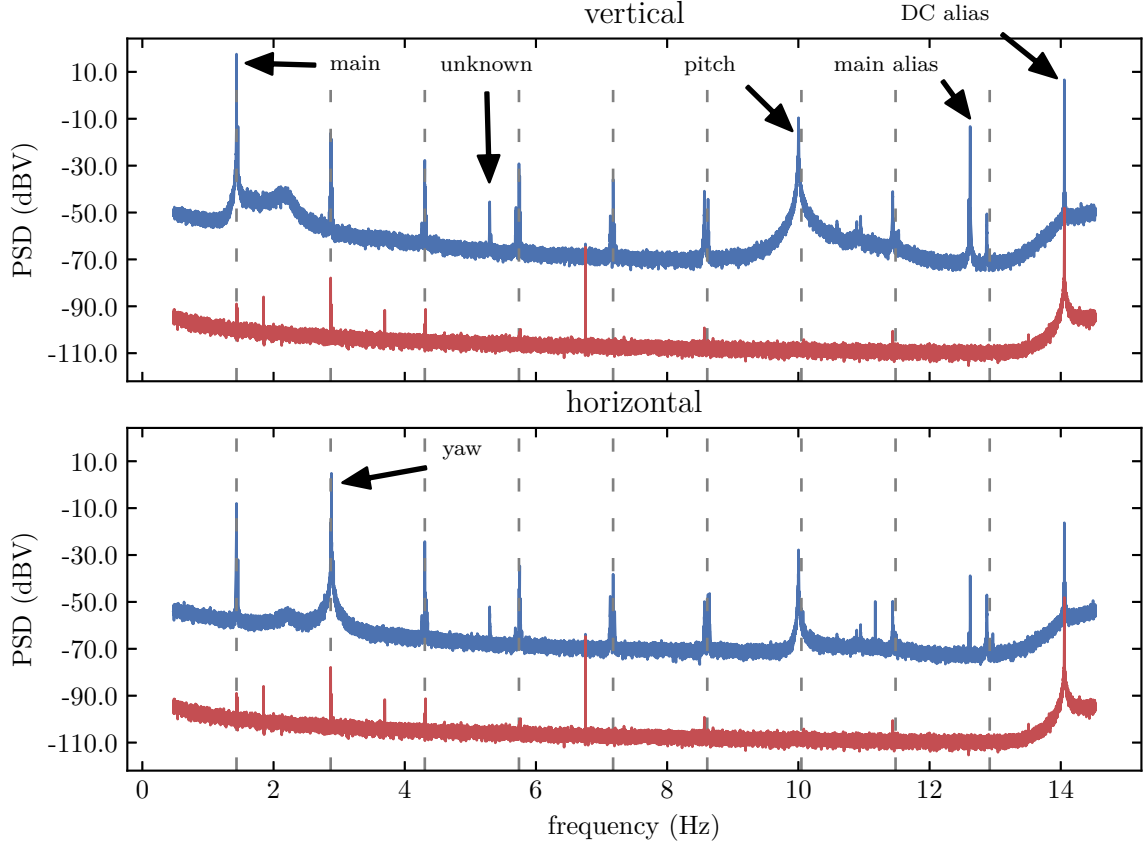


Figure 5.4.: Broadband mode spectrum for the vertical and horizontal channel of the QPD from a zoom FFT. The lower red traces show the dark noise. The average PSD of three individual measurement runs is shown. The measurement time for each run was 5.2 h corresponding to a RBW of 54 μ Hz. The first peak corresponds to the main pendulum mode at 1.435 Hz. Higher harmonics of this mode due to the nonlinearity of the QPD are marked with grey dashed lines. Two additional peaks due to aliasing from the FFT are present at the right side of the spectrum coming from the main peak at negative frequency and the DC peak that lie outside of the measurement window. In the vertical channel, the main and pitch (10 Hz) mode are dominant. In the horizontal channel, the highest peak corresponds to the yaw mode at 2.88 Hz.

the average of three such individual measurement together with the detector noise floor. One can see multiple peaks of different origin. The left peak corresponds to the main pendulum at $f \approx 1.435$ Hz. Due to the QPD's nonlinearity, additional peaks at higher harmonics of this frequency are visible in the spectrum. The gray dashed lines indicate those frequencies. The height of these peaks decrease with higher frequency.

At $f \approx 10$ Hz, a broader peak is visible, which corresponds to the pitch mode of the pendulum. Another peak is present at $f \approx 5.3$ Hz which is of unknown origin. Due to the periodicity of the FFT, two alias peaks coming from a DC peak and the main peak at negative frequency that lie outside of the measurement span are present in the spectrum. They are shifted by the measurement span of 14 Hz, since they are not far enough outside of the window to be fully attenuated by the low pass filter.

In the horizontal spectrum, the main contribution comes from the yaw mode at $f \approx 2.88$ Hz which is very close to the second harmonic of the main mode. This imposes a challenge for the parametric actuation at this frequency (see section 5.3).

One can also see the main and pitch pendulum modes. They are attenuated compared to the vertical channel, but this shows that the pendulum axes are not perfectly mapped to the QPD axes. This could be improved by rotating the QPD around the beam axis.

For fitting the individual pendulum mode spectra, I assume a constant white seismic noise C over the mode spectrum that drives the pendulum according to eqs. (2.25) and (2.30) with an additional detector noise level n_d resulting in the fit function

$$\begin{aligned} S(f, (f_0, C, n_d)) &= C \cdot |H(f)|^2 + n_d \\ &= C \cdot \frac{Q^2}{16\pi^4 m^2 (Q^2 (f^2 - f_0^2)^2 + f^2 f_0^2)} + n_d \end{aligned} \quad (5.1)$$

with the mass pendulum mirror $m = 47.657 \times 10^{-3}$ kg. I determined the initial fit values by hand and fitted with the non-linear least squares algorithm provided by the `curve_fit` function of SciPy [51, 52].

5.2.1. Main Pendulum Mode

Figure 5.5 (left) shows a zoomed in spectrum around the main pendulum mode at 1.4352 Hz which is averaged over three individual measurement traces with a measurement time of 10.4 h corresponding to a RBW of 27 μ Hz. The dark noise is also shown in red which is more than 50 dB below the detector noise floor. The main peak is approximately 60 dB above the detector noise floor. To the right of

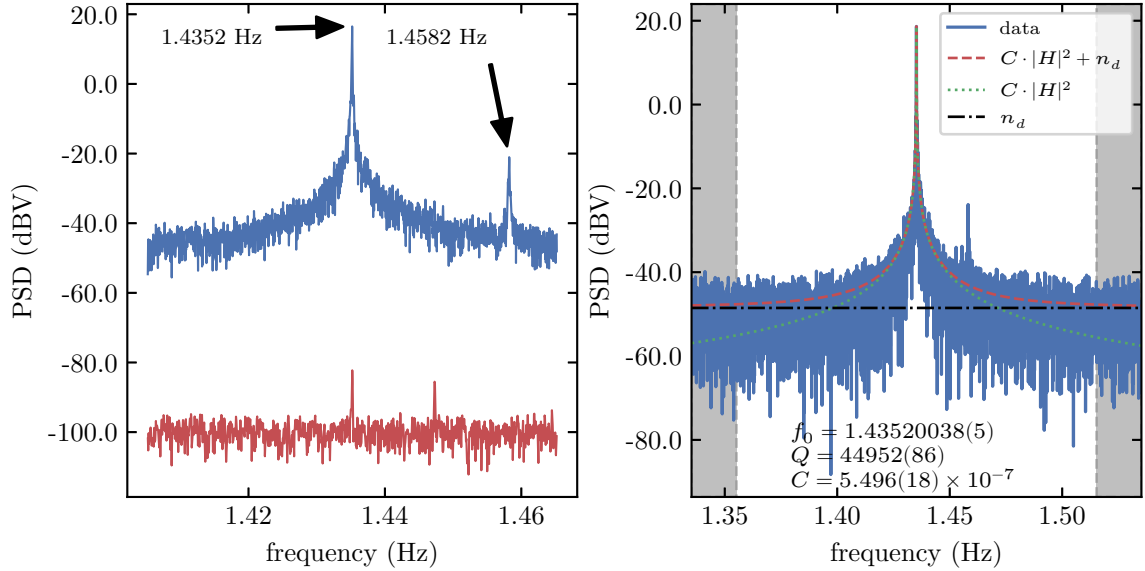


Figure 5.5.: PSD for the main pendulum mode. The measurement time was 10.4 h corresponding to a RBW of 27 μ Hz.

Left: The average PSD of three individual measurement runs is shown. The lower red trace shows the dark noise. The upper trace shows the vertical QPD signal. To the right of the main peak at 1.4352 Hz one can see a second peak at 1.4582 Hz, which is probably the perpendicular pendulum mode $f_{0,\text{perp}}$.

Right: Fit of eq. (5.1) to the main pendulum peak. The black dash-dotted line represents the detector noise n_d that is averaged over the gray shaded region. The red dashed line shows the fitted function including detector noise while the green dotted line represents only the oscillator spectral density from the fit parameters that are shown below.

the main pendulum peak in the center one can see a second peak with a slightly higher frequency of 1.4582 Hz, which is likely the perpendicular pendulum mode (see table 4.4). It is less prominent and approximately 20 dB above the noise floor.

In order to determine the Q factor and the center frequency of the main pendulum mode, I fitted eq. (5.1) to multiple single traces. These traces were taken on the weekends and over night, since the measurement was sensitive to seismic disturbances due to human activities which were present in the laboratory during normal working hours. An example of such a fit is shown in fig. 5.5 on the right. The red dashed line shows the fit function from eq. (5.1) with the added detection noise floor n_d (black dash dotted line), while the green dotted line shows the underlying resonance peak without the noise. The detection noise floor is determined as the average over the gray shaded area at the edges.

Table 5.1 shows the fitted parameters for six of such traces. The fits are shown in fig. B.1 in appendix B. The averaged center frequency is $f_{0,\text{main}} \approx 1.4352$ Hz with an average Q factor $Q_{\text{main}} \approx 4.1 \times 10^4$ which results in an amplitude decay time of ≈ 2.5 h (see eq. (2.15)). Most fitted Q factors for the individual measurements are within 25 % around the average value except for measurement 3. Here the fitted Q factor is 65 % higher then the average. Since I could observe small drifts of the center frequency between measurements, the actual Q factor could be higher then the average value, and the lower Q factors might come from an averaging effect of a shifting peak during a single measurement. So the average value might be a lower bound for the actual Q factor. An upper bound can be determined by a ringdown measurement (see section 5.3)

5.2.2. Yaw and Pitch Mode

In this section, I analyze the parameters of the yaw and pitch mode with the same method as above.

Figure 5.6 shows a zoomed in spectrum onto the yaw mode at 2.88 Hz in the horizontal QPD signal. The left side shows the averaged spectrum over three individual traces (RBW = 27 μ Hz). The dashed vertical lines indicate the second harmonics of the main (2.87 Hz) and perpendicular (2.916 Hz) pendulum mode. As the second harmonic of the main mode is rather close, it is possible to excite the yaw mode by actuating at this frequency. This imposes a problem for parametric actuation, which is most efficient at twice the oscillators eigenfrequency. This is why we use the fundamental frequency of the main pendulum mode for parametric excitation at the moment. It could be beneficial to separate these two modes in the future for example by shortening the pendulum length.

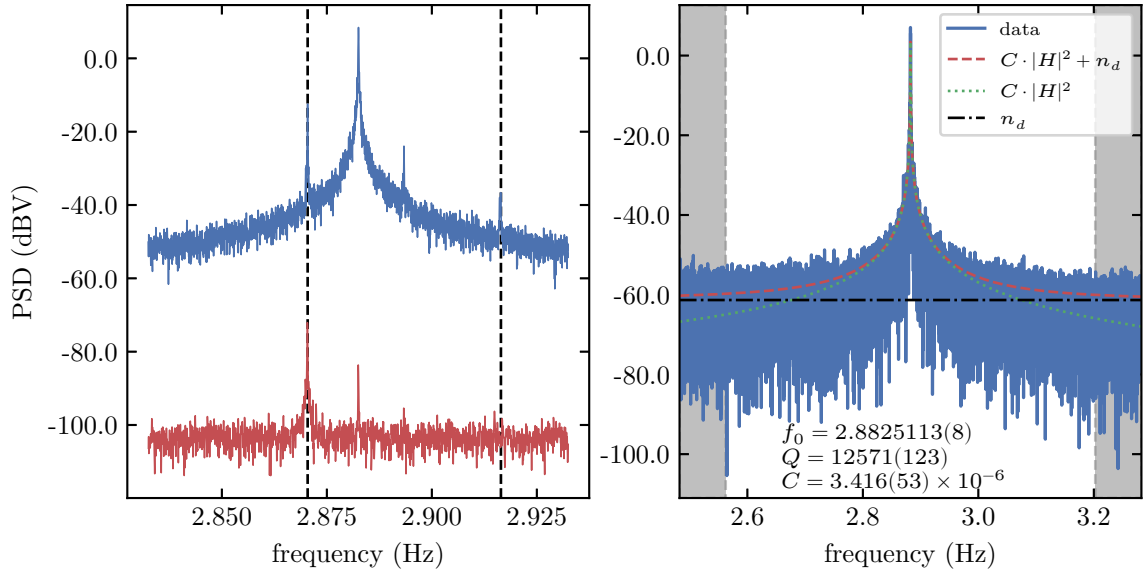


Figure 5.6.: PSD for the yaw mode. The measurement time was 10.4 h corresponding to a RBW of 27 μ Hz.

Left: The average PSD of three individual measurement runs is shown. The lower red trace shows the dark noise. The upper trace shows the horizontal QPD signal. The vertical black dashed lines indicate harmonics of the main and perpendicular pendulum modes.

Right: Fit of eq. (5.1) to the yaw pendulum peak. The black dash-dotted line represents the detector noise n_d that is averaged over the gray shaded region. The red dashed line shows the fitted function including detector noise while the green dotted line represents only the oscillator spectral density from the fit parameters that are shown below.

Table 5.1.: Fitted parameters of eq. (5.1) fit uncertainty for the main pendulum mode of multiple spectral measurements. The corresponding plots to the fits can be seen in fig. B.1 in the appendix. The center frequencies f_0 of all measurements agree to the precision of the lowest RBW of the measurement series of 54 μHz . The fitted Q factors lie in the order of magnitude of 4×10^4 . The third measurement results in a larger Q factor which could be the result of an averaging effect in the other traces over the long measurement time when the pendulum frequency shifts slightly due to thermal effects during the measurement. The averaged Q factor over all measurement thus might be a lower bound for the actual Q factor of the pendulum.

	f_0 (Hz)	Q	C ($\text{V}^2\text{N}^2/(\text{m}^2\text{Hz})$)	n_d (V^2)
1	1.435204543(71)	29264(111)	$6.363(37) \times 10^{-7}$	$1.6(1.5) \times 10^{-5}$
2	1.435200378(33)	44953(60)	$5.496(13) \times 10^{-7}$	$1.3(1.3) \times 10^{-5}$
3	1.4352024677(54)	67325(254)	$1.1237(32) \times 10^{-5}$	$1.5(2.0) \times 10^{-5}$
4	1.435227672(14)	35283(71)	$1.5418(41) \times 10^{-6}$	$1.1(1.2) \times 10^{-5}$
5	1.435198255(19)	29425(43)	$5.847(13) \times 10^{-6}$	$1.1(1.1) \times 10^{-5}$
6	1.43524569(11)	38204(213)	$2.855(26) \times 10^{-6}$	$1.2(1.3) \times 10^{-5}$
average	1.435213(19)	40743(14286)	$3.8(4.1) \times 10^{-6}$	$1.29(23) \times 10^{-5}$

The right side of fig. 5.6 shows a fit of eq. (5.1) to the yaw mode peak of a single measurement trace. Table 5.2 displays the fitted value for three such measurements with average center frequency of $f_{0,\text{yaw}} \approx 2.8826 \text{ Hz}$ with an average Q factor $Q_{\text{yaw}} \approx 1.3 \times 10^4$ which results in an amplitude decay time of $\approx 24 \text{ min}$ (see eq. (2.15)). The parameters for the individual measurements are within 5 % around the average value. The individual fits can be seen in fig. B.2 of appendix B.

Figure 5.7 shows a zoomed in spectrum onto the pitch mode at 10.0 Hz in the vertical QPD signal. The left side shows the averaged spectrum over three individual traces (RBW = 27 μHz). The dashed vertical lines indicate peaks at the sum and difference frequency with the main pendulum mode. This could be due to nonlinear coupling of the two modes [81]. If this is the case, it might be possible to observe an autparametric resonance [82], since the two modes have eigenfrequencies with a nearly integer ratio. This has to be investigated further.

On the right side of fig. 5.7 a fit of eq. (5.1) to the pitch mode is shown. The fit parameters for eight of such measurements is displayed in table 5.3. The average center frequency is $f_{0,\text{pitch}} \approx 10.003 \text{ Hz}$ with an average Q factor $Q_{\text{pitch}} \approx 4.1 \times 10^3$. This results in an amplitude decay time of $\approx 130 \text{ s}$ (see eq. (2.15)). The individual fits can be seen in fig. B.3 of appendix B.

Table 5.2.: Fitted parameters of eq. (5.1) fit uncertainty for the yaw mode of multiple spectral measurements. The corresponding plots to the fits can be seen in fig. B.2 in the appendix. The center frequencies f_0 of all measurements agree to the precision $100 \mu\text{Hz}$ which is less precise than the minimal RBW of $54 \mu\text{Hz}$. The fit errors are below the RBW. Thus, the observed frequency shift could be a frequency shift due to thermal effects. The fitted Q factors are around 1.3×10^4 .

	f_0 (Hz)	Q	C ($\text{V}^2\text{N}^2/(\text{m}^2\text{Hz})$)	n_d (V^2)
1	2.88251128(79)	12571(123)	$3.416(53) \times 10^{-6}$	$7.4(7.7) \times 10^{-7}$
2	2.88253703(33)	13910(63)	$1.550(11) \times 10^{-6}$	$6.9(7.2) \times 10^{-7}$
3	2.8826079(14)	12809(225)	$1.566(43) \times 10^{-6}$	$6.6(7.2) \times 10^{-7}$
average	2.882552(50)	13096(714)	$2.2(1.1) \times 10^{-6}$	$6.95(38) \times 10^{-7}$

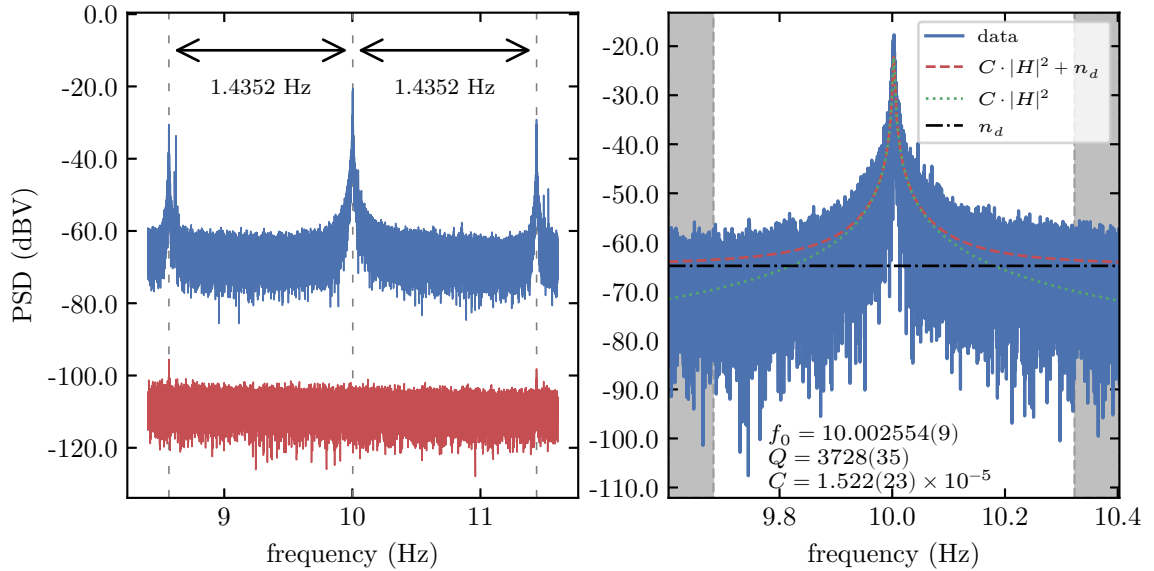


Figure 5.7.: PSD for the pitch mode. The measurement time was 10.4 h corresponding to a RBW of $27 \mu\text{Hz}$.

Left: The average PSD of three individual measurement runs is shown. The lower red trace shows the dark noise. The upper trace shows the vertical QPD signal. The dashed vertical lines indicate the sum and difference frequency peaks of the pitch and the main mode.

Right: Fit of eq. (5.1) to the pitch pendulum peak. The black dash-dotted line represents the detector noise n_d that is averaged over the gray shaded region. The red dashed line shows the fitted function including detector noise while the green dotted line represents only the oscillator spectral density from the fit parameters that are shown below.

Table 5.3.: Fitted parameters of eq. (5.1) fit uncertainty for the pitch mode of multiple spectral measurements. The corresponding plots to the fits can be seen in fig. B.3 in the appendix. The center frequencies f_0 of all measurements agree to the precision 1 mHz which is less precise than the minimal RBW of 54 μ Hz. The fit errors are below the RBW. Thus, the observed frequency shift could be a frequency shift due to thermal effects. The fitted Q factors are around 4×10^3 .

	f_0 (Hz)	Q	C ($V^2 N^2 / (m^2 Hz)$)	n_d (V^2)
1	10.002554(10)	3728(40)	$1.522(26) \times 10^{-5}$	$2.4(2.5) \times 10^{-7}$
2	10.002321(11)	3974(49)	$1.170(23) \times 10^{-5}$	$2.4(2.5) \times 10^{-7}$
3	10.002908(10)	3981(47)	$1.027(19) \times 10^{-5}$	$2.4(2.5) \times 10^{-7}$
4	10.0022887(87)	4395(48)	$2.008(34) \times 10^{-4}$	$1.8(1.9) \times 10^{-7}$
5	10.002482(13)	3598(48)	$2.229(47) \times 10^{-4}$	$1.8(1.9) \times 10^{-7}$
6	10.0026741(85)	5082(62)	$1.177(23) \times 10^{-4}$	$1.8(1.9) \times 10^{-7}$
7	10.002750(12)	4500(66)	$2.277(53) \times 10^{-4}$	$1.8(1.9) \times 10^{-7}$
8	10.002697(13)	3356(43)	$1.518(31) \times 10^{-4}$	$1.8(1.9) \times 10^{-7}$
average	10.00258(21)	4077(558)	$1.20(96) \times 10^{-4}$	$2.07(31) \times 10^{-7}$

In conclusion, the fitted Q factor for the main pendulum mode is much higher than for the yaw and pendulum mode. This is expected due to the dilution factor, since the energy for the main mode is stored in the lossless gravitational field. The Q factor for the pitch mode is the lowest, since the energy is stored in lossy elastic deformation of the wires. The Q factor for the yaw mode is between those of the other modes, which hints to part of the energy being stored in elastic deformation and not in the gravitational field. This is also consistent with the expectation since the model in section 4.3.3 only considers gravity and predicts a lower eigenfrequency than what I measured.

5.2.3. Violin Modes

In order search for the violin modes, I took a broadband spectrum of the vertical QPD signal up to 1.4 kHz and averaged over multiple traces to remove noise peaks. I searched through the spectrum over small frequency ranges to identify possible candidates for the violin modes. The left plot of fig. 5.8 shows a prominent double peak which I suspect to be the first violin mode. The split peak comes likely from small length difference between the suspension wires. The dashed vertical line indicates the maximum of the highest peak at 357.8 Hz. In the center and right plot of fig. 5.8, the dashed lines indicate the second and third harmonic of this peak frequency. In the spectrum one can also see two split peaks, where the highest one

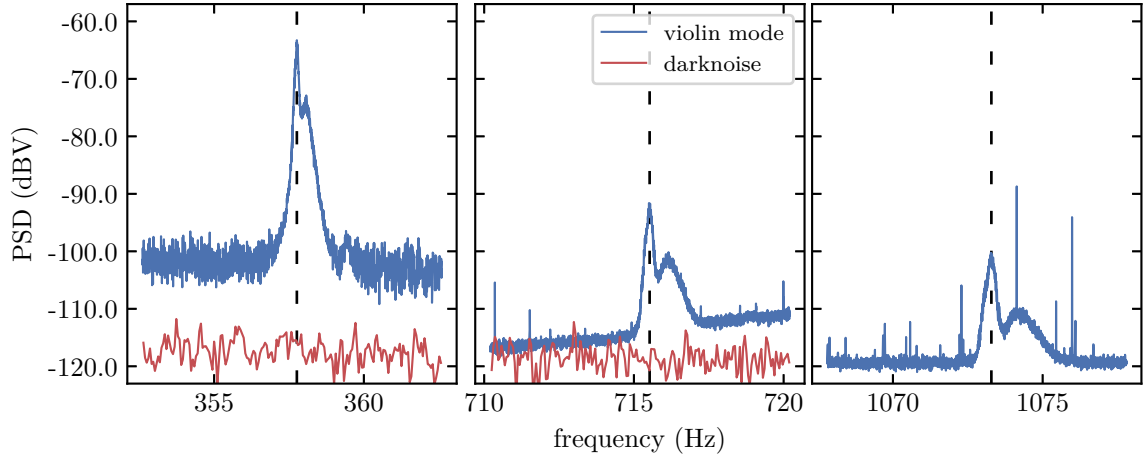


Figure 5.8.: Spectrum of the suspected violin modes. The left plot shows the suspected first violin mode in the spectrum of the vertical QPD signal. The dashed vertical line indicates the frequency of the maximum. In the center and right plot the dashed lines indicate the second and third harmonic of this frequency, respectively, which also show a similar shaped feature in the recorded QPD signal. One can see two overlapping peaks that might correspond to violin modes originating from suspension wires with slightly different lengths.

coincides with the dashed line. The overall shape of the split peaks is also similar to the suspected first violin mode. This is another strong indicator that these are in fact the first three violin modes. However, the frequencies do not fit to the theoretical values in table 4.4. This might be due to partly plastic deformation of the suspension wire since the stress on the tungsten wires is already near the yield strength of the material.

5.2.4. Additional Modes

Additionally to the three pendulum modes discussed above, I looked for additional peaks in the pendulum spectrum. Since the expected modes, like the roll and bounce mode, do not couple very much to the deflection angle, these peaks are expected to be very small. I used a broadband spectrum of the vertical QPD signal recorded with the lock-in amplifier at a demodulation frequency of 0 Hz giving a symmetric two sided spectrum centered around DC. This avoids alias peaks at higher frequencies. Figure 5.9 shows the positive frequency part in the top. In order to identify harmonic peaks of the main and pitch mode as well as the grid frequency of 50 Hz, I marked multiples of these frequencies inside the spectrum and only considered unmarked peaks to be possible pendulum modes. Zooms on these peaks are shown in fig. 5.9 on the bottom with the center frequency indicated above. The peaks at 38.505 Hz and 44.85 Hz fit well to the calculated values in table 4.4 for the roll and bounce

Table 5.4.: Center frequencies of detected peaks in the power spectrum of the vertical and horizontal QPD signal. Pendulum modes that are likely to correspond to these peaks are indicated. Some peaks could not be matched with particular pendulum modes and are marked as unknown.

frequency (Hz)	mode
1.4352	main
1.4582	perpendicular
2.883	yaw
10.003	pitch
26.83	unknown
31.24	unknown
38.505	roll
44.85	bounce
197.925	unknown
357.8	1st violin
715.6	2nd violin
1073.4	3rd violin

mode, respectively, with the assumed pendulum parameters. The other peaks might be oscillation modes of the suspension system.

An overview of all observed peaks in the pendulum spectrum is given in table 5.4. Identified pendulum modes that likely correspond to these peaks are indicated.

5.3. Pendulum Ringdown

Another way to determine the Q factor besides fitting the resonance peak is a ring-down measurement. For this, I excited the main pendulum mode parametrically for 20 min with a frequency generator connected to the driving piezo via a low pass filter in order to avoid a sudden movement when starting the excitation. I used the fundamental mode frequency 1.4352 Hz and not the second harmonic, since the yaw mode is very close to that frequency and gets easily excited instead. After the excitation time, the frequency generator was turned off and the pendulum amplitude could decay. I repeated this procedure multiple times with 6 h in between measurements for the pendulum amplitude to decrease to a point where another excitation could be safely performed. I measured the amplitude with the lock-in amplifier by demodulating at the mode frequency with a low pass filter bandwidth of 100 mHz

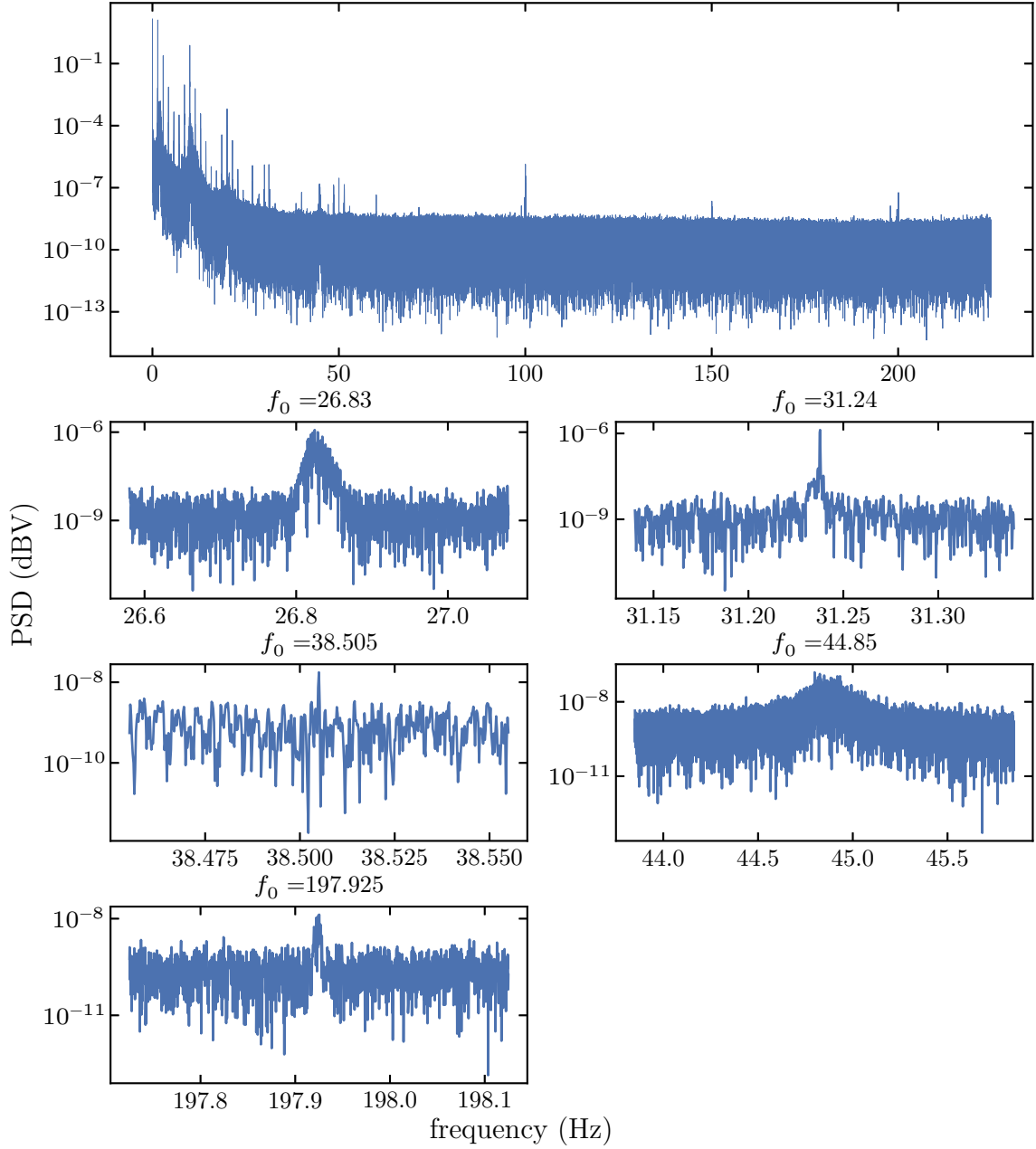


Figure 5.9.: Search for additional pendulum modes.

Top: Broadband power spectrum of the vertical QPD signal from 0 Hz to 225 Hz recorded with the lock-in amplifier with a demodulation frequency of 0 Hz to avoid alias peaks at higher frequencies. The negative frequency part of the spectrum is not shown here.

Bottom: Zoom on additional peaks in the broadband spectrum which are not caused by higher harmonics of the main and pitch mode frequencies or the grid frequency of 50 Hz. For each peak, the center frequency f_0 is indicated above. The peaks at 38.505 Hz and 44.85 Hz are close to the calculated values in table 4.4 for the roll and bounce mode, respectively.

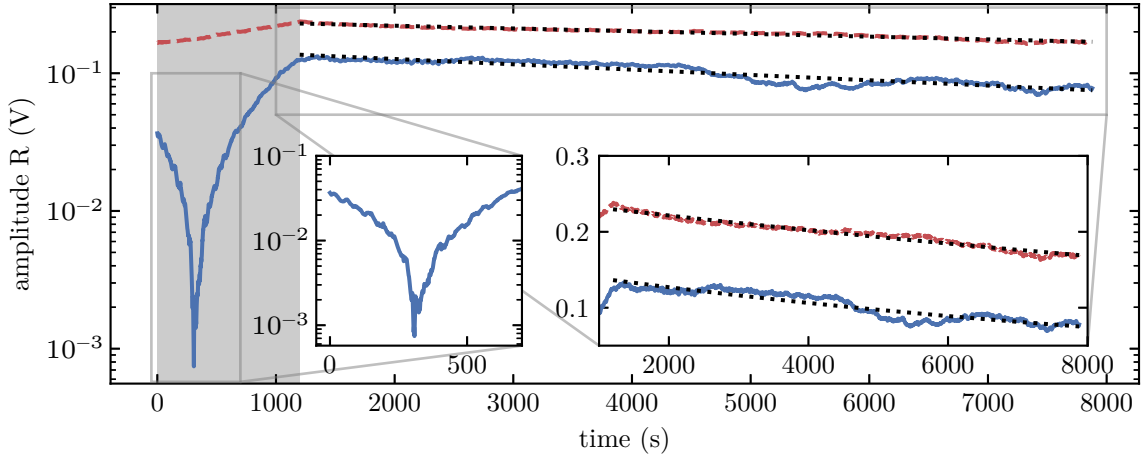


Figure 5.10.: Ringdown measurement of the main mode amplitude R measured with a lock-in amplifier demodulating at the mode center frequency with a low pass filter of 100 mHz. The pendulum is excited parametrically for 20 min (gray shaded area) at the mode frequency via a frequency generator connected to the suspension piezo actuator. The right inset shows the ringdown section with a linear amplitude scale. The dotted lines show the corresponding fit of the exponential decay from eq. (5.2). The left inset shows a zoom onto the excitation phase, where the parametric phase lead first to a reduction of the pendulum motion before the pendulum phase adjusted to parametric heating.

which is essentially a zero span measurement on a classical spectrum analyzer. Figure 5.10 shows two of such measurement traces in logarithmic amplitude scale and in linear scale in the right inset. The black dotted lines indicate a fit of an exponential decay

$$R(t) = A \exp\left(-\frac{t}{\tau}\right) \quad (5.2)$$

with the ringdown time τ and initial amplitude A . The fits start, where the parametric excitation was switched off. An interesting feature can be seen in the inset on the left. Due to an arbitrary phase at the start of the parametric excitation compared to the pendulum, it happened to first cool down the pendulum motion, before the pendulum phase adjusted to parametric heating. Here, the amplitude was reduced by 1.5 orders of magnitude. For continuous cooling, the phase would have to be adjusted by active feedback.

Table 5.5 shows the fit results for ringdown traces recorded over multiple days. The corresponding Q factor can be calculated from the ringdown time with

$$Q = \frac{2\pi f_0 \tau}{2}, \quad (5.3)$$

where I used a center frequency of $f_0 = 1.4352(2)$ Hz. The error accounts for small drifts of the mode frequency between measurements. The average Q factor is $76(17) \times 10^3$ and thus higher then the one determined by the fits to the spectral

Table 5.5.: Fit results for the ringdown measurements of the main pendulum mode with eq. (5.2). The Q factor is calculated from the decay time τ with eq. (5.3) and the main mode frequency $f_{0,\text{main}} = 1.4352(2)$ Hz, where the error in the frequency should account for shifts of the center frequency between measurements. The corresponding ringdown measurements and fits are shown in fig. C.1 in appendix C.

	τ (s)	A (V)	Q
1	$1.1245(57) \times 10^4$	0.15166(30)	$5.070(26) \times 10^4$
2	$1.8354(47) \times 10^4$	0.25812(16)	$8.276(21) \times 10^4$
3	$1.9416(32) \times 10^4$	0.26515(10)	$8.754(14) \times 10^4$
4	$2.1897(53) \times 10^4$	0.24258(12)	$9.873(24) \times 10^4$
5	$1.4618(13) \times 10^4$	0.71104(40)	$6.5911(61) \times 10^4$
6	$1.5235(11) \times 10^4$	0.84634(36)	$6.8692(50) \times 10^4$
average	$1.68(38) \times 10^4$	0.41(29)	$7.6(1.7) \times 10^4$

signal. Since it was not possible to excite the pendulum to a higher initial amplitude above the seismic noise due to the limitations of the QPD non-linearity and to not risk damaging the pendulum, the measured ringdown time is likely extended by additional seismic excitation. Thus, the measured average value can be considered as an upper bound for the actual Q factor.

5.4. Amplitude Estimation

In order to get an estimate of the pendulum oscillation amplitude due to the seismic excitation, I used the interferometric output signal as shown in fig. 5.11. The two beams in the interferometer arms were aligned with the steering mirrors for a maximum contrast and a symmetric signal. I reached a maximum contrast of 91 %. With this alignment, the two reflected beams have the most overlap when the pendulum crosses its equilibrium position. The top of fig. 5.11 shows the output signal over multiple pendulum oscillations. The maximum contrast is reached after a full pendulum oscillation period as indicated by the dashed vertical lines. The local maximum in between these two points is lower, which is likely caused by an excitation of the yaw pendulum mode which is nearly double the main pendulum frequency (see section 5.2). The decreasing contrast is caused by the deflection of the two interfering beams by the pendulum angle. At the turning point of the pendulum, one beam is deflected maximally upwards while the other is deflected maximally downwards. The bottom of fig. 5.11 is a zoom onto half a pendulum oscillation going from turning point to turning point. From these points, the frequency

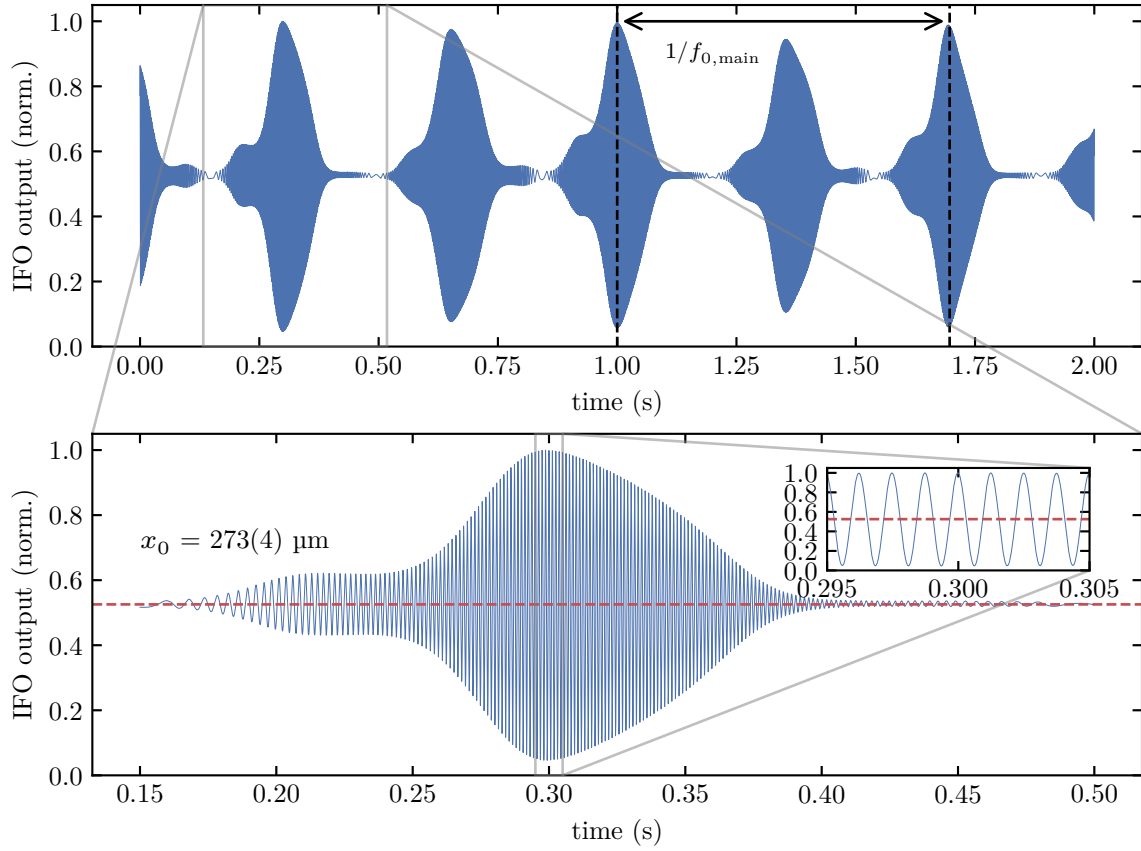


Figure 5.11.: Pendulum amplitude estimation from the interferometric signal. The interferometer output power was measured with a photodiode and recorded with a sampling rate of 28.78 kHz and a low pass filter bandwidth of 5 kHz. It is normalized to the maximum value.

Top: Interference signal over multiple pendulum oscillations. One can see an oscillating interferometer contrast that repeats with the frequency of the main pendulum mode as indicated by the black dashed vertical lines. The pendulum swings over multiple wavelengths and the frequency of the interferometer fringes increases when the pendulum swings from a turning point back through the equilibrium position, since the velocity increases.

Bottom: Zoom into half a pendulum oscillation. The average value is indicated by the red dashed line. The pendulum amplitude x_0 is estimated by fringe counting from the number of crossings through the dashed line and eq. (5.4). The inset shows a zoom onto the crossing of the pendulum equilibrium position with the maximum interference contrast of 91 %.

of the interference fringes increases up to the equilibrium point of the pendulum, since the pendulum velocity increases. The distance the pendulum is traveling can be inferred from the number of interference fringes n_F . The pendulum amplitude x_0 is half this distance, resulting in

$$x_0 = \frac{n_F \lambda}{2} \quad (5.4)$$

where λ is the laser wavelength, in this case 1550 nm. I got the number of fringes by counting the crossings of the average value line (red dashed line). I assume an error of 5 fringes for $n_F = 352(5)$. This results in an amplitude $x_0 = 273(4) \mu\text{m}$.

5.5. Pendulum in Quadrature Phase Space

Another way to display the pendulum motion is via the X and Y components in the rotating frame of the lock-in amplifier LO. This way, one can isolate the signal of a specific pendulum mode via the low pass filter bandwidth. Figure 5.12 shows such a measurement of the main pendulum mode in the vertical QPD signal. It was taken with a demodulation frequency of 1.435 001 24 Hz, which is slightly lower than the mode frequency, and a filter bandwidth of 200 mHz for an 8-pole low pass filter. It was sampled with a rate of 14.05 s^{-1} over 583 s. The left side of fig. 5.12 shows the signal in the rotating frame with the start and end points indicated. The red dashed line shows the average value of the complex amplitude R . The trace moves anti-clockwise, since the pendulum oscillates faster than the LO. Since the pendulum was disturbed at the beginning of the measurement, the amplitude decreases over time in a noisy random-walk like motion. On the right side, the time traces of the components X and Y as well as the polar coordinates R and Θ are shown. Here one can again see the decreasing amplitude, while the phase θ increases over time, due to the faster rotation.

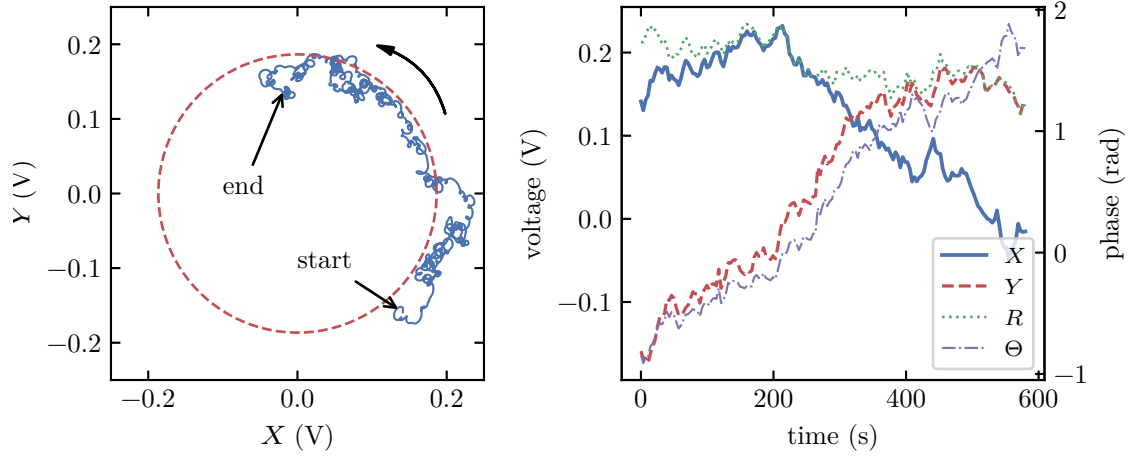


Figure 5.12.: Quadrature representation of the main pendulum mode at 1.4352 Hz. The vertical QPD signal is demodulated with a LO at 1.435 001 24 Hz and an 8-pole low pass filter bandwidth of 200 mHz. The sampling rate was 14.05 s^{-1} with a total measurement time of 583 s.

Left: Phase space representation of the two quadrature components in the rotating frame of the LO. The dashed red line indicates the average value of the amplitude $R = \sqrt{X^2 + Y^2}$. The overall trace rotates anti-clockwise since the actual pendulum frequency is slightly above the demodulation frequency. The amplitude also decreases over time in a random walk like motion, since the pendulum was slightly excited at the start of the measurement.

Right: Time traces of the quadrature components X and Y and the polar coordinates. Here, one can also see the decrease over time of the amplitude R as well as the increasing phase, since the pendulum is oscillating slightly faster than the LO.

6. Summary and Outlook

During this work I designed and set up an optomechanical tabletop experiment with a 50 g cuboid test mass, suspended by tungsten wires, that serves as the common end mirror in a Michelson interferometer with a Michelson-Sagnac like topology. I designed the test mass as an optical cavity to be used for alignment purposes. Since the manufactured test mass did not turn out to provide a stable cavity axis, this alignment procedure could not be tested. Nevertheless, I successfully suspended the test mass pendulum with a high Q factor between 4×10^4 to 7.6×10^4 for the main pendulum mode. The measured Q factors for the yaw and pitch pendulum modes are lower than that of the main mode. For the yaw mode, the energy is stored in lossy elastic deformation of the suspension wires, resulting in a higher loss factor. Since the main pendulum mode stores most of the energy in the lossless gravitational field, the mechanical loss is lowered by the dilution factor.

With the precise interferometric position readout and the detection of the deflection angle presented here, the pendulum oscillation can be measured over multiple orders of magnitude. Additionally, the optical setup allows for a radiation pressure force to be applied to the pendulum by using a second wavelength inside the interferometer. Due to too much seismic excitation, an effect on the pendulum motion could not be observed yet. I estimated the pendulum amplitude due to the remaining seismic excitation to $273(4) \mu\text{m}$ by fringe counting in the interferometric signal. The implemented parametric actuation of the suspension point is used for excitation of the pendulum mode. Currently, a feedback loop to control the parametric phase is being implemented, which will enable controlled cooling of the pendulum motion in the future.

In the next steps of the experiment, an active seismic isolation system to control the supporting concrete block of the optical table will be implemented to reduce the on-resonance excitation of the pendulum to allow for single fringe operation of the interferometric readout. With lower seismic excitation, it might also be possible to observe cooling of the test mass motion by means of active radiation pressure feedback cooling.

Once a shot noise limited operation of the interferometer is established, the planned power recycling mirror can be implemented to increase the optical power in the interferometer and thus increase the displacement sensitivity. Additionally, a signal

recycling mirror in the output port can be used for further enhancement of the interferometer's sensitivity.

If nonlinear mode coupling of the different pendulum modes is present, the mode frequency of one mode could be influenced by the amplitude of another mode as described in [81, 82]. This would make it possible to detect the displacement of one mode by measuring the frequency shift of another. Since the observed pitch mode frequency in our experiment is nearly an integer multiple of the main mode eigenfrequency, nonlinear mode coupling could be enhanced and observation of internal or autoparametric resonance as discussed in [82] might be possible.

Bibliography

- [1] LIGO Scientific Collaboration and Virgo Collaboration et al. “Observation of Gravitational Waves from a Binary Black Hole Merger”. In: *Physical Review Letters* 116.6 (Feb. 11, 2016), p. 061102. DOI: 10.1103/PhysRevLett.116.061102 (cit. on pp. iii, v, 1, 13).
- [2] Roman Schnabel. “Einstein-Podolsky-Rosen - entangled motion of two massive objects”. In: *Physical Review A* 92.1 (July 28, 2015), p. 012126. ISSN: 1050-2947, 1094-1622. DOI: 10.1103/PhysRevA.92.012126. arXiv: 1508.06462 (cit. on pp. iii, v, 1, 23, 28).
- [3] Seth B. Cataño-Lopez et al. “High-Q Milligram-Scale Monolithic Pendulum for Quantum-Limited Gravity Measurements”. In: *Physical Review Letters* 124.221102 (2020), p. 6 (cit. on pp. iii, v).
- [4] A. A. Michelson. *The relative motion of the Earth and of the luminiferous ether*. Aug. 1881. DOI: 10.2475/ajs.s3-22.128.120 (cit. on p. 1).
- [5] A. A. Michelson and E. W. Morley. “On the Relative Motion of the Earth and the Luminiferous Ether”. In: *American Journal of Science* s3-34.203 (Nov. 1887), pp. 333–345. ISSN: 0002-9599. DOI: 10.2475/ajs.s3-34.203.333. eprint: <https://www.ajsonline.org/content/s3-34/203/333.full.pdf> (cit. on pp. 1, 13).
- [6] Georges Sagnac. “L’ether lumineux demontre par l’effet du vent relatif d’ether dans un interferometre en rotation uniforme”. In: *Comptes Rendus* 157 (1913), pp. 708–710 (cit. on p. 1).
- [7] Ludwig Zehnder. “Ein neuer Interferenzrefraktor”. In: *Zeitschrift für Instrumentenkunde* 11 (1891), pp. 275–285 (cit. on p. 1).
- [8] Ludwig Mach. “Ueber einen Interferenzrefraktor”. In: *Zeitschrift für Instrumentenkunde* 12 (1892), pp. 89–93 (cit. on p. 1).
- [9] Kazuhiro Yamamoto et al. “Quantum noise of a Michelson-Sagnac interferometer with translucent mechanical oscillator”. In: *Physical Review A* 81.3 (Mar. 29, 2010), p. 033849. ISSN: 1050-2947, 1094-1622. DOI: 10.1103/PhysRevA.81.033849. arXiv: 0912.2603 (cit. on pp. 1, 13, 22, 26, 27).
- [10] André Xuereb, Roman Schnabel, and Klemens Hammerer. “Dissipative Optomechanics in a Michelson-Sagnac Interferometer”. In: *Physical Review Letters* 107.21 (Nov. 16, 2011), p. 213604. ISSN: 0031-9007, 1079-7114. DOI: 10.1103/PhysRevLett.107.213604 (cit. on pp. 1, 13).

-
- [11] Nikita Vostrosablin and Sergey Vyatchanin. “Stable optical spring in aLIGO detector with unbalanced arms and in Michelson-Sagnac interferometer”. In: *Physical Review D* 89.6 (Mar. 24, 2014), p. 062005. ISSN: 1550-7998, 1550-2368. DOI: 10.1103/PhysRevD.89.062005. arXiv: 1312.7153 (cit. on pp. 1, 13).
- [12] Henning Kaufer. “Opto-mechanics in a Michelson-Sagnac interferometer”. PhD thesis. Universität Hannover, 2014 (cit. on pp. 1, 3, 13, 17, 21, 23, 24, 25, 27).
- [13] Andreas Sawadsky. “Optomechanical Coupling in an Interferometer with a SiN-Membrane”. PhD thesis. Universität Hannover, 2017 (cit. on p. 1).
- [14] Lisa Kleybolte. “Sensitivity Enhancement of Optomechanical Measurements using Squeezed Light”. PhD thesis. Universität Hamburg, 2019 (cit. on pp. 1, 13).
- [15] Akito Araya et al. “Highly sensitive wideband seismometer using a laser interferometer”. In: *Review of Scientific Instruments* 64.5 (May 1993), pp. 1337–1341. ISSN: 0034-6748, 1089-7623. DOI: 10.1063/1.1144089 (cit. on p. 1).
- [16] M G Beker. “Newtonian noise and ambient ground motion for gravitational wave detectors”. In: *Journal of Physics* (2011), p. 10 (cit. on p. 1).
- [17] Michael Coughlin et al. *Towards a first design of a Newtonian-noise cancellation system for Advanced LIGO*. Dec. 20, 2016. DOI: 10.1088/0264-9381/33/24/244001. arXiv: 1606.01716 [astro-ph, physics:gr-qc]. URL: <http://arxiv.org/abs/1606.01716> (visited on 02/05/2022) (cit. on p. 1).
- [18] Helge Müller-Ebhardt et al. “Entanglement of Macroscopic Test Masses and the Standard Quantum Limit in Laser Interferometry”. In: *Physical Review Letters* 100.1 (Jan. 7, 2008), p. 013601. ISSN: 0031-9007, 1079-7114. DOI: 10.1103/PhysRevLett.100.013601 (cit. on p. 1).
- [19] Daniel Hartwig, Jan Petermann, and Roman Schnabel. *Mechanical parametric feedback-cooling for pendulum-based gravity experiments*. Feb. 17, 2021. arXiv: 2012.12158 [gr-qc, physics:physics]. URL: <http://arxiv.org/abs/2012.12158> (visited on 03/12/2021) (cit. on pp. 2, 12).
- [20] Volker Leonhardt. “Displacement measurements on suspended mirrors for off-resonant thermal noise detection”. PhD thesis. Universität Hannover, 2003 (cit. on pp. 3, 4).
- [21] Peter R. Saulson. *Fundamentals of interferometric gravitational wave detectors*. Second edition. Hackensack, NJ: World Scientific, 2017. 313 pp. ISBN: 978-981-314-307-4 (cit. on pp. 4, 8, 18).
- [22] Ian Hickman. *Analog Electronics: Analog Circuitry Explained*. Newnes, Oct. 2, 2013. 342 pp. ISBN: 978-1-4831-6228-7 (cit. on p. 4).
- [23] John A Gubner. *Probability and Random Processes for Electrical and Computer Engineers*. 2006 (cit. on p. 6).

- [24] J. B. Johnson. “Thermal Agitation of Electricity in Conductors”. In: *Physical Review* 32.1 (July 1, 1928), pp. 97–109. DOI: 10.1103/PhysRev.32.97 (cit. on p. 7).
- [25] H. Nyquist. “Thermal Agitation of Electric Charge in Conductors”. In: *Physical Review* 32.1 (July 1, 1928), pp. 110–113. ISSN: 0031-899X. DOI: 10.1103/PhysRev.32.110 (cit. on p. 7).
- [26] Herbert B. Callen and Theodore A. Welton. “Irreversibility and Generalized Noise”. In: *Physical Review* 83.1 (July 1, 1951), pp. 34–40. ISSN: 0031-899X. DOI: 10.1103/PhysRev.83.34 (cit. on p. 7).
- [27] R Kubo. “The fluctuation-dissipation theorem”. In: *Reports on Progress in Physics* 29.1 (Jan. 1966), pp. 255–284. DOI: 10.1088/0034-4885/29/1/306 (cit. on p. 7).
- [28] Kurt Magnus, Karl Popp, and Walter Sextro. *Schwingungen*. Wiesbaden: Springer Fachmedien Wiesbaden, 2016. ISBN: 978-3-658-13820-2. DOI: 10.1007/978-3-658-13821-9 (cit. on p. 10).
- [29] J.E. Logan, J. Hough, and N.A. Robertson. “Aspects of the thermal motion of a mass suspended as a pendulum by wires”. In: *Physics Letters A* 183.2-3 (Dec. 1993), pp. 145–152. ISSN: 03759601. DOI: 10.1016/0375-9601(93)91161-W (cit. on p. 11).
- [30] Michele Punturo. *The VIRGO sensitivity curve*. VIRGO Report No. VIR-NOT-PER-1390-51. Cascina (PI), Italy: VIRGO, July 21, 2003 (cit. on p. 11).
- [31] Daniel Hartwig. “Parametrically Damped High-Q Mechanical Pendulum with Interferometric Readout”. MA thesis. Universität Hamburg, 2018 (cit. on p. 12).
- [32] A. Einstein. “Zur Elektrodynamik bewegter Körper”. In: *Annalen der Physik* 322.10 (1905), pp. 891–921. ISSN: 00033804, 15213889. DOI: 10.1002/andp.19053221004 (cit. on p. 13).
- [33] A. A. Michelson and Henry G. Gale. “The Effect of the Earth’s Rotation on the Velocity of Light, II.” In: *The Astrophysical Journal* 61 (Apr. 1925), p. 140. ISSN: 0004-637X, 1538-4357. DOI: 10.1086/142879 (cit. on pp. 13, 17).
- [34] B Willke et al. “The GEO 600 gravitational wave detector”. In: *Classical and Quantum Gravity* 19.7 (Apr. 7, 2002), pp. 1377–1387. ISSN: 0264-9381, 1361-6382. DOI: 10.1088/0264-9381/19/7/321 (cit. on p. 13).
- [35] J J Fendley. “Measurement of refractive index using a Michelson interferometer”. In: *Physics Education* 17.5 (Sept. 1, 1982), pp. 209–211. ISSN: 00319120. DOI: 10.1088/0031-9120/17/5/001 (cit. on p. 13).
- [36] Michael R. Grace et al. “Quantum-Enhanced Fiber-Optic Gyroscopes Using Quadrature Squeezing and Continuous Variable Entanglement”. In: (Mar. 27, 2020). DOI: 10.1103/PhysRevApplied.14.034065 (cit. on p. 13).
- [37] Daniel Friedrich. “Laser interferometry with coating-free mirrors”. PhD thesis. Universität Hannover, 2011. DOI: 10.15488/7621 (cit. on p. 13).

-
- [38] A. A. Michelson. “The Effect of the Earth’s Rotation on the Velocity of Light, I.” In: *The Astrophysical Journal* 61 (Apr. 1925), p. 137. ISSN: 0004-637X, 1538-4357. DOI: 10.1086/142878 (cit. on p. 17).
- [39] Gerhard Heinzel. “Advanced optical techniques for laser-interferometric gravitational-wave detectors”. PhD thesis. Universität Hannover, 1999 (cit. on pp. 19, 27).
- [40] H Kogelnik and T Li. “Laser Beams and Resonators”. In: *Applied Optics* 5.10 (Oct. 1966), pp. 1550–1567 (cit. on pp. 19, 20).
- [41] Peter Lambropoulos and David Petrosyan. *Fundamentals of quantum optics and quantum information*. Berlin ; New York: Springer, 2007. 325 pp. ISBN: 978-3-540-34571-8 (cit. on p. 21).
- [42] M. Heurs. “Gravitational wave detection using laser interferometry beyond the standard quantum limit”. In: *Philosophical Transactions of the Royal Society A: Mathematical, Physical and Engineering Sciences* 376.2120 (May 28, 2018), p. 20170289. ISSN: 1364-503X, 1471-2962. DOI: 10.1098/rsta.2017.0289 (cit. on pp. 21, 22).
- [43] J. Aasi et al. “Enhanced sensitivity of the LIGO gravitational wave detector by using squeezed states of light”. In: *Nature Photonics* 7.8 (Aug. 2013), pp. 613–619. ISSN: 1749-4885, 1749-4893. DOI: 10.1038/nphoton.2013.177 (cit. on p. 21).
- [44] Mikhail Korobko. “Taming the quantum noise - How quantum metrology can expand the reach of gravitational-wave observatories”. PhD thesis. Universität Hamburg, 2020 (cit. on p. 24).
- [45] Ralf Riedinger. “Optomechanical State Reconstruction and Optical Noise Reduction for Cavity Optomechanics Experiments”. MA thesis. Marburg: Philipps Universität Marburg, Aug. 2013. 96 pp. (cit. on p. 24).
- [46] Dan Xu et al. “Laser phase and frequency noise measurement by Michelson interferometer composed of a 3×3 optical fiber coupler”. In: *Optics Express* 23.17 (Aug. 24, 2015), p. 22386. ISSN: 1094-4087. DOI: 10.1364/OE.23.022386 (cit. on p. 25).
- [47] Shuichi Sato et al. “High-gain power recycling of a Fabry–Perot Michelson interferometer for a gravitational-wave antenna”. In: *Applied Optics* 39.25 (Sept. 1, 2000), p. 4616. ISSN: 0003-6935, 1539-4522. DOI: 10.1364/AO.39.004616 (cit. on p. 26).
- [48] M Coughlin and J Harms. “Global characterization of seismic noise with broadband seismometers”. In: (2012), p. 17 (cit. on p. 29).
- [49] Nanometrics Inc. *Trillium 120Q/QA User Guide*. Apr. 6, 2017 (cit. on p. 31).
- [50] P. Welch. “The use of fast Fourier transform for the estimation of power spectra: A method based on time averaging over short, modified periodograms”. In: *IEEE Transactions on Audio and Electroacoustics* 15.2 (June 1967), pp. 70–73. ISSN: 1558-2582. DOI: 10.1109/TAU.1967.1161901 (cit. on pp. 30, 57).

- [51] Ralf Gommers et al. *scipy/scipy: SciPy 1.7.3*. Zenodo, Nov. 24, 2021. DOI: 10.5281/zenodo.5725464 (cit. on pp. 30, 63).
- [52] Pauli Virtanen et al. “SciPy 1.0: Fundamental algorithms for scientific computing in python”. In: *Nature Methods* 17 (2020), pp. 261–272. DOI: 10.1038/s41592-019-0686-2 (cit. on pp. 30, 63).
- [53] M.W.L.M. Rijnen. “A numerical and experimental study on passive damping of a 3D structure using viscoelastic materials”. MA thesis. Eindhoven University of Technology, May 2014 (cit. on pp. 30, 32).
- [54] Alexander Franke. “Finite element simulations of optomechanical components”. MA thesis. Universität Hamburg, 2019 (cit. on pp. 30, 33).
- [55] David Halliday et al. *Physik*. 2., überarb. u. ergänzte Aufl. Weinheim: Wiley-VCH, 2009. 1437 pp. ISBN: 978-3-527-40645-6 (cit. on pp. 33, 37, 41).
- [56] David Roylance. *Engineering Viscoelasticity*. Oct. 24, 2001, p. 38 (cit. on p. 34).
- [57] Wilhelm Rust. *Nichtlineare Finite-Elemente-Berechnungen: Kontakt, Geometrie, Material*. 2., überarb. und erw. Aufl. Studium. Wiesbaden: Vieweg + Teubner, 2011. 301 pp. ISBN: 978-3-8348-1491-3 (cit. on p. 34).
- [58] *Tungsten - online catalogue source - supplier of research materials in small quantities - Goodfellow*. URL: <http://www.goodfellow.com/E/Tungsten.html> (visited on 10/26/2021) (cit. on pp. 35, 43).
- [59] Aaron Meurer et al. “SymPy: symbolic computing in Python”. In: *PeerJ Computer Science* 3 (Jan. 2, 2017), e103. ISSN: 2376-5992. DOI: 10.7717/peerj-cs.103 (cit. on p. 38).
- [60] David John McManus. “Dual Torsion Pendulum Sensor for Measurement of Terrestrial Gravitational Forces”. PhD thesis. Australian National University, June 28, 2019. 158 pp. (cit. on p. 42).
- [61] Stefan Göbner. “The suspension systems of the interferometric gravitational-wave detector GEO 600”. PhD thesis. Universität Hannover (cit. on p. 43).
- [62] AZoM. *Properties: Tungsten*. AZoM.com. URL: <https://www.azom.com/properties.aspx?ArticleID=614> (visited on 01/26/2022) (cit. on p. 43).
- [63] Janyce Franc et al. “Mirror thermal noise in laser interferometer gravitational wave detectors operating at room and cryogenic temperature”. In: (Dec. 2009), p. 29 (cit. on pp. 46, 48).
- [64] Heraeus. *Quartz Glass for Optics Data and Properties*. Dec. 2019 (cit. on pp. 48, 49).
- [65] H. H. Li. “Refractive index of silicon and germanium and its wavelength and temperature derivatives”. In: *Journal of Physical and Chemical Reference Data* 9.3 (July 1980), pp. 561–658. ISSN: 0047-2689, 1529-7845. DOI: 10.1063/1.555624 (cit. on p. 48).

-
- [66] Mikhail N. Polyanskiy. *Refractive index database*. URL: <https://refractiveindex.info> (visited on 02/02/2022) (cit. on p. 48).
- [67] Andreas Freise. *Finesse 2 - Frequency domain INterferomEter Simulation Software*. May 9, 2014 (cit. on p. 47).
- [68] Sellmeier. “Zur Erklärung der abnormen Farbenfolge im Spectrum einiger Substanzen”. In: *Annalen der Physik und Chemie* 219.6 (1871), pp. 272–282. ISSN: 00033804, 15213889. DOI: 10.1002/andp.18712190612 (cit. on p. 49).
- [69] Pascal Gewecke. “Optimierung eines Michelson-Sagnac-Interferometers für die Anwendung von gequetschtem Licht”. MA thesis. Universität Hamburg, 2019 (cit. on p. 49).
- [70] JPE. JPE. URL: <https://www.jpe-innovations.com/> (visited on 01/21/2022) (cit. on p. 50).
- [71] JPE. *MAN01-01 – CRYO LINEAR ACTUATOR (CLAXXXX) USER MANUAL*. July 5, 2021 (cit. on p. 50).
- [72] JPE. *MAN01-09 – CRYO POSITIONING SYSTEMS CONTROLLER (CPSC) USER MANUAL*. Jan. 11, 2021 (cit. on p. 50).
- [73] Guido Van Rossum and Fred L Drake Jr. *Python reference manual*. Centrum voor Wiskunde en Informatica Amsterdam, 1995 (cit. on p. 51).
- [74] Thomas Kluyver et al. “Jupyter Notebooks – a publishing format for reproducible computational workflows”. In: *Positioning and power in academic publishing: Players, agents and agendas*. Ed. by F. Loizides and B. Schmidt. IOS Press. 2016, pp. 87–90 (cit. on pp. 51, 92).
- [75] R. W. P. Drever et al. “Laser phase and frequency stabilization using an optical resonator”. In: *Applied Physics B Photophysics and Laser Chemistry* 31.2 (June 1983), pp. 97–105. ISSN: 0721-7269, 1432-0649. DOI: 10.1007/BF00702605 (cit. on p. 53).
- [76] Coherent. *Operator’s Manual Mephisto Laser*. Nov. 2013 (cit. on p. 55).
- [77] H. Nyquist. “Certain topics in telegraph transmission theory”. In: *Transactions of the American Institute of Electrical Engineers* 47.2 (1928), pp. 617–644. DOI: 10.1109/T-AIEE.1928.5055024 (cit. on p. 58).
- [78] C.E. Shannon. “Communication in the presence of noise”. In: *Proceedings of the IRE* 37.1 (1949), pp. 10–21. DOI: 10.1109/JRPROC.1949.232969 (cit. on p. 58).
- [79] Zurich Instruments. *Principles of lock-in detection and the state of the art*. Nov. 2016 (cit. on p. 58).
- [80] Dana Z. Anderson. “Alignment of resonant optical cavities”. In: *Applied Optics* 23.17 (Sept. 1, 1984), p. 2944. ISSN: 0003-6935, 1539-4522. DOI: 10.1364/AO.23.002944 (cit. on p. 59).

- [81] H. J. R. Westra et al. “Nonlinear Modal Interactions in Clamped-Clamped Mechanical Resonators”. In: *Physical Review Letters* 105.11 (Sept. 10, 2010), p. 117205. DOI: 10.1103/PhysRevLett.105.117205 (cit. on pp. 67, 79).
- [82] Keivan Asadi, Jun Yu, and Hanna Cho. “Nonlinear couplings and energy transfers in micro- and nano-mechanical resonators: intermodal coupling, internal resonance and synchronization”. In: *Philosophical Transactions of the Royal Society A: Mathematical, Physical and Engineering Sciences* 376.2127 (Aug. 28, 2018), p. 20170141. ISSN: 1364-503X, 1471-2962. DOI: 10.1098/rsta.2017.0141 (cit. on pp. 67, 79).

A. Legend
















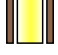












	beam 1550 nm		fixed mirror		signal generator
	beam 1064 nm		manual mirror		mixer
	laser		electric mirror		difference
	Faraday isolator		flip mirror		low pass filter
	optical fiber		beamsplitter		periscope
	electro-optic modulator		polarizing beamsplitter		
	mode cleaner ring cavity		s-pol cleaner		
	photodiode		test mass		
	QPD		half-waveplate		
	beam dump		phase shifter		
			Faraday rotator		
			dichroic mirror		
			lenses		

Figure A.1.: Legend for optics and electronics.

B. Pendulum Fits

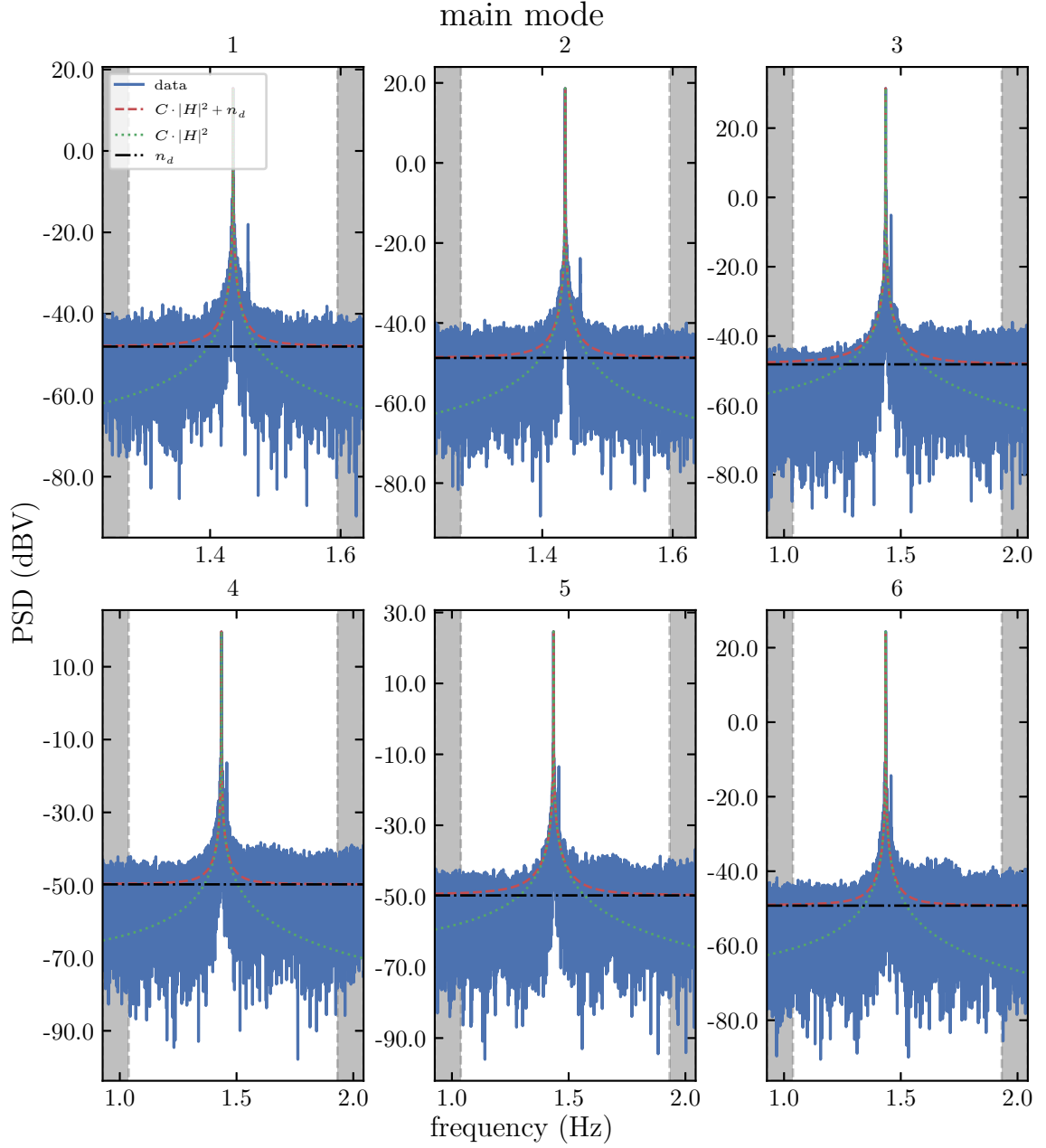


Figure B.1.: Fitted spectral measurements from table 5.1. The measurement time for each trace was 10.4 h corresponding to a RBW of $27 \mu\text{Hz}$. The black dash-dotted line represents the detector noise n_d that is averaged over the gray shaded region. The red dashed line shows the fitted function including detector noise while the green dotted line represents only the oscillator spectral density from the fit parameters.

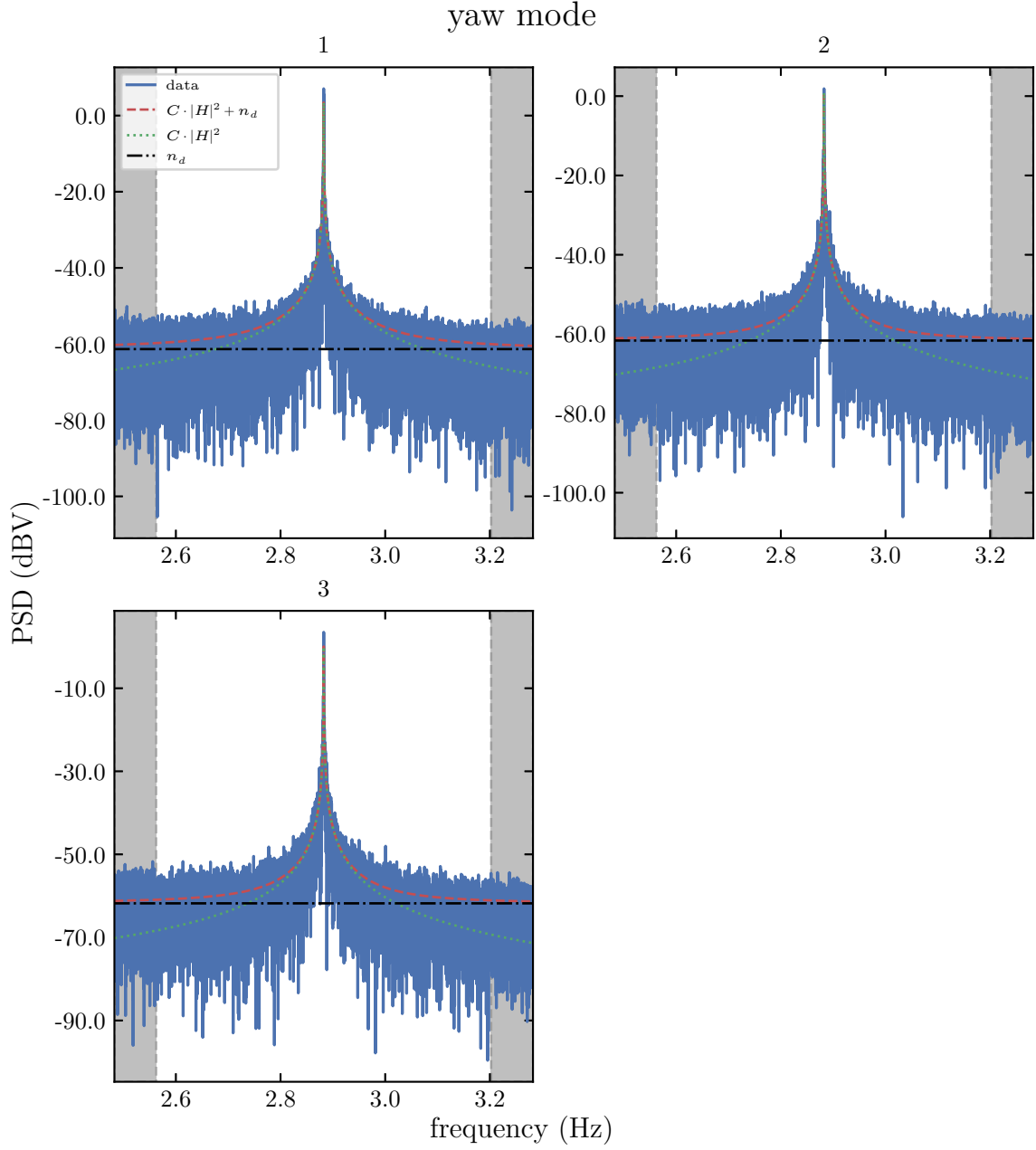


Figure B.2.: Fitted spectral measurements from table 5.2. The measurement times were 10.4 h (trace 1 and 2) and 5.2 h (trace 3) corresponding to a RBW of 27 μ Hz and 54 μ Hz. The black dash-dotted line represents the detector noise n_d that is averaged over the gray shaded region. The red dashed line shows the fitted function including detector noise while the green dotted line represents only the oscillator spectral density from the fit parameters.

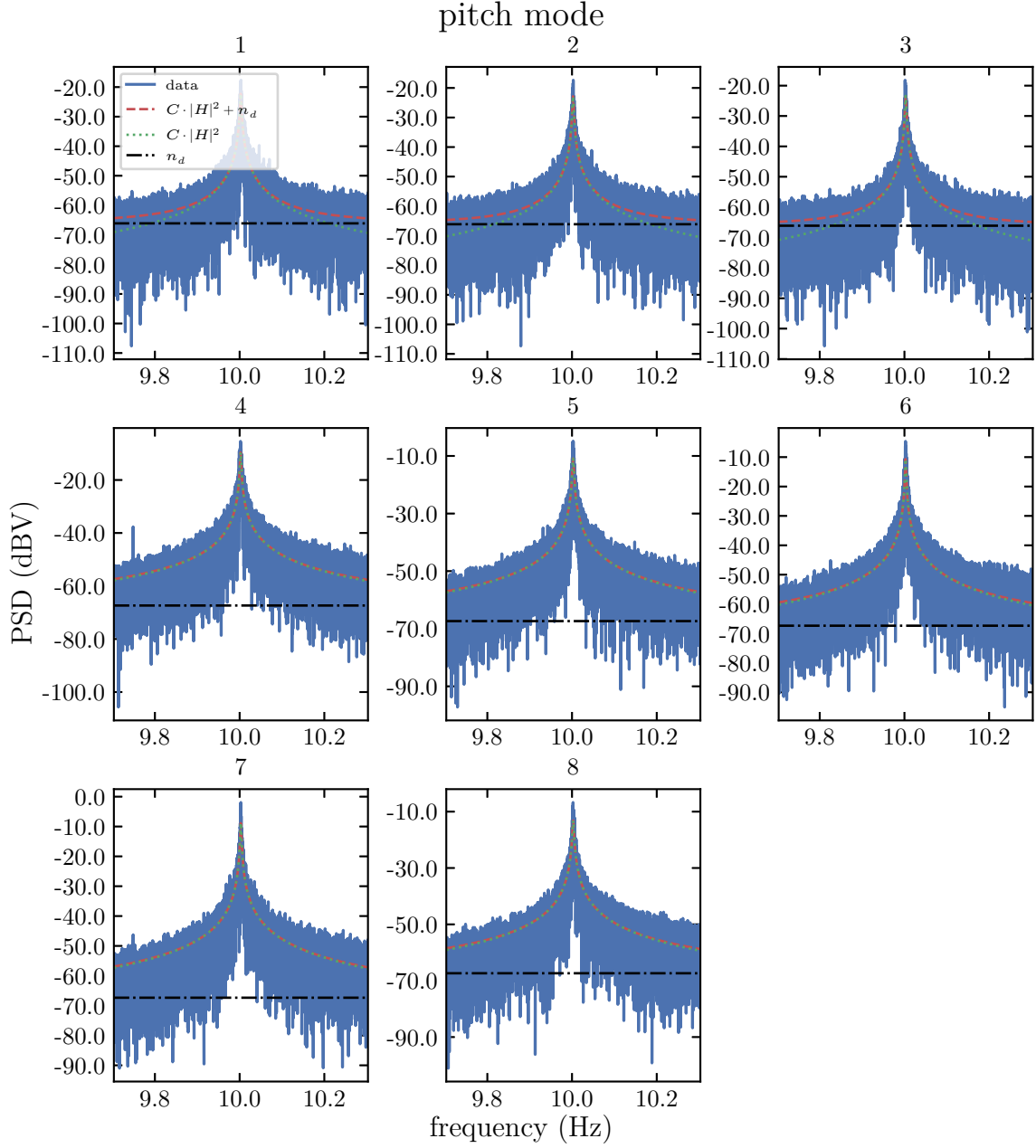


Figure B.3.: Fitted spectral measurements from table 5.1. The measurement time for each trace was 10.4h corresponding to a RBW of $27\mu\text{Hz}$. The black dash-dotted line represents the detector noise n_d that is averaged outside of the plots frequency axis in a flat region due to disturbing peaks near the pitch mode. The red dashed line shows the fitted function including detector noise while the green dotted line represents only the oscillator spectral density from the fit parameters.

C. Ringdown Fits

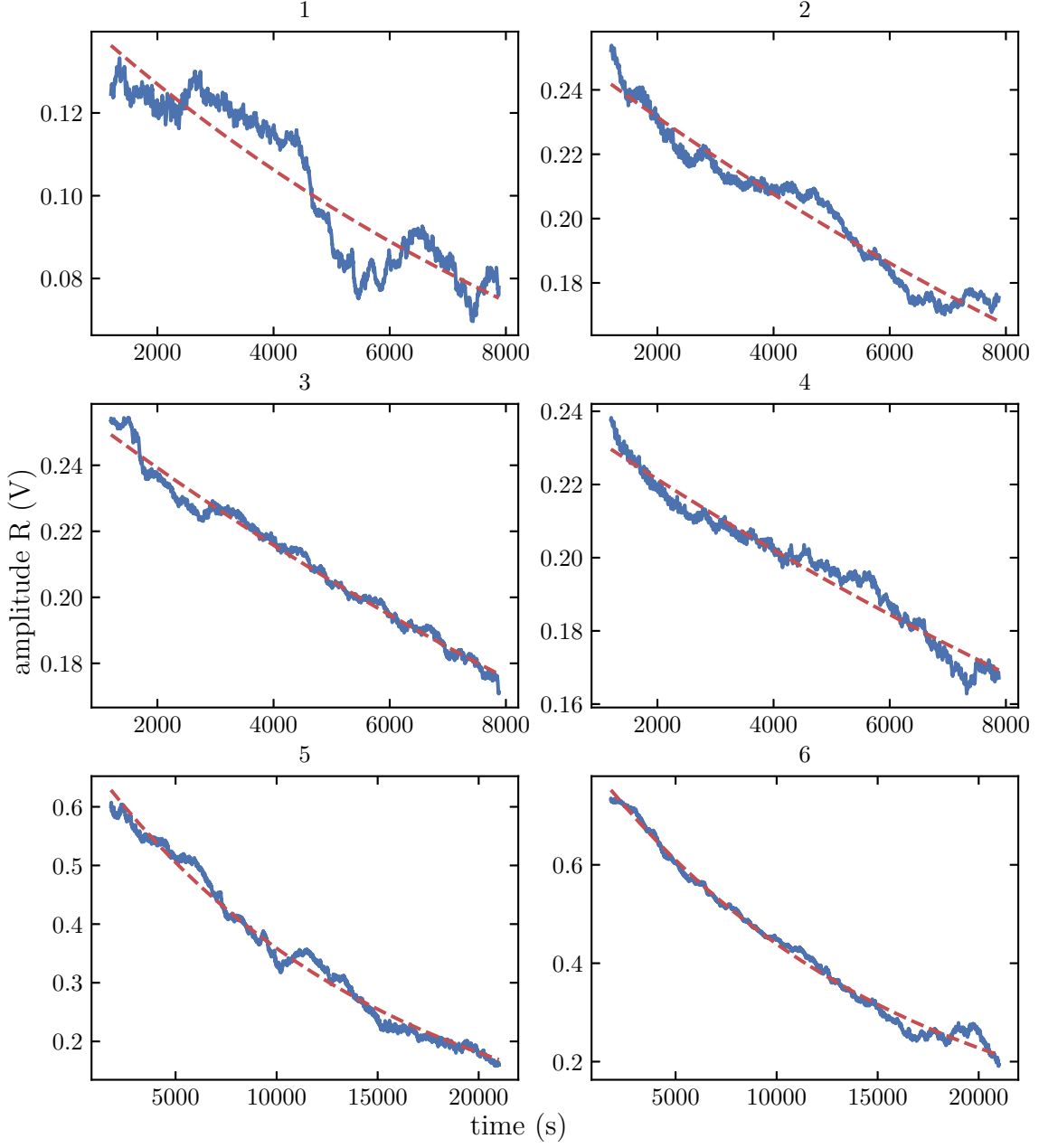


Figure C.1.: Ringdown traces to the fit results in table 5.5. The plots only show the actual ringdown trace, after the pendulum has been excited by parametric actuation, with the corresponding fit of the exponential decay in eq. (5.2).

D. Mirror Positioner Configuration and GUI

Listing D.1: Example configuration for one mirror positioner called **PR**. It has three piezoknobs called **left**, **top** and **right**. The configuration is written in the simple YAML file format.

```
PR:
  controller_address: "192.168.166.201"
  piezoknobs:
    left:
      address: 1
      channel: 2
    top:
      address: 2
      channel: 2
    right:
      address: 3
      channel: 2
```



Figure D.1.: Screenshot of the GUI for the mirror positioner control software. It is build with widgets inside of an Jupyter Notebook [74] which enables cross-platform compatibility. The mirror positioners are split into multiple tabs, each displaying the piezoknobs for a single positioner. The selected tab here displays a positioner which is configured as shown in listing D.1 with an exemplary configuration. Each piezoknob is shown in its own section with a selection for the number of steps and a button for the direction. Additionally, one can move all three piezoknobs at the same time. By default, the step size is set to 100 %. By enabling the precision mode, one can tune the step size and overwrite the default value. This is useful for tuning the mirror position in a sub wavelength range.

Eidesstattliche Versicherung / Declaration on oath

Hiermit versichere ich an Eides statt, die vorliegende Dissertationsschrift selbst verfasst und keine anderen als die angegebenen Hilfsmittel und Quellen benutzt zu haben.

Die eingereichte schriftliche Fassung entspricht der auf dem elektronischen Speichermedium.

Die Dissertation wurde in der vorgelegten oder einer ähnlichen Form nicht schon einmal in einem früheren Promotionsverfahren angenommen oder als ungenügend beurteilt.

Hamburg, 8. September 2022

Unterschrift des Doktoranden

Acknowledgments

Finally, I would like to thank all the people who helped me finishing this thesis.

First of all, I want to thank Prof. Dr. Roman Schnabel for giving me the opportunity to work on this topic in his group and for supervising this work.

A big thank you also goes to all group members for interesting discussions on physics and for the fun and the coffee breaks we had together. Especially, I want to thank our postdocs that I could always come to you with problems and questions.

I want to thank my colleagues Daniel for his support in the lab and Jan for his help with electronics and both of them for proofreading this thesis and also Alex for his help with simulations.

I am grateful for my family and friends who support and encourage me all the time.

Thank you all!

Open Source Software

I would also like to thank the authors of free and open source software that helps scientists all over the world with their work. During the course of this thesis, I used the following software:

- Inkscape [1]
- Inkscape ComponentLibrary [2]
- python [3]
- Matplotlib [4, 5]

- pandas [6, 7]
- SciPy [8, 9]
- SymPy [10, 11]
- numpy [12]
- h5py [13, 14]
- Jupyter [15]
- Finesse 2 [16]

References

- [1] Inkscape Project. *Inkscape*. Version 1.1.1 (cit. on p. 94).
- [2] Alexander Franzen. *ComponentLibrary* (cit. on p. 94).
- [3] Guido Van Rossum and Fred L Drake Jr. *Python reference manual*. Centrum voor Wiskunde en Informatica Amsterdam, 1995 (cit. on p. 94).
- [4] Thomas A. Caswell et al. *matplotlib/matplotlib: REL: v3.5.1*. Zenodo, Dec. 11, 2021. DOI: 10.5281/zenodo.5773480 (cit. on p. 94).
- [5] J. D. Hunter. “Matplotlib: A 2D graphics environment”. In: *Computing in Science & Engineering* 9.3 (2007), pp. 90–95. DOI: 10.1109/MCSE.2007.55 (cit. on p. 94).
- [6] Jeff Reback et al. *pandas-dev/pandas: Pandas 1.1.5*. Zenodo, Dec. 7, 2020. DOI: 10.5281/zenodo.4309786 (cit. on p. 95).
- [7] Wes McKinney et al. “Data structures for statistical computing in python”. In: *Proceedings of the 9th python in science conference*. Vol. 445. Austin, TX. 2010, pp. 51–56 (cit. on p. 95).
- [8] Ralf Gommers et al. *scipy/scipy: SciPy 1.7.3*. Zenodo, Nov. 24, 2021. DOI: 10.5281/zenodo.5725464 (cit. on p. 95).
- [9] Pauli Virtanen et al. “SciPy 1.0: Fundamental algorithms for scientific computing in python”. In: *Nature Methods* 17 (2020), pp. 261–272. DOI: 10.1038/s41592-019-0686-2 (cit. on p. 95).
- [10] Christopher Smith et al. *sympy/sympy: SymPy 1.9*. Zenodo, Oct. 8, 2021. DOI: 10.5281/zenodo.5558034 (cit. on p. 95).

- [11] Aaron Meurer et al. “SymPy: symbolic computing in Python”. In: *PeerJ Computer Science* 3 (Jan. 2017), e103. ISSN: 2376-5992. DOI: 10.7717/peerj-cs.103 (cit. on p. 95).
- [12] Charles R. Harris et al. “Array programming with NumPy”. In: *Nature* 585.7825 (Sept. 2020), pp. 357–362. DOI: 10.1038/s41586-020-2649-2 (cit. on p. 95).
- [13] Andrew Collette et al. *h5py/h5py: 3.2.1*. Zenodo, Mar. 5, 2021. DOI: 10.5281/zenodo.4584676 (cit. on p. 95).
- [14] Andrew Collette. *Python and HDF5*. O’Reilly, 2013 (cit. on p. 95).
- [15] Thomas Kluyver et al. “Jupyter Notebooks – a publishing format for reproducible computational workflows”. In: *Positioning and power in academic publishing: Players, agents and agendas*. Ed. by F. Loizides and B. Schmidt. IOS Press. 2016, pp. 87–90 (cit. on p. 95).
- [16] Andreas Freise. *Finesse 2 - Frequency domain INterferomEter Simulation Software*. May 9, 2014 (cit. on p. 95).